

Evaluating different turbulence models regarding the airflow around a wind turbine

Diploma Thesis

submitted by
Philip Kotrba
on December 7th, 2010



Institute of Hydraulic Fluidmachinery

Head:

O.Univ.-Prof.Dr.Ing. Helmut Jaberg

Advisor TU Graz:

Ass.Prof.Dipl.-Ing.Dr.techn. Helmut Benigni

Advisors AMSC Windtec GmbH:

Dipl.-Ing. Sami Jaber

Dipl.-Ing.Dr.techn. Andreas Tratnig

STATUTORY DECLARATION

I declare that I have authored this thesis independently, that I have not used other than the declared sources / resources, and that I have explicitly marked all material which has been quoted either literally or by content from the used sources.

Graz, December 7th 2010

Philip Kotrba

EIDESSTÄTTLICHE ERKLÄRUNG

Ich erkläre an Eides statt, dass ich die vorliegende Arbeit selbstständig verfasst, andere als die angegebenen Quellen/Hilfsmittel nicht benutzt und die den benutzten Quellen wörtlich und inhaltlich entnommenen Stellen als solche kenntlich gemacht habe.

Graz, am 7. Dezember 2010

Philip Kotrba

Preface

This thesis builds the final milestone for receiving the “Diplomingenieur” degree at Graz University of Technology for me. It has been carried out in association with the Institute of Hydraulic Fluid Machinery at Graz University of Technology and the company AMSC Windtec GmbH located in Klagenfurt.

My personal motivation for this topic was on the one hand, the interest in Computational Fluid Dynamics and on the other hand, the application of this subject to a wind turbine. So I got the possibility to learn more about numerical simulation within the very common and interesting field of wind-energy engineering.

At this point I want to thank my supervisors from the Institute of Hydraulic Fluid Machinery, Ass.Prof.Dipl.-Ing.Dr.techn. Helmut Benigni and Dipl.-Ing. Jürgen Schiffer for their encouragement and great support all the time during my work at the institute. Even in times of trouble they always offered a sympathetic ear.

I would also like to thank my supervisors at AMSC Windtec GmbH, Dipl.-Ing.Dr.techn. Andreas Tratnig and Dipl.-Ing. Sami Jaber. Every time when some data or information about the wind turbine was needed it was passed quickly, so that the work was not retained.

Finally I would like to direct a very warm thank to my family and my girlfriend for all the excellent support during my studies and to my friends for spending great time in Graz.

Thank you!

Abstract

The aim of this thesis was an evaluation of different turbulence models (k/ε , k/ω , BSL- k/ω , SST- k/ω , Spalart-Allmaras and the BSL Reynolds stress model) within CFD simulations for the 2 MW horizontal axis wind turbine WT2000 developed by AMSC Windtec GmbH. The main focus was set on simulations in combination with unstructured grids, in a second step the results of the unstructured grids were compared to results yielded with a structured grid. The mechanical power, streamlines, pressure distribution and airfoil coefficients were the items compared. The deviation of the mechanical power was within a small range for all turbulence models. The Reynolds stress model combined with the unstructured grid yielded the lowest power because of an enlarged separation zone. The biggest deviations were observed for the resolution of the 3D effect in combination with the unstructured mesh. The structured mesh yielded an increased power of 9%. Final comparisons with BEM calculations realized by the AMSC Windtec GmbH showed good agreement whereas the structured grid fitted better to the BEM results.

Zusammenfassung

In dieser Arbeit wurde eine Evaluierung verschiedener Turbulenzmodelle in der CFD-Simulation (k/ε , k/ω , BSL k/ω , SST k/ω , Spalart-Allmaras und BSL Reynoldsstress Modell) am Beispiel der 2 MW Horizontalachsenwindturbine WT2000 der Firma AMSC Windtec GmbH betrachtet. In erster Linie wurden die Simulationen mit unstrukturierten Gittern durchgeführt und in weiterer Folge wurden diese Ergebnisse mit jenen aus den Berechnungen mittels strukturierter Gitter verglichen. Als Vergleich wurden die mechanische Leistung, Stromlinienplots, Druckverteilungen und Profilbeiwerte herangezogen. Die Abweichung der mechanischen Leistung unter den Turbulenzmodellen war für das feinste unstrukturierte Gitter, so wie für das strukturierte Gitter in einem sehr schmalen Bereich. Das Reynoldsstress-Modell lieferte mit dem unstrukturierten Gitter die niedrigste Leistung, was auf einen vergrößerten Ablösungsbereich zurückzuführen ist. Große Unterschiede konnten vor allem für das unstrukturierte Gitter bei der Auflösung des 3D-Effektes am Rotor festgestellt werden. Weiters konnte mit dem strukturierten Gitter eine Leistungssteigerung um ca. 9 % erreicht werden. Abschließende Vergleiche mit BEM Berechnungen von AMSC Windtec GmbH zeigen gute Übereinstimmungen, wobei die Ergebnisse mit dem strukturierten Gitter jene der BEM Berechnungen besser treffen.

Table of Contents

1	Introduction.....	1
2	Review.....	2
2.1	Historical insight into the evolution of wind turbines.....	2
2.2	Available approaches to calculate a horizontal axis wind turbine.....	6
2.3	Examples of different up-to-date wind turbine calculations.....	10
3	Fundamentals.....	18
3.1	Turbulence and its characteristics.....	18
3.2	Turbulence modelling.....	20
3.2.1	Eddy viscosity models.....	21
3.2.2	Second-moment closure models.....	26
4	Simulation.....	27
4.1	Layout of the computational domain for solving the flow.....	27
4.1.1	Interfaces.....	28
4.1.2	Boundary conditions.....	29
4.2	Mesh generation for the blade domain.....	31
4.2.1	Geometry import.....	31
4.2.2	Specification of different element sizes.....	34
4.2.3	Special treatment of the leading and trailing edge.....	35
4.2.4	Near wall treatment of the mesh.....	37
4.2.5	Mesh quality.....	41

5	Results.....	43
5.1	Observed and calculated quantities	43
5.2	Grid dependency study	48
5.2.1	Results for the mechanical power in terms of the unstructured mesh and turbulence model used	48
5.2.2	Results for the mechanical power in terms of a structured mesh and turbulence model.....	54
5.2.3	Streamline plots on the suction side of the blade	56
5.2.4	Pressure coefficient at 4 m airfoil section.....	59
5.2.5	Streamline plots around the 4 m airfoil section.....	62
5.3	Detailed look on the results for the fine and the structured mesh	64
5.3.1	Lift and drag coefficients	66
5.3.2	Pressure distribution around 16 m blade section	71
5.3.3	Wall shear stress at the 4 m airfoil section	73
5.3.4	Streamlines around all selected airfoil sections and tip vortex comparison.....	74
5.4	Transient (time dependent) simulation	78
5.5	Summary of the deviations for the computed mechanical output.....	80
5.5.1	Conversion to the exponential wind profile.....	82
6	Conclusion and prospect	86
7	List of references	89
8	List of tables	91
9	List of diagrams	93
10	List of figures	94

1 Introduction

This thesis aims to determine the differences of turbulence models available within the commercial Computational Fluid Dynamics (CFD) Software ANSYS CFX 11.0 for simulating the airflow around a wind turbine. The horizontal axis wind turbine (HAWT) WT2000 developed by the company AMSC Windtec GmbH is the pretended turbine this work is based on. It is a 2 MW pitch-regulated turbine and has a rotor diameter of 93 m. The nacelle is located 80 m from the ground.

The flow around the turbine is simulated by solving the Reynolds-averaged Navier-Stokes (RANS) equations, which are combined with one of six turbulence models. The chosen models are: k/ε , k/ω , BSL k/ω , SST k/ω , Spalart-Allmaras and the BSL Reynolds stress model. The basic arrangement of the computational domain was investigated within a preliminary thesis [1] which aimed to set up an appropriate simulation for the pretended wind turbine chosen. The aim of this study is, to validate the above mentioned turbulence models by comparing the results themselves and furthermore with 2D Blade Element Momentum (BEM) calculations realized by AMSC Windtec GmbH. Also, the dependence of the resolution of the computational grid and the type of the grid (unstructured and structured) are investigated.

Plotting power graphs in terms of the turbulence model used and the computational grid used is one possible approach to accomplish these comparisons.

This thesis should lead to a more detailed understanding of the behaviour of the different turbulence models considered for the case of simulating a horizontal axis wind turbine in order to get accurate results. Additionally, a literature review was carried out to give the reader an overview of current CFD calculations related to horizontal axis wind turbines.

2 Review

A short historical insight into the evolution of wind turbines leads to the second part of this review, an overview of available approaches for predicting the flow over wind turbines. Furthermore, a literature review of present calculations and their applicability for analysis purposes is given.

2.1 Historical insight into the evolution of wind turbines

A first milestone of the utilization of wind power ranges back into the 14th century, when Guido von Vigevano engineered a wind driven vehicle. It contained a rotor with a diameter of 6-8 m and achieved a maximum speed of approximately 50 km/h.

In the 16th century, the Dutch and Danish population built the leading spearhead in using the power of wind for milling the corn. [2]

At the beginning of the 20th century scientists and technicians already recognised the potential of wind power. Many small wind turbines were situated as local power stations basically for water supply and later on for electricity supply. At that time, Halladay and Eclipse turbines were widespread types. The rotor consisted of approximately 10 to 50 blades and its tip speed ratio (ratio between the circumferential speed of the blade tips and the wind speed) was low. Instead of airfoil shaped blades these turbines had only steel sheet blades. Fig. 1 shows a wind turbine typical for this era.



Fig. 1 Eclipse Wind Turbine [3]

While the basic drive arrangement of these turbines just grounded on momentum calculations as shown in [4], the next generation of wind turbines was marked by the propeller types, which began to originate in the early 20th century in addition to the investigation of airfoil profiles [5].

In 1920, Albert Betz affected the corner stone leading research in the aerodynamic theory of wind turbines. He published the maximum utilizable power of the wind flow with the value being 59,3%. He also formulated the fundamental theory of wind turbine airfoil design.

Some time earlier, at the end of the 19th century, the milestone for generating electricity with wind turbines was set by the Danish scientist Poul La Cour. His turbines still consisted of rotors which were of the same type as the rotors of the typical Dutch wind mills (no propeller types), however they reached a power output of up to 35 kW.

The vertical axis wind turbine Darrieus-Rotor, developed in 1925 by Georges Darrieus, should also be mentioned at this point. This type consists of vertical bended airfoils fixed at the top and bottom of the axis of rotation as displayed in Fig. 2. The advantage of this type of turbine is the independence of the wind direction, so there have to be no yaw drives as these are necessary for horizontal axis wind turbines. However, the vertical axis turbines show some important disadvantages compared to horizontal axis types, since they need to be driven externally to start rotation and the manufacturing of the blades is more complex, since they are submitted to alternating loads. The most powerful Darrieus-Rotor ever built had a mean power of 4 MW and was built in Canada in 1987 (c.f.: Fig. 2). [6]



Fig. 2 4 MW Darrieus-Rotor [6]

In 1931, already a Russian company built a 100 kW propeller type rotor controlled by flaps. [6]

In 1932, the German technician Hermann Honnef was engaged with the development of a large scale wind power plant. The whole construction should be composed of 3 up to 5 multi-megawatt wind turbines. The turbines rotor consisted of two concentric, counter-rotating rotors with a diameter of 160 m. Each turbine should have a mean power of 20 MW at a considered wind speed of 15 m/s! They had to be built analogical to a double-decker in order to ensure the stiffness (i.e. each rotor is made of displaced airfoils). The rotors were considered to be made of Göttinger airfoils to show best aerodynamic characteristics. The mechanical power at the rotor was commuted with an in-wheel electric generator in order to conserve the use of a gearbox which would decrease the overall efficiency of the construction. The rotors were placed within a zone of 200 m up to 500 m above the ground to allow for strong wind conditions. Fig. 3 shows the scheme of Honnef's wind power plant.

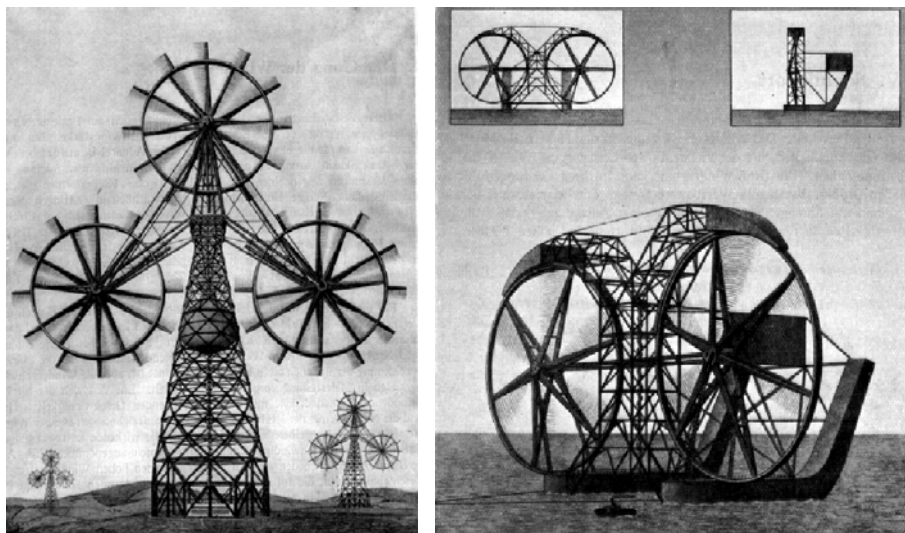


Fig. 3 Scheme of the large-scale power plant (left) and swimming offshore wind turbine (right) of Honnef, 1932 [7]

Honnef also thought about big offshore wind turbines. They should be placed on pontoons as shown in Fig. 3. [7]

However, in spite of all calculations Honnef effected, these great ideas could not be realized because of the complexity of construction. [2]

As a matter of fact, a concept of the Japan Kyushu University published at the Yokohama Renewable Energy International Exhibition 2010 shows a design, similar to the one proposed by Honnef in 1932 (c.f.: Fig. 4).



Fig. 4 New floating wind turbine [8]

In 1941, the American engineer Palmer C. Putnam realized the first large-scale plant with a power of 1250 kW. Theodore von Kármán provided the aerodynamic design of the rotor of this turbine. The turbine had a rotor diameter of 53,3 m.

After the energy crisis in the Seventies of the 20th century, the era of modern wind energy was established. In 1973, in the United States the *Federal Wind Energy Program* was established and many experimental wind turbines were built. During the period from 1975 to 1987, the series MOD-0 – MOD-5 were built with a range from 200 kW up to 3,2 MW. In Europe, the development of modern wind turbines started only a short period of time later. In 1974, a German feasibility study confirmed that a wind turbine based on the concept of Professor U. Hütter, with a rotor diameter of 110 m and a power output of 3 MW, could be built without any difficulty. So, in the late Seventies, the wind turbine “Growian” was developed and then built in 1982. In 1975, Denmark built the experimental plants “Tvind” (designed by amateurs), “Nibe A” and “Nibe B”. Also, the countries Great Britain, Italy, the Netherlands, Spain and Sweden did intensive research within the field of wind power at that time. [6]

At present the largest wind turbine in the world is the E-126 developed by Enercon in Germany, with a nominal power of up to 7,5 MW and a rotor diameter of 127 m. [9]



Fig. 5 Currently, worlds largest wind turbine Enercon E-126 [10]

2.2 Available approaches to calculate a horizontal axis wind turbine

Today, there are basically three different methods available for calculating the power of a wind turbine. Based on these basic methods combinations are also being developed, however, not further discussed in the scope of this thesis. The present work concentrates on the CFD approach, whereas the other approaches are also shortly described in this chapter to give a little overview.

- **Actuator disk method**

The actuator disc method is a one-dimensional theory model which provides an adequate insight into the aerodynamic performance of a rotor. It considers the wind turbine as an infinitesimal thin, permeable disk.

The energy of the wind is extracted by means of the rotor by producing a step change in the static pressure across the rotor swept surface. As the air approaches the rotor, velocity decreases slowly and, as a consequence, the static pressure increases. As a result of the drop in static pressure across the rotor disk, the air behind it is at a sub-atmospheric

pressure level. This causes a further decrease of velocity when the static pressure is gaining to the atmospheric level behind the turbine.

Therefore, we can deduce therefore that there is a reduction in the kinetic energy of the wind, which is converted into useable energy by the wind turbine. [11]

The process across the actuator disk is illustrated in Fig. 6.

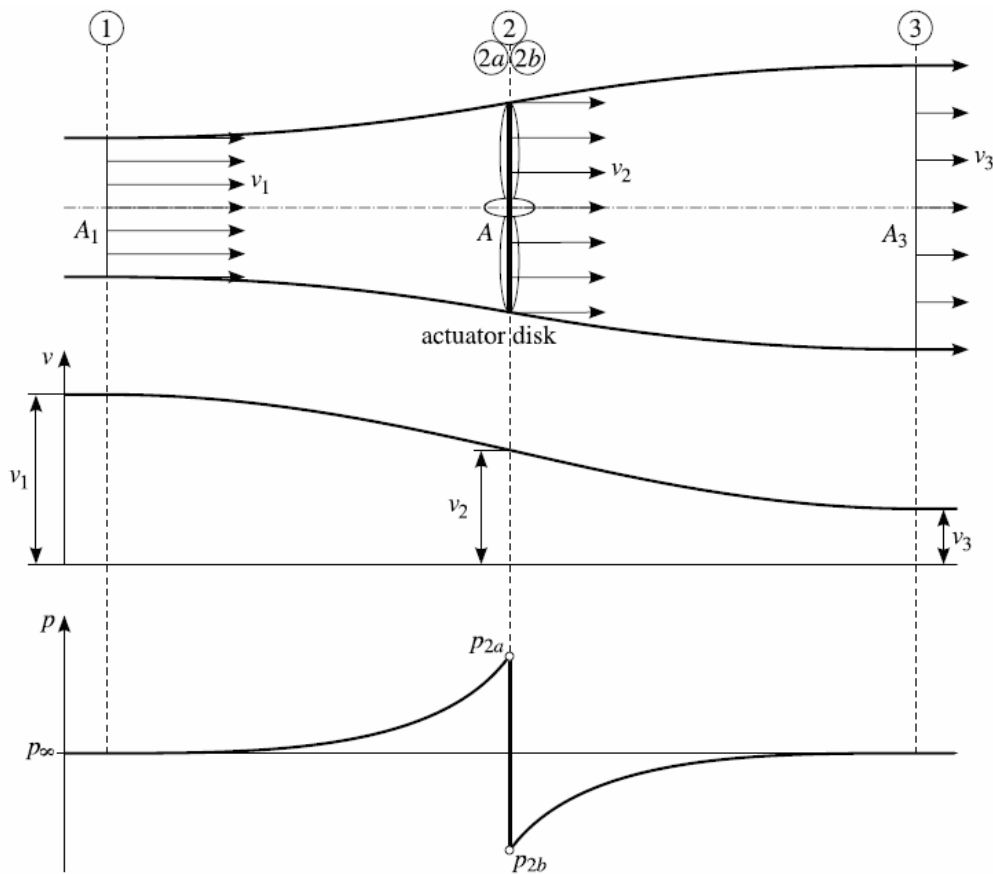


Fig. 6 Flow conditions across the actuator disk [12]

The first row shows the control volume with the actuator disk located in the middle and the velocities at the entrance, the rotor and the outlet. In the second and third row, the velocity and pressure distribution along the axis of rotation from the entrance numbered with 1 to the outlet numbered with 3 are displayed.

This is the simplest model, which is based on the investigations of Lanchester and Betz. [12]

- **Blade Element Momentum theory (BEM)**

As of its simplicity, the BEM theory has become the main stay of the wind turbine industry to predict the performance of turbines. [13]

AMSC Windtec GmbH uses the commercial BEM software GH-Bladed for the development and calculation of its wind turbines.

BEM, the combination of the blade element theory and the momentum theory (similar to the actuator disk approach), is an extension of the actuator disk theory described above. On the one hand, a momentum balance on every rotating annular stream tube as displayed in Fig. 7 is achieved the same way as if the actuator disk theory were used. On the other hand, the blade element theory divides the blade into a number of sections (usually 10-20), see also Fig. 7. This way the power force distribution on each section is calculated by comprising known airfoil coefficients of the blade elements. In this case it is important to say, that two-dimensionality is assumed and neighboring airfoil sections do not influence each other. At each radial position the rate of change of axial and angular momentum is equated with the calculated thrust and torque generated by each blade element. Thus, a set of equations is achieved that can be solved iteratively. [11, 14]

The main problem of BEM codes is their sensitivity to two-dimensional airfoil data. Therefore, it is important to provide exact airfoil characteristics for the calculations.

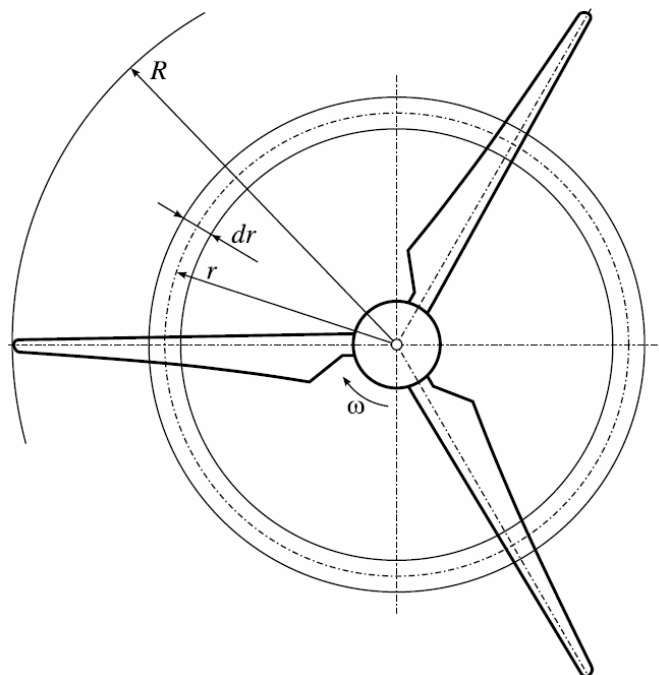


Fig. 7 Annular Element for Blade Element theory [12]

- **Computational Fluid Dynamics (CFD)**

The computational fluid dynamics methods are the most advanced techniques to compute the flow field around a HAWT. Over the past two decades, CFD and, more typically, the finite volume method have been increasingly used to predict the performance of wind turbines. Simple CFD codes calculate the flow field in an inviscid manner, so they do not account for boundary layers on solid surfaces. These codes solve the Euler equations which are derived from the Navier Stokes Equations by setting the viscous forces equal to zero. Some examples of Euler codes could be found in [15, 16]. More sophisticated CFD codes simulate the aerodynamic behavior of the HAWT by solving the Reynolds-Averaged Navier-Stokes (RANS) equations which include the viscous forces acting in a flow. Both, the Euler codes as well as the RANS codes, solve their equations for each element within a control volume that encloses the rotor and its surrounding area. This control volume is discretized by subdividing it into a finite number of volume elements, called the computational mesh or grid. Since CFD methods calculate the whole flow field, they also show effects like three-dimensional flow separation (especially at the inboard sections of the blades), turbulence effects and tip vortices.

Even though CFD requires extensive computing power it has developed to a powerful instrument. It provides a detailed insight in the aerodynamics of wind turbines thus enabling a better understanding for further investigations and developments. [17,18]

In Fig. 8 a representative CFD result is displayed. It shows a streamline plot around a section of the HAWT examined in this thesis. The streamlines in this plot are coloured by the magnitude of their velocity.

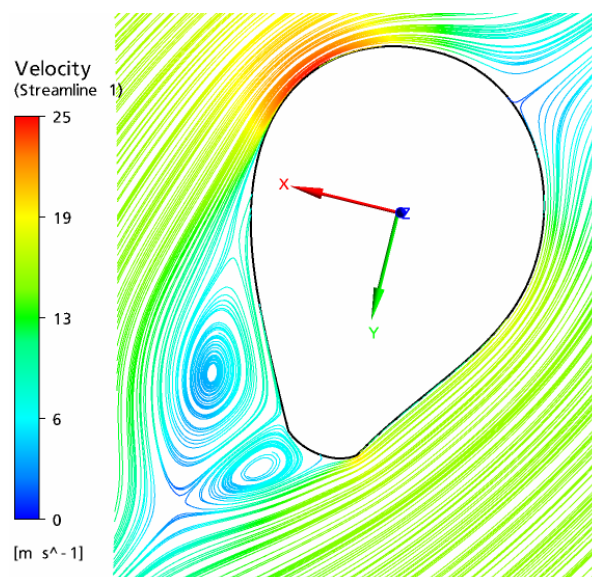


Fig. 8 Streamline plot around a 5,1 m radius blade section(about 10% blade height) at 9,75 m/s wind speed, 15,7 rpm and -0,9° pitch of the WT2000 HAWT

2.3 Examples of different up-to-date wind turbine calculations

Over the past 15 years, a large number of computational calculations of wind turbines and wind turbine airfoils have been carried out. The following pages describe the different approaches of present calculations realized within the scope of research activities with respect to wind turbines. First, calculations of an entire HAWT are presented and then more the calculations of wind turbine airfoils are described.

The general method for simulating a HAWT rotor with the CFD approach is - depend on the number of blades of a rotor - to calculate a segment with just one blade. The reason for this is to keep the computational effort in an acceptable size. This method is proposed by many references like Tachos et al [18], Laursen et al [19] and Kramer and Archer [20]. In Fig. 9, the typical arrangement of a computational domain is illustrated. The commonly used domains usually extend 1 to 10 rotor radii in upstream direction, 2,5 to 10 rotor radii in downstream direction and 1,5 to 10 rotor radii in radial direction. One can say that the smaller values of domain extension are used for smaller wind turbines and the higher values are used for bigger ones, c.f. [18, 19, 20].

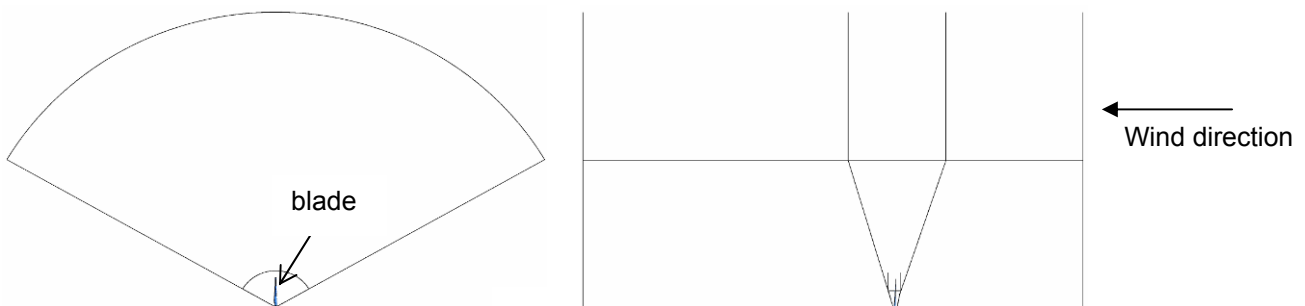


Fig. 9 Frontview (left) and sideview (right) of the whole domain used for the computations in the present thesis

Typically a boundary condition with steady wind speed is applied to the inlet, located at the upstream end of the domain. To the outlet, which is located at the downstream end of the domain, an opening with atmospheric pressure is normally applied.

This sort of simulation was realized by Laursen et al. [19] for a Siemens SWT-2.3-93 variable speed wind turbine with 45 m blades. The operating points observed were varied from 10 rpm and 6 m/s wind speed up to 16 rpm and 11 m/s wind speed.

The aim of the above mentioned research was to perform the simulations with the commercial 3D CFD RANS solver ANSYS CFX 10.0 and 11.0, in order to compare the results against BEM calculations and experimental data of a test turbine. The computations have been primarily performed with a fully turbulent setup using the SST k/ω turbulence model of Menter [21] and, additionally, the two equation laminar/turbulent transition model of Langtry and Menter [22] was tested. Since this is a large turbine, the computational domain extended to the biggest size mentioned above. A block structured hexahedral mesh was applied in a way that the boundary layer was resolved fine enough to ensure a y^+ value smaller than 2. The quantities monitored were the mechanical power and the force distribution on the blades. The fully turbulent setup reflected the measurements very well, with a deviation at most 3,7%. The introduced transition model decreased the calculated drag forces to more realistic levels and, simultaneously, the lift forces were increased. This confirms the theory that a laminar profile has an increased slope of the lift curve compared to a profile with a triggered boundary layer. As a direct consequence of this rise, the mechanical power of the turbine also increased. At last, the comparison among the fully turbulent and the transition case showed that the measurements of the mechanical power fit somewhere between the two cases.

The above HAWT has quite the same dimensions as the HAWT examined for this thesis. So, this former research provided a good basis for the present thesis.

Often, rotors examined correspond to the different types of the National Renewable Energy Laboratory (NREL) [23] rotors as there is a number of experimental data regarding wind tunnel measurements of the mechanical power as well as pressure distribution at selected airfoil sections available for these rotors. So, it is possible to make best comparisons between measurements and simulations. Although these rotors are much smaller than the HAWT presented in this work, the published research on them provided an excellent insight into how to evaluate the results of a simulation. For instance, Tachos et al. [24] did investigations on the NREL Phase II rotor and compared the results gained with experimental data. The rotor investigated is small, with a blade radius of 5,029 m. The nominal rotational speed was 71,68 rpm at a constant wind speed of 7,2 m/s. Due to the fact that this is a very small-sized rotor, the rotational speed is significantly higher compared to the HAWT described above. In [24] as well a computational domain as described above is used and the grid was generated structured-hexahedral. In order to resolve the boundary layer for standard-wall-functions a y^+ value ≥ 30 was aspired. The

CFD simulations were realized with the commercial RANS Solver FLUENT in combination with the one-equation Spalart-Allmaras turbulence model. Analysis of the pressure distribution at selected span wise locations of the blade was compared to experimental data and showed satisfactory agreement. Some discontinuity was found at the leading edge which even increased at the inboard sections of the blade. This discontinuity was most likely due to the incorrectly resolved, highly separated flow by the RANS approximation, state the authors. Another interesting aspect is the limiting streamlines plot presented in [24].

In [24] these streamlines are described as follows:

The curves whose directions coincide with that of the vanishing fluid velocity or shear stress, at the surface.

The plot shows the strong 3D effects which occur near the root.

This kind of visualization will also be considered within this thesis to show differences between the selected turbulence models.

Further investigations of Tachos et al. [18] were conducted with respect to the use of different turbulence models. The rotor analysed has been the same as in the studies mentioned above. The computational domain was also built in the same way and only the turbulence model was altered for the computations. The RANS equations were combined with the Spalart-Allmaras one-equation model, the k/ε model, the renormalization group (RNG) k/ε model and the SST k/ω model of Menter [21]. The RNG- k/ε model is similar to the standard k/ε model but uses different model constants and has some additional terms. All used turbulence models were set to be stable and robust with regard to the considered wind condition. With regard to the computation time demand, the SST k/ω model required a time maximum. For the other models, time demand decreased from 10% (RNG k/ε) up to 20% (Spalart-Allmaras). When comparing the pressure distribution at selected span wise locations the SST k/ω showed the best coincidence to the experiment. Discrepancies only appeared at the leading edge which seems to increase towards the inboard sections of the blade.

Apart from the suction side of the blade the RNG k/ε and the Spalart-Allmaras model as well showed pretty good agreement. The reason for this is, that these models are not suitable to handle highly separated flows and free shear layers, the authors explain. The k/ε model showed only poor agreement to the experiments.

The above-described limiting streamlines were also taken into account in order to show differences among the models tested. The streamlines on the pressure side of the blade showed no significant differences, while the streamlines on the suction side diverged strongly compared to the turbulence model.

The SST k/ω model predicted the strongest 3D effects at the inboard sections of the blade, while with the other models the separation zone extended just to the half of the zone defined for the SST k/ω model. [18]

Gómez-Iradi and Barakos [25] did CFD analysis for the NREL Phase VI rotor with regard to the blade aspect ratio and different tip and root geometries. For the starting configuration there was no root added (blade started at 25% radius) and the nacelle of the turbine was modelled with only an infinite cylinder. Also, the blade was 5,4% longer than the blade used for the experiment, in order to quantify the influence of the blade tip. Starting with this configuration the others were modelled by adding a nacelle instead of the cylinder, adding a root to connect the blade with the nacelle, shorting the blade to the correct length and rounding the blade tip (instead of a flat tip). These different types were compared to experiments in order to show which configuration yielded the best results and which part showed the greatest influence on the results. The simulation runs were conducted with a hexahedral block-structured mesh generated with the commercial software ICEM CFD which is also used for the present work. All simulations were performed in combination with the k/ω turbulence model. The strongest influence on the agreement with the experiments was shown by the blade aspect ratio – whether the correct blade length of the longer blade was taken into account - where models with the original blade length showed better agreement when observing the pressure coefficient at blade sections near the tip. The details of the tip shape and the modelling of the root and nacelle also showed some influence, however, this influence on the overall power output of the turbine was insignificant.

A method how to extract airfoil characteristics from 3D CFD rotor computations is presented by Johansen and Sørensen [26]. The method was applied to the NREL Phase VI rotor and two additional rotors. The process is based on the reduced axial velocity method. Thus, the local flow angle Φ , which is composed of the reduced axial velocity and the circumferential speed, will be calculated by determining the disturbed (reduced) axial velocity in the rotor plane. This way it is possible to calculate the actual inflow velocity to

the airfoil at the selected radial position. The knowledge of the actual inflow velocity provides the possibility to calculate the lift and drag coefficients by means of the forces acting on the selected radial position. Later on the gained airfoil characteristics were imported into a standard BEM software to verify the method explained by means of comparing the resulting mechanical power. Good agreement among the two calculation methods could be stated and therefore the proposed method can be considered to determine airfoil characteristics from a 3D CFD simulation.

This method will also be used for further comparisons among the turbulence models selected for the present work.

Turbulent flow CFD simulations of the NREL S809 airfoil, which is especially designed for HAWT and deployed for the NREL rotors, have been performed by Guerri et al. [27] to compare two different turbulence models at various angles of attack. The turbulence models compared are the SST k/ω model of Menter [21] and the renormalization group (RNG) k/ε model. The SST k/ω model was chosen, because it is able to provide results at strong adverse pressure gradients and has proofed in many references. The above-mentioned additional terms of the RNG k/ε model improve its ability to model swirl flows better than the standard k/ε model. Also, the prediction of the recirculation zone is enhanced. Furthermore, reports say that inaccurate geometry formulation yields inconsistent CFD results so that the geometry of the examined airfoil had to be modelled exactly, in order to force the turbulence models to provide accurate results. The airfoil was located in the middle of the computational domain and extended 10 times the chord in every direction. The mesh was generated in a structured way, at the surface of the airfoil a non-slip boundary condition was imposed. The y^+ value ranged between 2 and 10. The results obtained were compared with reference to wind tunnel data. The observed pressure distribution over the airfoil surface was visualized by plotting pressure coefficient curves for different angles of attack and it was proved that the RNG k/ε model performs slightly better at small angles. At higher angles with separation the SST k/ω predicts better agreement with the experiment. When the angle of attack reached a maximum for both models, discrepancies with the experiment became visible. Looking at the observed lift and drag coefficients (c_L and c_D), the c_L values were in good agreement with the measurements for the linear part of the lift curve but failed to predict the stall location. However, the SST k/ω model performed better, also for the post stall characteristics. The

obtained velocity contours showed a larger separation zone for the SST k/ω than for the RNG k/ε . The results confirmed the performance of the SST k/ω model. [27]

In addition, Wolfe and Ochs [28] performed CFD simulations for the same airfoil using the standard k/ε turbulence model. They started with fully turbulent calculations and furthermore they performed mixed laminar/turbulent calculations. These became possible, by splitting the computational domain. Up to the transition point, the laminar flow was considered and, after this point has been reached, the k/ε model was applied. The airfoil characteristics observed agree better with experimental data when applying the transition approach rather than the fully turbulent. It has also been proved that the k/ε model is not appropriate at angles of attack with flow separation.

Campobasso et al. [29] did two-dimensional CFD calculations of the FFA-W3-241 wind turbine airfoil with regard to wake tracking and turbulence modelling. The airfoil was modelled with a structured c-grid. It was proved that adopting the c-grid behind the airfoil towards the direction of the wake propagation yields an improvement of the results. Whereas the overall number of elements was kept, only the local grid topology was varied. The improvements were depicted with reference to the distance of the wake behind the trailing edge of the blade. However, for the calculated drag coefficients negligible fluctuations and for the lift coefficients small fluctuations were observed no matter whether the wake was tracked correctly or not. With reference to turbulence modelling it was shown that applying a model for laminar/turbulent transition ended in deviations of 50% for the drag. So, the application of a transition model seems to be significant, but, it has to be done with regard to the available computational resources.

Effects of the physics of aero-elastic motion are investigated by Bertagnolio et al. [30]. They carried out investigations by simulating the RISØ-B1-18 airfoil section with a commercial CFD code in 2D and 3D configurations and also compared the obtained results with wind tunnel measurements. At first, they calculated the static airfoil and, in further simulations, the aero-elastic motion was generated with a dynamic inflow condition to the airfoil section. The 2D calculations were realized using the SST k/ω and they predicted enough accurate lift and drag as long as the flow remained attached, for both static and dynamic inflow. Above stall the results differed from the experimental data [30]

In order to reduce the amount of computational effort which is required for 3D CFD simulations Xu and Sankar [31] developed a hybrid Navier-Stokes potential flow solver. Their approach split the flow field into viscous regions, inviscid regions and vortices as to be seen in Fig. 10. The viscous region was solved by a Navier-Stokes solver, the

surrounding inviscid region, by using a compressible potential flow equation. The tip vortices were modelled using a free wake model which is explained in detail in [31]. The method presented has been approved by comparing the obtained results with full 3D CFD simulations, BEM simulations and measurements, and it can be said that good agreement is obtained. [31]

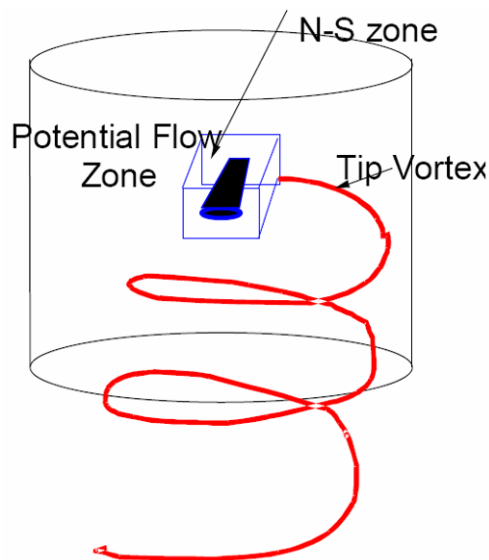


Fig. 10 Split flow field for hybrid Navier-Stokes solver [31]

Another field of interest is the simulation of wind turbine rotors under yawed flow conditions. Madsen et al. [32] calculated the local flow angle by means of CFD as well as actuator disc/BEM simulations and compared these with measurements. These simulations were made with the NREL Phase VI and one other wind turbine for a yaw angle interval of $\pm 60^\circ$. Due to the unsteadiness of the blade coefficients, yawed wind turbine rotor flow simulations had to be performed unsteady. The reason for this is that the blades experience different wind speeds during one revolution. In general, CFD calculations matched well with the measurements while other methods developed a systematic underestimation of the amplitude of the local flow angle which occurs as a bell-shaped curve plotted against the azimuth position of the rotor. Tongchitpakdee et al. [33] also realized similar simulations, however, only with a 3D CFD code.

At this point, Delft University of Technology (DUT) should be cited as well, since it has developed a number of wind turbine airfoils within the last 15 years. The two-dimensional characteristics of these airfoils have been tested extensively in the DUT wind tunnel facility. The aim of these experiments was, on the one hand, to validate the software

XFOIL and RFOIL used for the airfoil development and, on the other hand, the effects of the application of aerodynamic devices such as Gurney flaps – small flaps at the trailing edge to increase the lift - and vortex generators were investigated. The design goal for all DUT airfoils always was set to keep the sensitivity of the airfoil due to contamination and contour imperfections of the nose as low as possible since it rarely occurs that blades are completely clean. At present, the DUT airfoils are used worldwide by various wind turbine and blade manufacturers for wind turbine rotors with 6 to 60 meter blade length and maximum power ranging from 350 kW to 3,5 MW. [34]

In order to develop airfoils with best characteristics for the application in wind turbines, additionally different measurements on existing airfoils have been performed at DUT. So, in [35] the airfoil characteristics of rotating wind turbine blades were investigated by means of experiments. Furthermore in [36] experiments to visualize the flow near the blade root have been performed in an open jet wind tunnel at DUT.

3 Fundamentals

Due to the fact that the present thesis aims to evaluate turbulence models, this chapter should give an overview on the theory of turbulence. Furthermore, the different turbulence models compared are described in a practical way. For more theoretical information see [21, 22, 37, 38 - 41].

3.1 Turbulence and its characteristics

In 1883, Osborne Reynolds proved with experiments, laminar flows transition in turbulent flows by flowing water through a glass pipe into which he injected a dye from a needle. When flow velocity was very slow, the dye was like a linear filament within the water flowing through the pipe as displayed in Fig. 11 a) - laminar flow. After achieving a critical flow rate, the dye filament began to burst - turbulent flow as shown in Fig. 11 b).

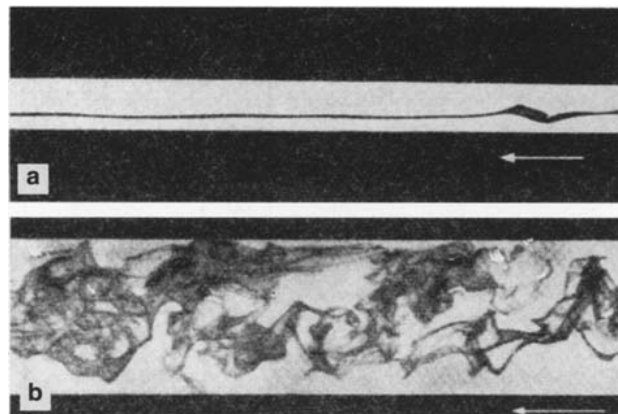


Fig. 11 Dye filament in Reynolds' experiment 1883,
a) laminar flow, b) turbulent flow [39]

The measure whether a flow field is turbulent or not is defined by the Reynolds Number Re . In case of $Re > Re_{crit}$, the flow can be declared as turbulent.

The Reynolds Number is defined by the ratio of inertial forces to viscous forces, where U_∞ represents the characteristic velocity, L the characteristic length, ρ the density and μ the viscosity, and, in a further step ν is used for the kinematic viscosity.

$$Re = \frac{\rho U_\infty L}{\mu} = \frac{U_\infty L}{\nu} \quad (1)$$

This ratio provides the possibility to classify different types of flow. Thus, flows with low Reynolds Numbers are dominated by viscous forces, whereas flows with quite high Reynolds Numbers are dominated by inertial forces.

For instance, the critical Reynolds Number for a flat plate is 5×10^5 [39] whereas the length of the plate represents the characteristic length.

In laminar flows each particle moves on a straight line, parallel to the wall, turbulent flows are characterized by three-dimensional stochastic fluctuations which are overlaid to the main flow. This effect is connected to a rise in the resistance of the flow.

Typical characteristics of turbulent flows [40]:

- highly unsteady in all directions
- turbulence is always associated with vortices
- vortices are in a broad spectrum of scale and fluctuation frequency
- biggest vortices are in the range of the whole flow domain, whereas the smallest vortices are much smaller than the smallest finite volume element of the discretized domain
- vortices consume kinematic energy from the main flow for their own motion
- energy is passed from big vortices to smaller ones. Within the smallest vortices energy is dissipated since viscosity becomes significant (also called energy cascade).

Since turbulence spans a large range of length and time scales, the exact calculation of all these properties is connected to very high effort by solving the governing Navier-Stokes equations. This is done by means of direct numerical simulation (DNS), which resolves the entire flow domain with a very fine grid to capture all effects of turbulence in all scales. However, it is just used for low Reynolds Number flows and simple test cases like flow over a flat plate in order to calibrate turbulence models.

3.2 Turbulence modelling

Engineers are not interested in exact fluctuating values which can only be gained by means of DNS. For them, rather averaged quantities are relevant, so, all details of a flow field do not have to be calculated.

Therefore, Reynolds developed a method to divide the fluctuating components, for instance a velocity U into an averaged component \bar{U} and a time varying component U' , as displayed in Fig. 12.

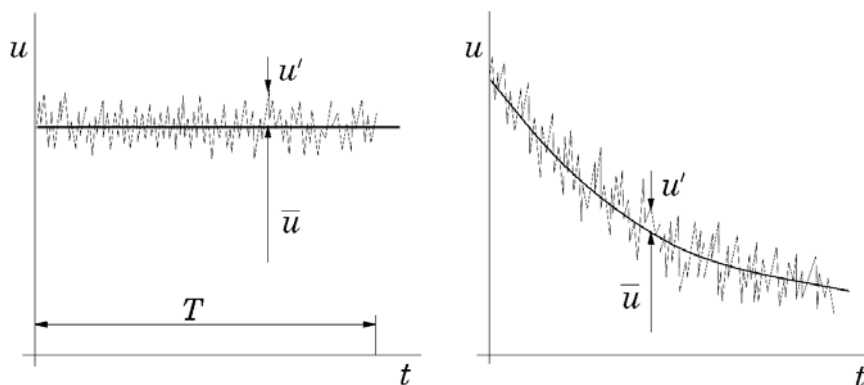


Fig. 12 Averaging of the velocity component U for a statistical steady (left) and unsteady (right) flow [38]

Integrating this averaging into the Navier-Stokes equations yields the Reynolds Averaged Navier-Stokes (RANS) equations. It introduces new, additional unknown terms which act like additional stresses in the fluid and thus the governing system of equations is not “closed”. These terms are called the Reynolds Stresses which form the Reynolds Stress Tensor.

To “close” the system of equations, the Reynolds stresses need to be modelled by additional equations of known quantities. As soon as the system is “closed”, for each unknown quantity an equation is defined.

The function of turbulence models is exactly the fact to model the set of equations for the “closure” of the system.

Two basic concepts for the closure of the system are developed. On the one hand there are the Eddy Viscosity Models (EVM), which are based on a Boussinesq (1877) assumption for the Reynolds stresses and on the other hand there are the Second-Moment Closure Models also known as Reynolds Stress Models that model each

unknown term in the Reynolds Stress Tensor thus providing more, additional equations than EVMs.

3.2.1 Eddy viscosity models

EVMs are grounded on a Boussinesq assumption that expresses the Reynolds Stress Tensor in terms of the mean rate of strain. This assumption bases on the well known material law for Newtonian fluids which is expressed as follows, an in which τ stands for the shear stress, μ for the viscosity, u for the velocity in x direction and y for the distance in y direction.

$$\tau = \mu \frac{du}{dy} \quad (2)$$

In the Boussinesq assumption the viscosity μ is replaced by the eddy viscosity μ_t , which is not a local fluid property as μ but a local flow property (it depends on the local flow situation). The eddy (turbulent) viscosity μ_t overshoots the viscosity μ in high Reynolds flows by orders of magnitude (in free shear flows away from a wall).

By introducing this approximation for the Reynolds Stresses, the problem for the closure has been reduced by defining the eddy viscosity.

The eddy viscosity can be expressed as the product of a characteristic turbulent length and velocity scale. So, these are the two new components which have to be defined.

3.2.1.1 Zero-equation eddy viscosity models

The simplest turbulence models are algebraic eddy viscosity models (zero-equation models) considering the length scale with the characteristic flow dimension and the velocity scale with the mean velocity of the problem observed. This was estimated because the eddy viscosity μ_t represents the transport of momentum by turbulent fluctuations induced by large scale eddies. These are in the dimension of the characteristic flow (length scale) and the characteristic velocity (velocity scale) [41].

These types of models are very simple as the eddy viscosity is calculated to be a global value. Ansys CFX 11.0 uses the fluid domain volume for calculating the length scale and the mean velocity for the velocity scale. The zero equation model implemented in Ansys

CFX 11.0 is just recommended for initial estimations which could be provided as initial value for calculations with more ambitious models. [22,42]

3.2.1.2 One-equation eddy viscosity model

For the present work the Spalart-Allmaras one equation EVM has been considered to prove its ability of predicting the flow over a wind turbine rotor.

This model has been chosen for the evaluation since it has been used for different simulations of wind turbines [18, 24] and it is said to be popular in aeronautics for predicting the flow around aircraft wings and even whole aeroplanes. In general one-equation models are all tuned for predicting external flows like aeronautical applications, however, this restricts their ability to reproduce complex internal flows correctly, since it is very difficult to determine a correct length scale [41].

In a one-equation EVM just one additional differential equation for the velocity scale is modelled to calculate the eddy viscosity μ_t . Spalart-Allmaras uses a transport equation for the kinematic eddy viscosity.

The near wall treatment was done by scaleable wall functions available within Ansys CFX 11.0. Their advantage is that they could be applied to any (fine) resolved near wall mesh. In order to save computational performance effort in fully resolving the boundary layer (which yields a very high number of elements), the wall functions approach uses the logarithmic relation of the velocity for the near wall regions. When using the wall function approach a general suggestion for the dimensionless wall distance is $20 \leq y^+ \leq 100$. [22, 42]

3.2.1.3 Two-equation eddy viscosity models

Two-equation eddy viscosity models use two additional model equations for defining the eddy viscosity. One for the turbulent velocity scale and one for the turbulent length scale. So, μ_t is given by the function,

$$\mu_t \propto \rho U_t L_t \quad (3)$$

whereas U_t represents the velocity scale and L_t the length scale.

For defining the velocity scale for all two-equation models is the turbulent kinetic energy k , which results of the velocity fluctuations within a turbulent flow, is chosen.

$k^{1/2}$ is used to define U_t [41].

- **k- ε model**

The k- ε model is the most widely spread turbulence model and has been implemented into most of the general purpose CFD codes. It is considered as industrial standard.

For many flows of engineering interest it provides acceptably realistic predictions of the mean flow features and has proven to be numerically robust [41]. The strength of the k- ε model can be related to the prediction of flows in the wake of the boundary layer. This feature is considered in the later discussed BSL and SST k/ω model.

However, it also shows defences like underpredicting the amount of separation and too late predicting of the onset of separation. Also, for some applications it is not preferable as Ansys CFX refers to in [42]:

- flows with boundary layer separation
- flows with sudden changes in the mean strain rate
- flows in rotating fluids
- flows over curved surfaces

The k- ε model consists of a transport equation of the above-mentioned turbulent kinetic energy k and it uses another transport equation for the turbulence eddy dissipation ε that is the rate at which turbulent velocity fluctuations dissipate.

Hence, the eddy viscosity for the k- ε model is given by

$$\mu_t = C_\mu \rho \frac{k^2}{\varepsilon} \quad (4)$$

C_μ represents a model constant.

Within the Ansys CFX 11.0 solver the k- ε model is also combined with the above mentioned scaleable wall function approach, which simplifies the process of mesh generation to a great extent. Most notably for complicated geometries that usually appear in technical applications. Note that low Reynolds formulations (as required in the vicinity of walls) of the k- ε model would need a near wall resolution of $y^+ < 0,2$ [22].

- **k- ω model**

The k- ω model makes use of the turbulent frequency ω to define the turbulent length scale for the definition of the eddy viscosity. So, the eddy viscosity is defined by

$$\mu_t = \rho \frac{k}{\omega} \quad (5)$$

Again, for these two quantities model equations are developed. One of the main advantages of the k- ω model is that for near wall bounded low Reynolds flows (near walls) there are no complex damping functions involved - as necessary for the k- ϵ model. So, the k- ω model is much more independent of the near wall resolution than the k- ϵ model [22].

The weakness of the k- ω model is its sensitivity to free stream values of ω (outside the boundary layer) as mentioned in [21]. Simple reduction of ω in the free stream can affect changes of 100% for the eddy viscosity.

In Ansys CFX 11.0 all models based on the ω equation are combined with the “automatic wall treatment” method. Automatic wall treatment uses blending functions in the near wall region to switch from a low Reynolds formulation to a wall functions approach, depending on the refinement of the near wall mesh. A low Reynolds formulation of the ω based models would require a very fine resolution of the near wall mesh in a range of $y^+ \leq 2$ whereas the wall functions approach confirms with $20 \leq y^+ \leq 100$ like mentioned above [42].

- **BSL and SST k- ω model**

To combine the advantages and to avoid the disadvantages of the above presented two equation models, Menter [21] developed two new turbulence models.

First, the baseline model (BSL) was developed. It utilizes the k- ω model near surfaces and by the use of a blending function switches to the k- ϵ model for outer regions.

This is realized by multiplying the k- ϵ model which is transformed into a k- ω formulation by a function $(1-F_1)$ and adding it to the k- ω model times F_1 . The blending function F_1 - a function of the wall distance - is equal to 1 near the wall and switches over to zero in the wake region. In order to determine the blending function an additional equation to compute the wall distance has to be solved. This is made by the solver within the first few iterations of a simulation.

So, a new model based on a $k-\omega$ formulation that switches among the original $k-\omega$ model near the wall and the $k-\varepsilon$ model in the outer region is achieved.

Although the BSL model combines the advantages of the $k-\omega$ and $k-\varepsilon$ models, it still fails to properly predict the amount and the onset of separation on smooth surfaces. Menter explains this weakness with the fact that both models do not account for the transport of the turbulent shear stress which results in an overprediction of the eddy viscosity.

Hence, he developed the Shear Stress Transport (SST) model which additionally accounts for the transport of the turbulent shear stress and therefore provides highly accurate predictions of the onset and of the level of separation under adverse pressure gradients [21].

Thus, the SST model eliminates the deficiencies of the BSL model and therefore is the model of choice for present CFD simulations, as proposed in different references [18, 19, 30, 29] as well.

The SST $k-\omega$ model as well as the BSL model are also combined with the above mentioned “automatic wall treatment” within the Ansys CFX 11.0 solver.

In order to examine the process of laminar turbulent transition, the SST $k-\omega$ model could be combined with a transition model developed by Langtry and Menter. This model solves two additional equations to calculate the intermittency and the transition onset Reynolds Number. However, in order to take advantage from this model it is important to correctly resolve the boundary layer ($y^+ \approx 1$) as well as to have a sufficient number of grid points in stream wise direction to best resolve the region of the transition onset.

This was the dilemma for the calculations realized in addition to the transition model within the present work, as mentioned later.

- **SST-scale-adaptive-simulation (SAS) model**

The SAS model is based on the introduction of the Von Karman length scale into the turbulence scale equation for the usage within time dependent (unsteady) simulations. This step allows for the model to dynamically adjust to resolved structures in an unsteady RANS simulation whereas at the same time for stable flow regions standard RANS capabilities are provided. The application of the SAS approach is realized in combination with the SST $k-\omega$ model as implemented in the Ansys CFX 11.0 solver.

The comparison of simulations with the standard unsteady RANS method and the SAS method shows that the unsteady RANS method just resolves large turbulent structures while the SAS concept dynamically adjusts to already resolved scales.

A major advantage of the SAS modelling is the limited grid sensitivity in comparison to the Detached Eddy Simulation (DES) that switches between a RANS approach inside the boundary layer and calculates the other flow field via Large Eddy Simulation (LES). LES directly models the large scale fluctuating motions, similar to the direct numerical simulation. However, for the LES approach the grid has to be created in a fine manner as the resolution of the grid determines the size of eddies resolved [42].

3.2.2 Second-moment closure models

While two-equation models use the eddy viscosity approach, second-moment closure models or Reynolds Stress models are based on transport equations for all components of the Reynolds Stress tensor (6 equations) and one equation for the dissipation rate. So, these models do not assume an isotropic turbulence but, in principle, enable accurate prediction of the anisotropic turbulence field. Theoretically, Reynolds Stress models are more applicable to complex flows than eddy viscosity models, nevertheless, practice has shown that often they are not better than eddy viscosity models. Due to the six additional equations, the convergence of these models may be slower than for eddy viscosity models and the demand for computational resources is higher [41].

As of the higher accuracy of these models in [42], they are recommended for the following types of flow:

- free shear flows with high anisotropy, including flows in rotating fluids,
- secondary flow (3D effects),
- flows with strong streamline curvature.

All these points supported the application of a second-moment closure model in the scope of the present work. So, for this work simulation runs with the Baseline (BSL) Reynolds stress model supported in Ansys CFX 11.0 in combination with the finest unstructured grid were performed.

4 Simulation

After an introduction into the theory of turbulence modelling, an overview of the pre-processing - the assembling of the computational domain and the definition of boundary conditions - is given in the following chapter. Within a CFD simulation the complete flow region has to be discretized by means of volume elements, called mesh or grid, since RANS equations have to be solved for the whole flow field. For this purpose the procedure of the mesh generation process of the blade domain is described in detail.

4.1 Layout of the computational domain for solving the flow

This chapter describes the different domains which build up the whole computational domain. The overall alignment of the domains, as displayed in Fig. 13, was investigated within a preliminary thesis [1] with the target to set up a simulation for the investigated wind turbine blade. The expansion of the whole domain is equal to 6 rotor radii upstream, 10 rotor radii downstream and 10 rotor radii in radial direction. The rotor radius is 46,5 m.

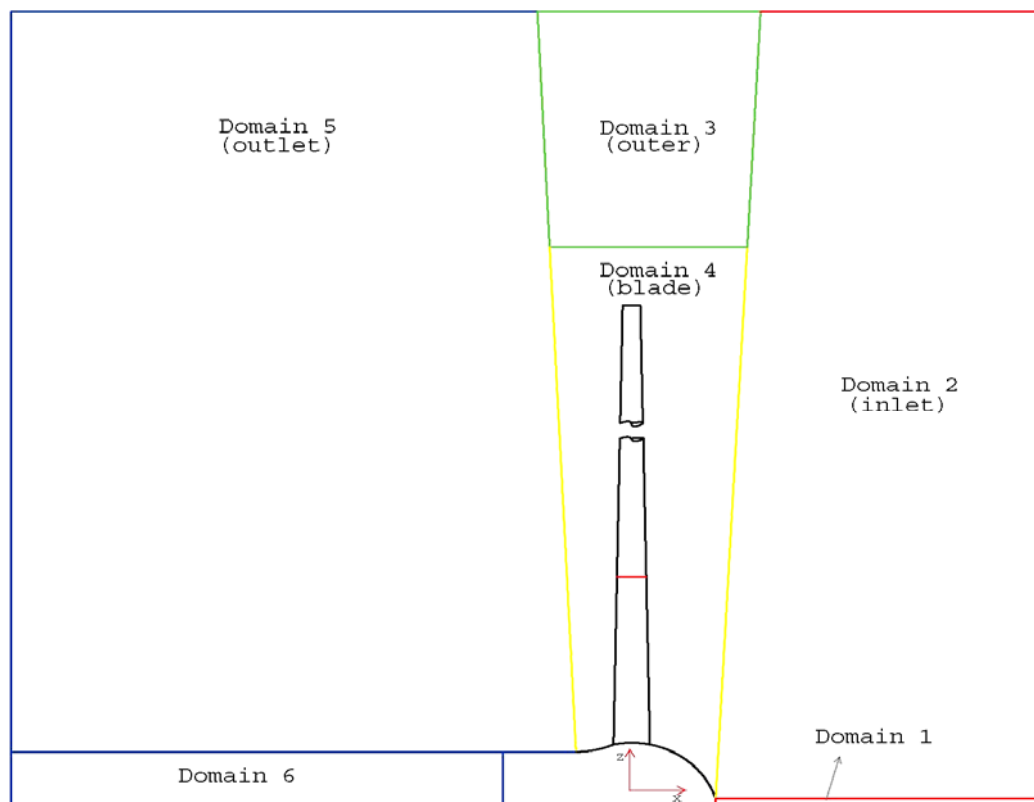


Fig. 13 Schematic diagram of the overall alignment of the domains (sideview)

The domains 1-3, 5 and 6 were adopted from the preliminary thesis [1] and just slightly trimmed to better fit to the newly created blade domain (domain 4). All domains, except the blade domain, were generated in a structured way. For the blade domain the focus was set to build a mesh in an unstructured way. The definitions for a structured and an unstructured mesh are given in chapter 4.2.

4.1.1 Interfaces

To run a simulation with multiple domains, the domains have to be connected to each other by defining interfaces.

Within the present work, interfaces were necessary because of the following reasons:

- The flow field repeats in multiple identical regions around the axis of rotation. For the present simulation just one of the three blades of the wind turbine rotor was modelled in terms of a 120° piece. This was done in order to save computational resources. In the case presented the boundaries tagged by the arrows in Fig. 14 had to be set as “rotational periodicity”.

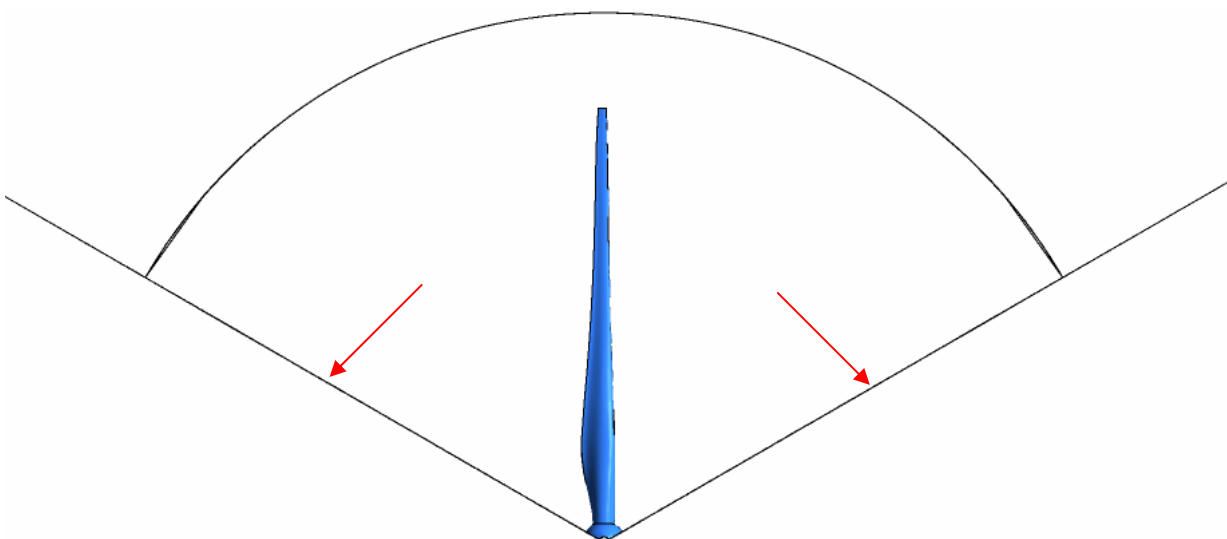


Fig. 14 Front view of the whole domain with boundaries for “rotational periodicity” tagged by arrows

- To the blade domain of the examined rotor different non-matching mesh types (grid points of one mesh do not match exactly with the grid points of the other mesh) had to be connected as displayed in Fig. 15. In the middle, there is the tetrahedral mesh for the blade domain, whereas left and right hexahedral meshes are connected. A common and proposed method for connecting different grids is the General Grid Interface (GGI) connection method which was used for all connections of the meshes realized in this thesis.

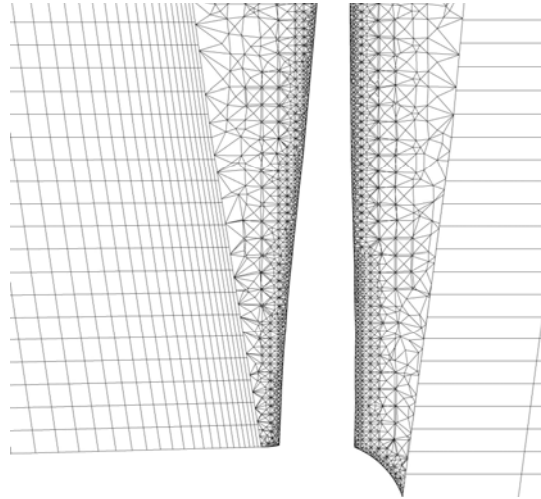


Fig. 15 Connecting different non-matching mesh types

- The blade domain rotates with the rotation speed of the rotor whereas the other domains are static. For this case, a “frozen-rotor” interface was applied to all surfaces being in touch with the blade domain. The frozen-rotor interface calculates the flow inside the rotating domain separately and passes the calculated values to the next frame of reference. However, the frozen-rotor interface calculates the flow for one fixed “frozen” rotor position. Therefore, it is not possible to use this interface for time dependent (transient) simulations. For the transient simulation conducted the interface was changed to “transient-rotor-stator”. This interface takes into account the interaction among stationary and rotating domains.

4.1.2 Boundary conditions

Within the present simulation four different types of boundary conditions had to be set. For each surface representing a real wall (blade and hub surfaces) a “non-slip wall” was set. Thus the behavior of the boundary layer as to the velocity of a fluid that flows around a solid body being zero on the surface of the wall is described.

With regard to the radial exterior surfaces (the surfaces 10 rotor radii in radial direction) “free slip wall” conditions were applied. In fact, this is an outer boundary but it does not act like a real solid body with zero velocity on its surface.

To the inlet surfaces (surfaces 6 rotor radii upstream the rotor in axial direction) “inlet” conditions with a specified velocity magnitude for the wind speed in axial direction were applied as well as the turbulence intensity of the incoming flow. Since there were no exact values available the turbulence intensity for all calculations were set to medium as proposed in [42].

To the outlet surfaces (surfaces 10 rotor radii downstream the rotor in axial direction) “opening” boundaries with 0 Pa relative pressure were applied.

Fig. 16 shows the total assembly of the domain in order to give an overview of the different boundary conditions used within the realized simulation.

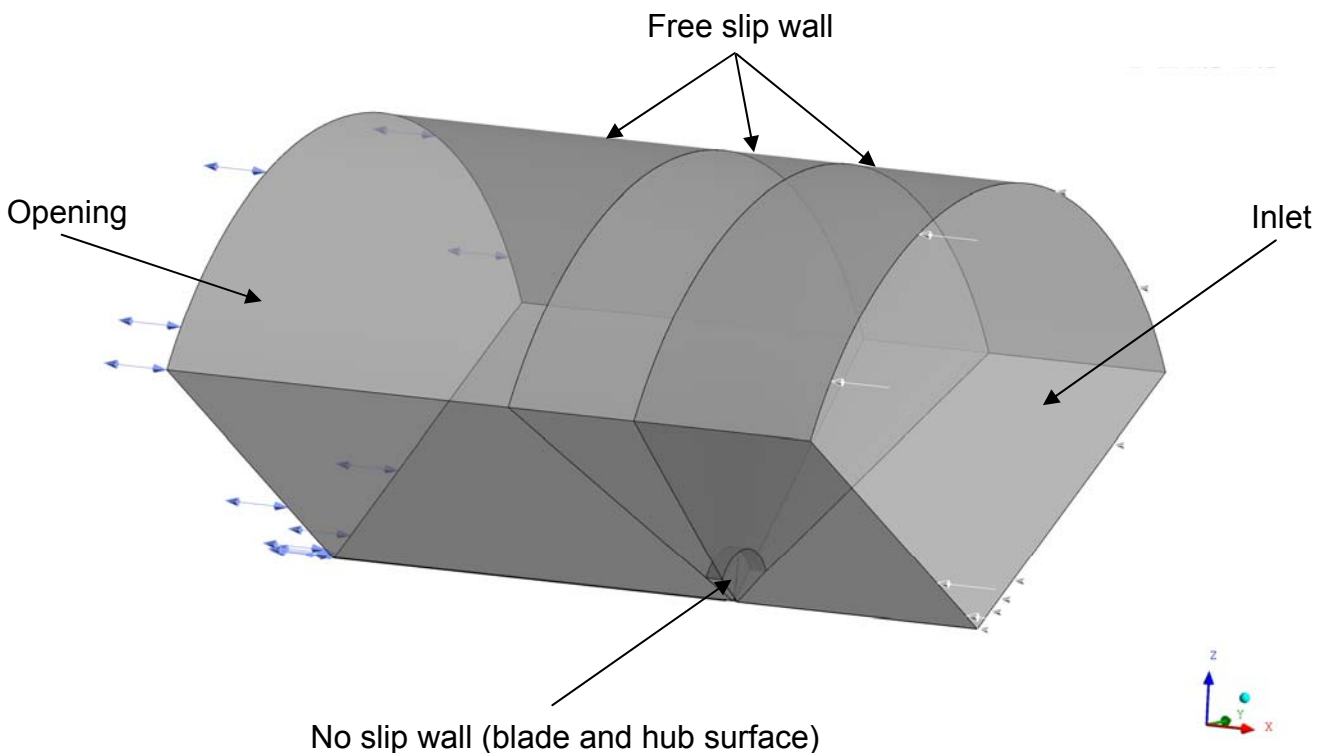


Fig. 16 Different types of boundary conditions used for the simulation

4.2 Mesh generation for the blade domain

In the present thesis the focus was set on the generation of a computational grid in an unstructured way for the part of the domain which contains the wind turbine blade (domain 4 in Fig. 13). This can be done structured or unstructured.

Structured suggests that the mesh is made of quads (2D) and cubes (3D) and “*each vertex can be readily defined as an array of indices...*” [43].

In unstructured meshes the flow region will be in general reproduced of simple elements such as triangles (2D) and tetrahedrons (3D). Unstructured meshes are usually used for arbitrarily complex geometries as it is difficult to obtain a structured mesh in an automatic manner in such cases. The procedure of generating an unstructured mesh is usually composed of four steps as presented in [43]:

1. Definition of domain boundaries
2. Specifications of an element size
3. Generation of a mesh respecting the defined domain boundaries
4. Improving mesh quality

These four steps will be discussed later in the following sub chapters.

The software used for generating the mesh was Ansys ICEM CFD 11.0, which is specialized on the generation of unstructured as well as structured grids.

4.2.1 Geometry import

The first challenge in creating an unstructured grid was the generation of an accurate geometrical copy of the considered wind turbine rotor which builds the inner boundaries of the computational domain.

The starting point consisted of simple txt-files including point coordinates of section curves of the whole blade and the hub of the rotor, created in the scope of a preliminary work [1]. A short description of the work flow and on how to extract the profile points from a CAD file could be found there. These points were imported to the 3D CAD software Pro Engineer in order to export them to a neutral data format file importable in ICEM CFD. Fig. 17 displays the lower part of the blade sections and the section of one half of the hub imported in ICEM CFD.

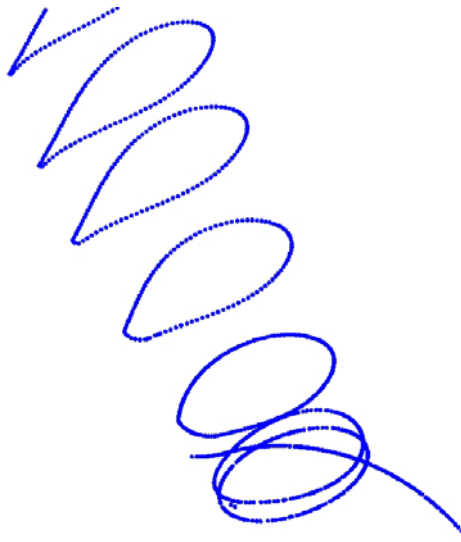


Fig. 17 Section points of the lower part of the blade and section points of the hub

The next step was to connect the imported points via splines, as shown in Fig. 18, in order to get section curves which built the basis for creating a surface of the blade and the hub.

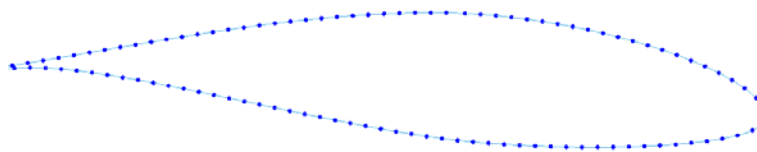


Fig. 18 Section points connected via spline curve

The trailing edge was left open because drawing the spline around it would recreate the geometry in an unrealistic way as shown in Fig. 19 right. Therefore, the trailing edge was closed by a single linear piece (cf.: Fig. 19 left).

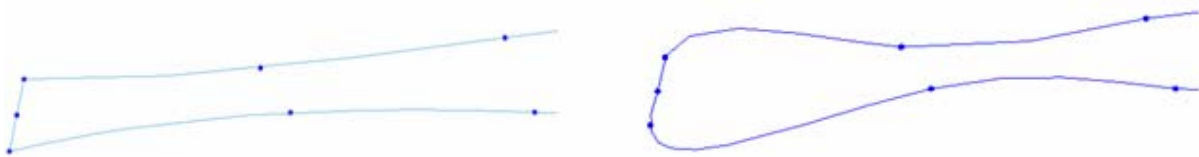


Fig. 19 Trailing edge linear closed (left), unrealistic closure by drawing spline (right)

After creating all section curves, the surface of the blade could be defined by connecting the curves previously formed. These curves were not connected with one surface extending over all curves, but the blade surface was divided into 20 segments in span wise direction. Each surface segment represents a “part” within the ICEM CFD software. The

parts at the blade surface were numbered from 1-20 whereas the lowest part at the hub represented part number 1 and the part at the tip number 20.

The hub surface was created by rotating the section curve about 120° around the axis of rotation of the blade. Also, the hub surface was dedicated as a particular part.

The result of the generated blade and hub surface is displayed in Fig. 20, where each coloured section represents a single part.

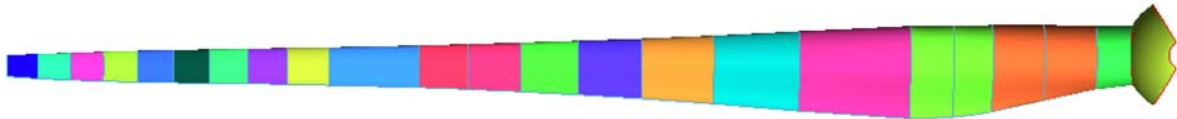


Fig. 20 Completed surface generation of the blade and hub

The partitioning of the blade surface in 20 sections was necessary, as the later defined element size of the grid differed in span wise direction. To define different element sizes for the grid generation, different parts needed to be created as each single part can be allocated to a dedicated element size.

In order to fit exactly, the outer boundary of the blade domain was given by the domains surrounding the blade domain. So, the surrounding contour was rotated around the axis of rotation of the blade (in the same way as it was done for the hub) to build the surrounding surface. Fig. 21 displays the blade inside the surrounding surface, simplified as the black wireframe.

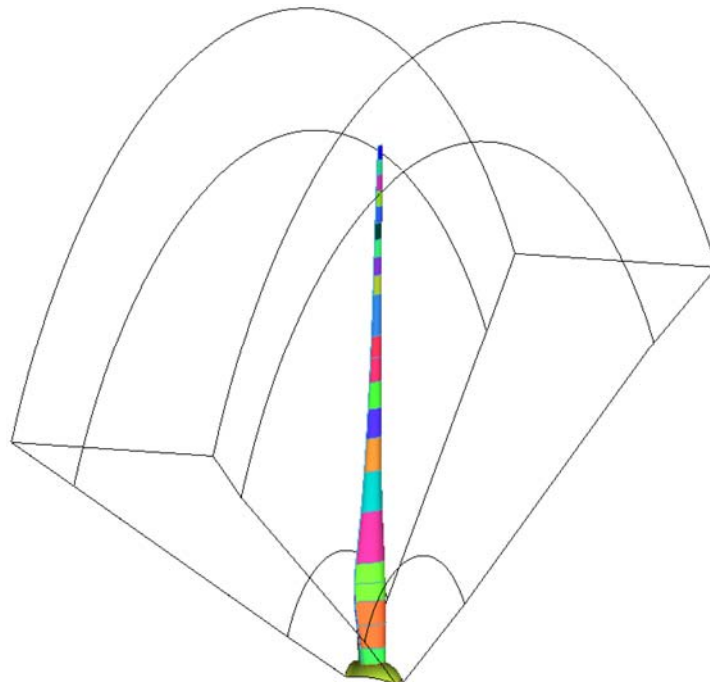


Fig. 21 Blade inside wireframe of surrounding surface

4.2.2 Specification of different element sizes

In order to reproduce the surface of the blade and the hub with the elements in a realistic way, the lower, thicker part of the blade was covered by larger elements and the element size was reduced continuously towards the tip. The upper part of the blade shows much more curvature and thus smaller elements were needed there, especially in the region of the leading edge.

Fig. 22 displays the lower part and the hub region of the blade, covered by larger elements with a size of 200 mm. Fig. 23 displays the upper part of the blade, where the element size is reduced from 200 mm at the right side to 50 mm at the tip on the left side.

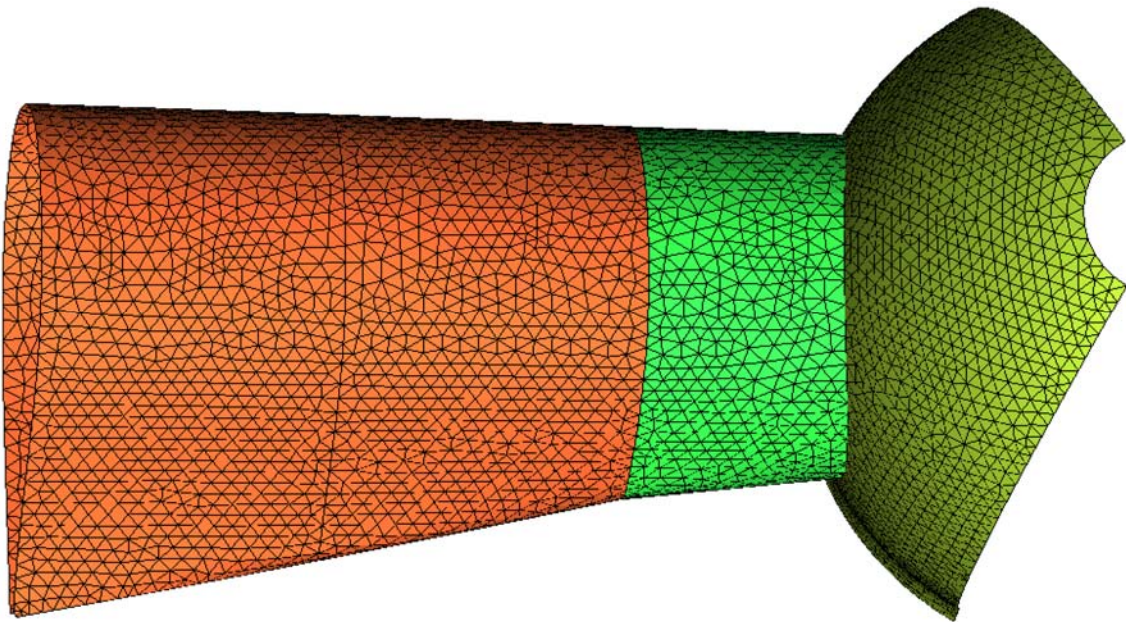


Fig. 22 Lower part of the blade and hub (element size 200 mm)

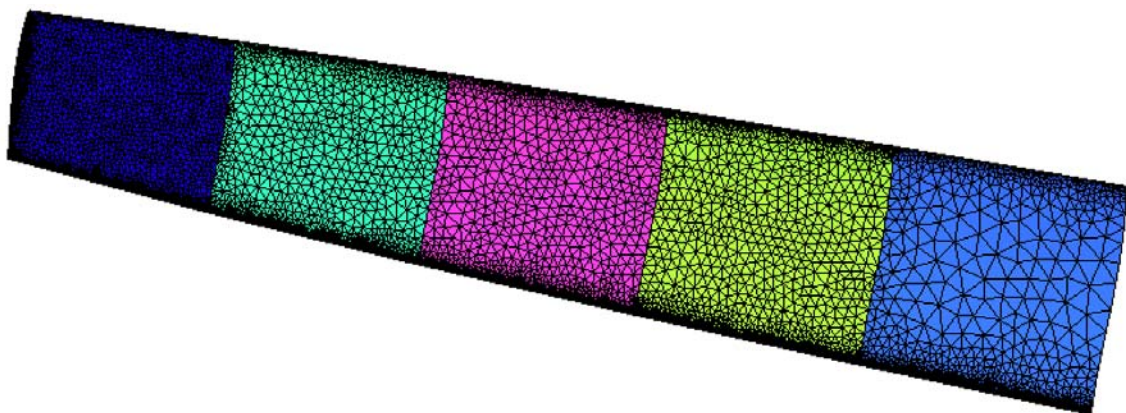


Fig. 23 Upper part of the blade (element size from left to right 50 mm-200 mm)

The target was to rebuild the blade surface as realistically as possible, in accordance to the available main memory (3,46 GB RAM) of the desktop PC used for mesh generation. If the mesh size was defined to small the total number of elements increased strongly, the software ran out of memory and shut down during the mesh generation process.

Another factor contributing to the success of grid generation is the global mesh size, which has to be defined. The global mesh size defines the size of the elements away from surfaces where element size is defined separately - as it had been made for the surface of the blade and hub. A global mesh size of 1500 mm resulted to be adequate with respect to the total amount of elements computable by the used desktop PC. Table 1 outlines the different mesh sizes applied to different parts.

Table 1 Overview of global mesh size and part mesh size

Mesh size [mm]	
Global mesh size	1500
Parts	
Hub	200
Blade segment 1-16	200
Blade segment 17-19	75
Blade segment 20	50
Blade tip	30

4.2.3 Special treatment of the leading and trailing edge

The leading edge of the blade held the strongest curvature all along the blade, especially at the upper part toward the blade tip. Hence, the element size on the leading edge was treated separately. This was done by creating curves resting on the leading edge. In ICEM CFD every single curve can be treated with a curve mesh setup. The curves on the leading edge were placed within the same segments as well as the surface parts of the blade. This way, for each curve the maximum element size could be specified. Fig. 24 shows the refined leading edge for one segment of the blade. The leading edge is marked by the red line.

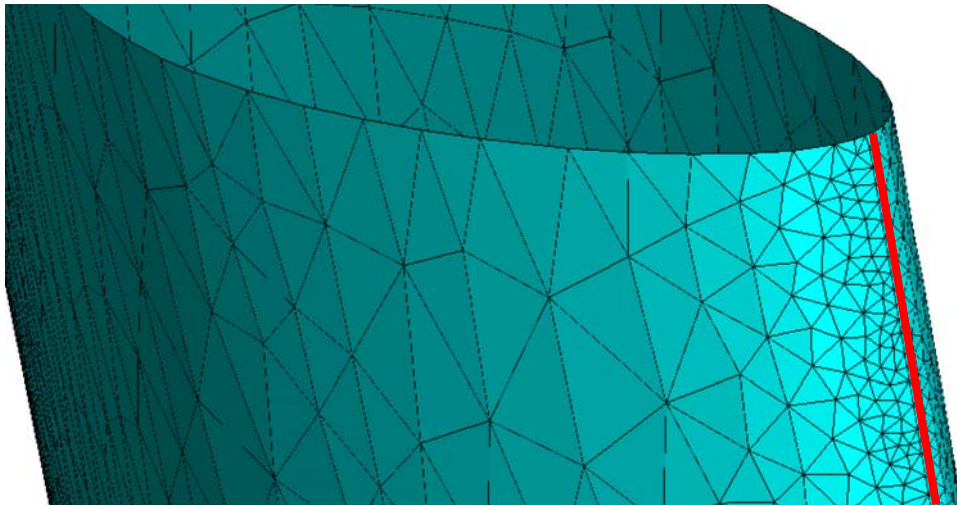


Fig. 24 Refined leading edge marked by the red line

The same procedure was applied to the trailing edge. However, the trailing edge was more difficult to refine since the trailing edge is very narrow against the element size beside. The aim was, to place at least three elements on the trailing edge. This could be realized, except for the topmost segment, where the width of the trailing edge was about 4,4 mm. At the trailing edge curves were placed also within the blade surface segments to define the maximum element size. The result for the topmost part of the blade is displayed in Fig. 25.

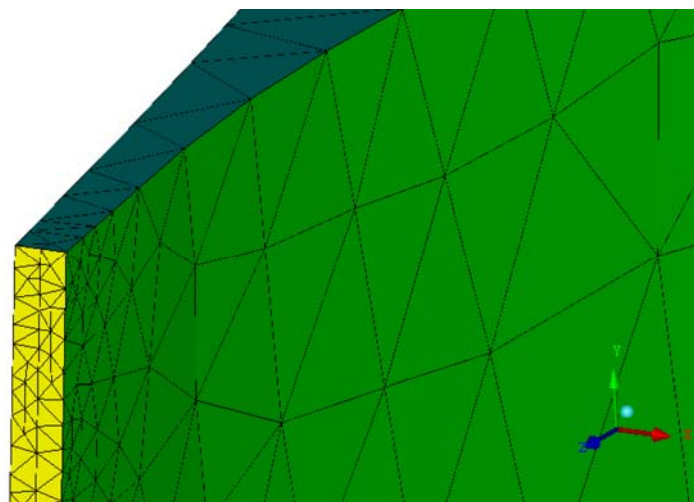


Fig. 25 Refined trailing edge marked in yellow

4.2.4 Near wall treatment of the mesh

In order to fulfil the required near wall resolution of the turbulence models used it was necessary to refine the elements at each non-slip wall. This was done by extruding prism layers from each wall. For each part as defined above, the initial height of the first prism layer at the wall was specified. Furthermore, the number of prism layers and the growth rate had to be specified. Thus, the whole blade and the hub were covered by prism layers. The initial height of the first layer was determined in terms of the estimated boundary layer thickness in order to place at least 10 layers within the boundary layer. This was done by using the guidelines for mesh generation given in [42].

The guideline is based on the theory for a flat plate however, it seemed to be a good compromise since the airfoil of the blade is quite flat in relation to the chord length, especially at the upper parts of the blade.

So, for each blade section the Reynolds number was calculated by means of

$$\text{Re}_c = \frac{\rho V_{rel} C}{\mu} \quad (6)$$

with the chord length C of the particular section and V_{rel} as relative velocity to the blade section simplified calculated as a vector product of circumferential speed and wind speed.

Now, the boundary layer thickness was estimates with

$$\delta = 0,035C \text{Re}_c^{-1/7} \quad (7)$$

proposed in [42].

So, it was possible to calculate the initial height of the first prism layer at the wall of the blade in order to fulfil the goal of at least 10 layers within the boundary layer. Since the height of the prism layers grows following the exponential law (geometric series)

$$H = \Delta y_1 \frac{r^n - 1}{r - 1} \quad (8)$$

with H as total height of all layers, Δy_1 as initial height of the first layer, r as expansion factor and n as number of layers. This formulation was formed to Δy_1 and the total height H was replaced by the formerly calculated boundary layer thickness. The number of layers

was set to the desired value and so the initial height Δy_1 was calculated to be specified for each part of the blade surface.

With the calculated initial height it was possible to estimate the dimensionless wall distance y^+ with the correlation

$$\Delta y_1 = C y^+ \sqrt{80} \text{Re}_c^{-13/14} \quad (9)$$

given in [42], yielded from the correlations for a flat plate.

So, the y^+ value was estimated as well to check whether it is within the correct range required for the chosen turbulence models.

For these calculations an excel spreadsheet was prepared. The input parameters were:

- blade section radius and associated chord length
- wind speed
- rotational speed
- air properties (density, viscosity)
- expansion factor for the prism layers
- desired number of layers within the boundary layer.

This spreadsheet is enclosed on a CD at the end of this paper.

At this point, knowing the initial height of the first prism layer, three different grids were generated. A coarse mesh with 5 prism layers, a middle mesh with 10 prism layers within the estimated boundary layer thickness and a fine mesh with 15 prism layers within the estimated boundary layer thickness.

Generating at five prism layer first and then splitting afterwards each layer into two or three has proved to be a robust method. This was done, because generating 15 layers at a stroke was not stable often and yielded software overload.

Fig. 26 shows the complete mesh around a blade section and Fig. 27 the detailed view of the prism layers surrounding the blade at the trailing edge.

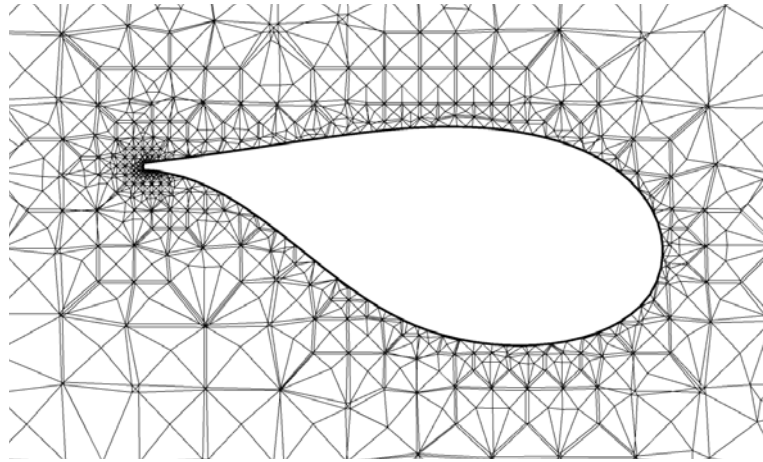


Fig. 26 Unstructured mesh around blade section

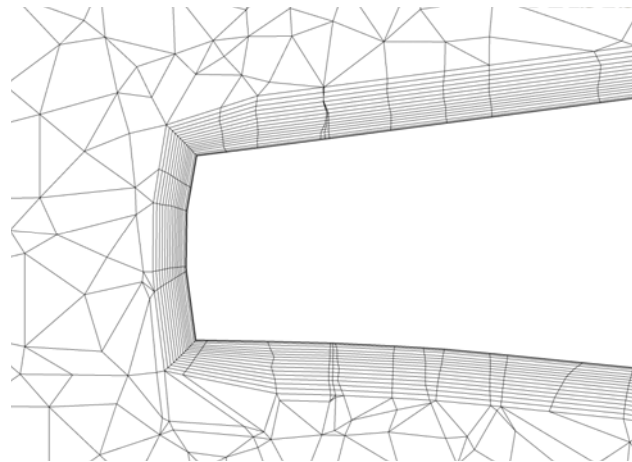


Fig. 27 Detailed view of the prism layers surrounding the surface of the blade

In Table 2 an overview of the calculated values for 5 prism layers within the boundary layer is given. δ is the calculated boundary layer thickness, Δy_1 the height of the first layer and y^+ the dimensionless wall distance. The total height in the last column is the height of all prism layers which is smaller than the boundary layer thickness in order to ensure that all layers are within the boundary layer.

Table 2 Overview of the calculated values for 5 prism layers within the boundary layer

Distance from the root [m]	Blade segment	δ [mm]	Calculated		Applied		Total height [mm]
			Δy_1 [mm]	y^+	Δy_1 [mm]	y^+	
2	1-4	11,02	1,48	38	1,5	36	10,42
4		12,38	1,66	53	1,5	48	11,16
6		13,72	1,84	72	1,5	59	11,16
8		14,11	1,90	89	1,5	70	11,16
10		13,49	1,81	100	1,5	83	11,16
12		12,38	1,66	106	1,5	95	11,16
14		11,25	1,51	109	1,5	108	11,16
16	5-7	10,21	1,37	111	1	81	7,44
18		9,28	1,25	112	1	90	7,44
20		8,46	1,14	112	1	99	7,44
22		7,74	1,04	112	1	108	7,44
24	8-10	7,11	0,96	112	0,8	93	5,95
26		6,56	0,88	111	0,8	101	5,95
28		6,09	0,82	110	0,8	108	5,95
30	11	5,70	0,77	110	0,7	101	5,21
32		5,38	0,72	111	0,7	107	5,21
34	12-14	5,12	0,69	111	0,6	97	4,46
36		4,90	0,66	112	0,6	102	4,46
38		4,66	0,63	113	0,6	108	4,46
40	15-17	4,34	0,58	110	0,5	95	3,72
42		3,89	0,52	104	0,5	100	3,72
44	18	2,92	0,39	83	0,3	64	2,23
45	19	1,37	0,18	43	0,18	42	1,34
45,3	20	0,73	0,10	24	0,09	22	0,67

4.2.5 Mesh quality

The most relevant measures for the mesh quality are the maximum aspect ratio, the minimum orthogonality angle and the maximum mesh expansion factor. These measures are responsible for the accuracy of the results and the stability of the solver run.

The aspect ratio is defined by the maximum to the minimum surface area of a control volume as displayed in Fig. 28.

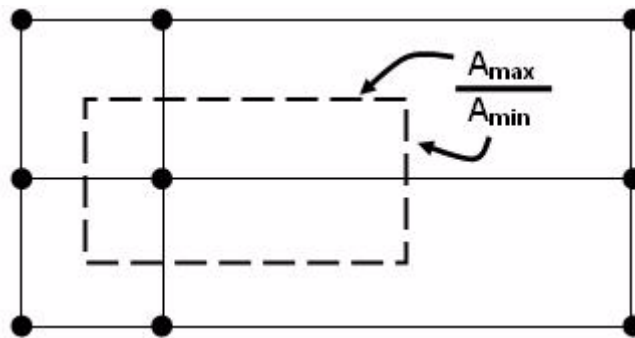


Fig. 28 Description of aspect ratio [42]

The minimum orthogonality angle describes the angle between two adjacent element surfaces and the mesh expansion factor describes the rate of change of adjacent element volumes [42].

An overview of the grids generated for the blade domain is given in Table 3. The figures highlighted in red overshoot the recommended maximum values. However, it was not possible to generate a finer grid since the memory of the workstation used for the grid generation did not allow for more elements. So, a compromise to satisfy the number of nodes within the boundary layer as well as the recommended y^+ values had to be made. It should also be noted that the mesh generation procedure was very complicated due to the instability of the software and the time demand to compute a grid successfully. The average time for generating a grid was about one hour, and often it was accompanied by sudden software shut downs during the saving process, so that the grid had to be computed again. In spite of the bad mesh quality, all unstructured generated grids yielded a stable solution after approximately 50-150 iterations.

Table 3 Overview of generated mesh types

Type:	Prism layers:	Average y^+	Elements	Nodes	Min. orthogonality angle	Max. aspect ratio	Max. mesh expansion factor
Coarse	5	80	$6,4 \cdot 10^6$	$1,6 \cdot 10^6$	17°	280	167
Middle	10 within BL	30	$7,7 \cdot 10^6$	$2,2 \cdot 10^6$	11°	1222	954
Fine	15 within BL	18	$9,1 \cdot 10^6$	$2,9 \cdot 10^6$	10°	2017	1400

5 Results

This chapter describes the process of analysing the conducted simulations. The challenge has been to decide which quantities have to be considered for an adequate analysis. Therefore, the review in chapter two gave an excellent insight into which quantities are recommendable.

In order to get useful values all graphs depicted are related to coordinate systems which are placed at the given airfoil sections by AMSC Windtec GmbH.

5.1 Observed and calculated quantities

At this point, gathered quantities and their calculation for the evaluation of the turbulence models are described.

A significant focus in the evaluation process was set to the mechanical power of the examined wind turbine. By monitoring the torque T_{blade} around the axis of rotation and multiplying it with the number of blades z and the angular velocity ω , the mechanical power P_{mech} was calculated.

$$P_{\text{mech}} = zT_{\text{blade}}\omega \quad (10)$$

Quantities plotted against the normalized chord

The quantities which were plotted against the normalized chord have been analysed at four selected radial positions in order to show best differences among the turbulence models considered. The positions were at 5,275 m, 17,275 m, 31,275 m and 43,275 m, which are equal to 4 m, 16 m, 30 m and 42 m distance from the root relative to the blade. The first is selected in order to have an airfoil section near the hub, the second and third are equally located along the middle part of the blade and the fourth section is placed near the blade tip. Fig. 29 for example, displays the reference coordinate system at 16 m distance from the root, to which the analysed quantities are related. The X axis is oriented normally, the Y axis is oriented in chord direction. Fig. 30 shows the alignment of the selected radial stations along the blade.

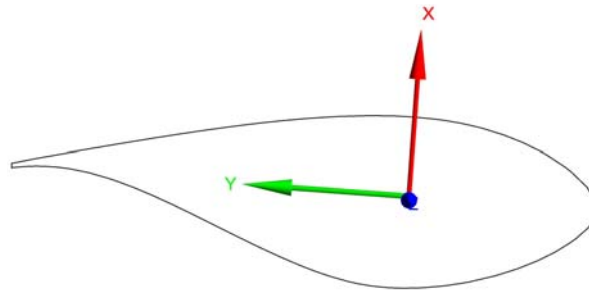


Fig. 29 Reference coordinate system at 16m distance from the root

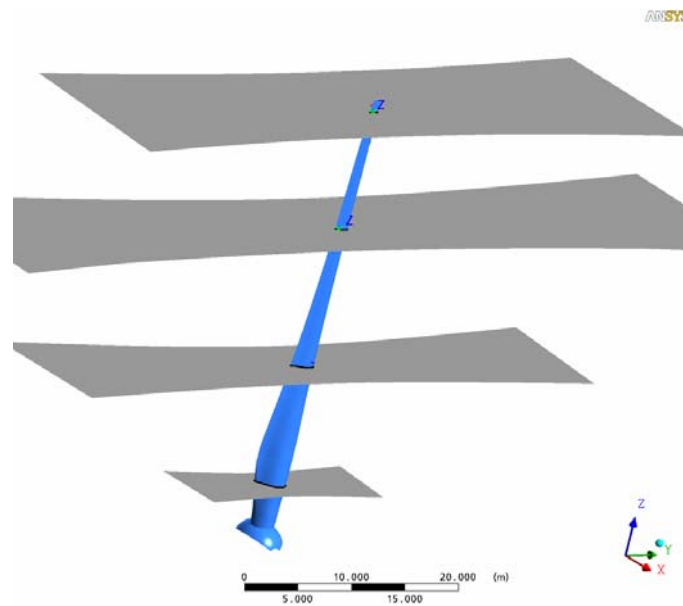


Fig. 30 Intersection planes at the selected airfoil sections

The quantities monitored were:

- pressure distribution by means of the pressure coefficient
- wall shear stress

Pressure coefficient c_p

The pressure coefficient c_p is a dimensionless figure which describes the ratio of the static pressure on a surface to the dynamic pressure of the incoming flow. So, at a stagnation point of an airfoil c_p is equal 1 as static pressure equals dynamic pressure. In the scope of this thesis the c_p value is plotted around selected airfoil sections of the wind turbine blade.

The coefficient is defined as follows whereas p is the pressure on a defined position, p_∞ is the pressure of the incoming flow in front of the airfoil section, ρ is the density and v_{rel} is the velocity of the incoming flow in front of the airfoil.

$$c_p = \frac{p - p_\infty}{\frac{\rho}{2} v_{rel}^2} \quad (11)$$

Lift and Drag coefficients

Furthermore, the lift and drag coefficients (c_L and c_D) are calculated based on the normalized forces in the X and Y direction (F_X and F_Y) at the dedicated span wise locations in combination with the additionally obtained local flow angle ϕ . The local flow angle was calculated as shown in reference [26] by determining the reduced axial velocity U_{red} in front of the blade. This was done by sweeping annular surfaces with an average radius of the selected span wise locations in stream wise direction across the rotor plane. Thus, an axial velocity distribution was gained and the axial velocity in front of the blade could be determined. See Diagram 1 for the run of the axial velocity against the axis of rotation of the wind turbine. The dotted line shows the position of the rotor plane. Furthermore, to simplify matters, U_{red} was determined by positioning the annular plane exactly in front of the blade and calculating the averaged axial velocity on it. Fig. 31 displays the comprised annular plane for determining U_{red} .

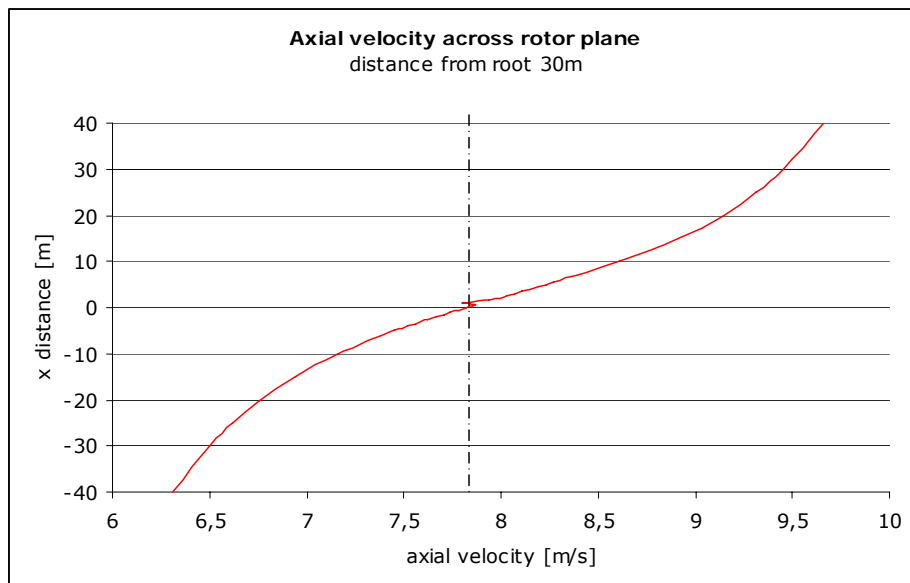


Diagram 1 Axial velocity distribution against the X direction (rotational axis of the turbine)

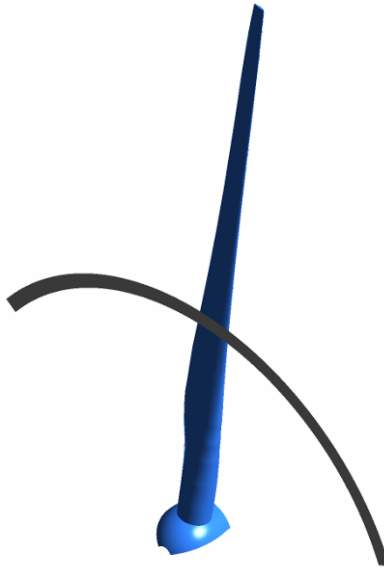


Fig. 31 Annular plane for determining the reduced axial velocity in front of the blade

This way it was possible to calculate the axial induction factor a , which is needed to account for the local flow angle ϕ . The local flow angle ϕ is the angle of the relative speed which impacts on the airfoil section due to the circumferential speed of the airfoil section and the wind speed in being the reduced axial velocity U_{red} .

The axial induction factor a and the local flow angle ϕ are expressed as follows.

$$a = \frac{U_{\infty} - U_{red}}{U_{\infty}} \quad (12)$$

$$\phi = \tan^{-1} \left(\frac{(1-a)U_{\infty}}{r\omega} \right) \quad (13)$$

At last, it was possible to calculate the angle of attack α of the dedicated airfoil section. The angle of attack α is composed of the local twist and the global pitch angle.

Results

Then, lift force F_L and drag force F_D as well as the lift and drag coefficients were calculated. As surface of reference the product of the chord length of the airfoil section and a normalized depth of 1 were presumed.

$$F_L = F_x \cos \alpha - F_y \sin \alpha \quad (14)$$

$$F_D = F_x \sin \alpha + F_y \cos \alpha \quad (15)$$

$$c_L = \frac{F_L}{\frac{\rho}{2} v_{rel}^2 A_{ref}} \quad (16)$$

$$c_D = \frac{F_D}{\frac{\rho}{2} v_{rel}^2 A_{ref}} \quad (17)$$

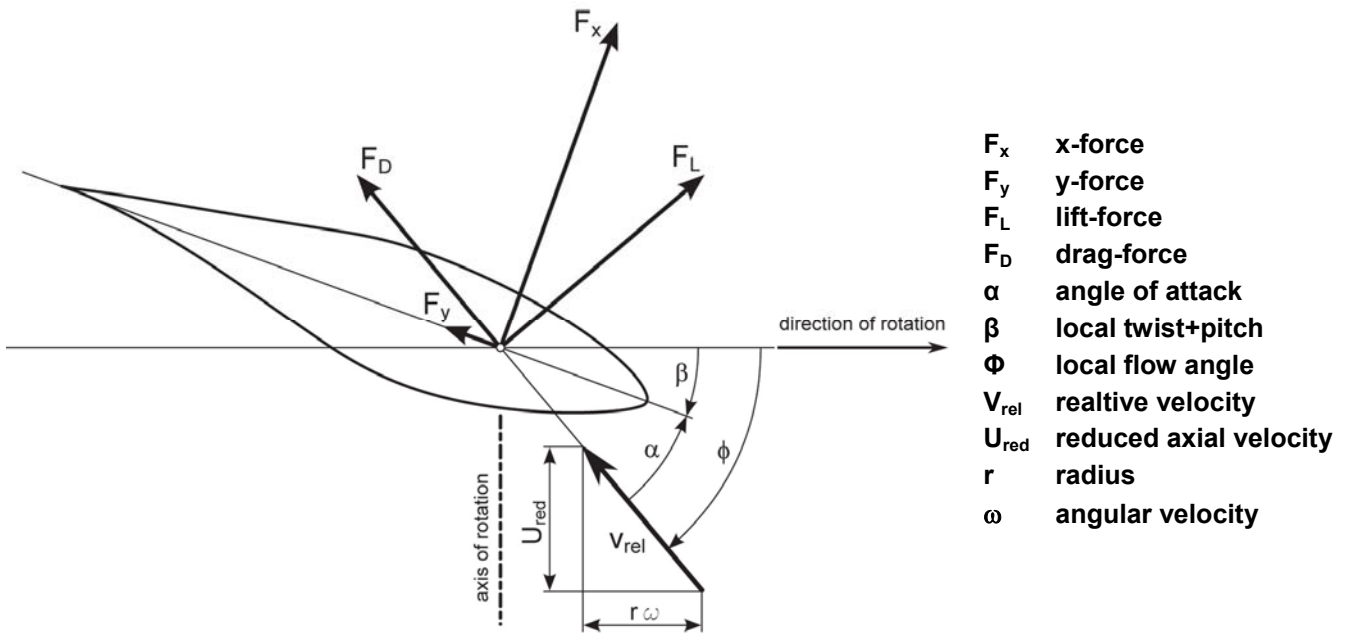


Fig. 32 Profile section with associated forces and angles

5.2 Grid dependency study

The grid dependency study should give an insight into how the different turbulence models used, behave with different mesh sizes of an unstructured mesh related to the resolution of the boundary layer. The present study is based on three meshes with different boundary layers resolved, as described in the mesh generation chapter.

Furthermore, results in combination with a structured mesh are presented to show the impact of the mesh type on the results.

In order to compare the turbulence models, the SST k/ω model is considered as the most accurate in order to get a reference for the other models. It has been chosen, because it has proved in many practical applications as mentioned in the review chapter and it is also used as the standard turbulence model of Ansys CFX 11.0 as well as of the Institute of Hydraulic Fluid Machinery at Graz University of Technology.

5.2.1 Results for the mechanical power in terms of the unstructured mesh and turbulence model used

Observing the mechanical power of the turbine, dependency of the resolution of the near wall mesh (fine, middle and coarse) is identified for the SST k/ω model, the k/ε model and the Spalart-Allmaras model. The finer the resolution, the higher the power is the tendency for these models. Contrasted, the k/ω and the BSL k/ω model behave quite similar for each mesh size. The k/ω model shows the tendency of a general overprediction, which is lowered with finer mesh sizes.

In order to get a feeling as far as the behaviour of the turbulence models due to wind condition is concerned, two boundary conditions are considered. For the global comparison of the grid dependency, boundary condition I is used. Boundary condition II is applied to the fine mesh, as it was assumed that the fine mesh provides the most accurate results. The parameters for the two boundary conditions are summarized in Table 4.

Table 4 Overview of the boundary conditions considered

	Wind speed	Rotor speed
Boundary condition I	9,75 m/s	15,7 rpm
Boundary condition II	6 m/s	10,74 rpm

At this point it is important to say that all simulations for the evaluation of the turbulence models have been carried out using a one-dimensional wind profile. It was assumed that wind speed grows following an exponential law, with the distance starting from the ground (z-direction within the computational domain). However, at one point while accomplishing this turbulence model study by studying literature and talking to colleagues it was established that the application of a wind profile on a 120° rotor segment - as used for those simulations - is not practicable, because this leads to an axial symmetric wind profile since the mechanical power of one blade is multiplied by three. And thus the calculated power becomes too high.

Another essential cause for the deviations observed is that the blade used for these simulations is about one meter shorter than the original. This reduction of the length was made at an early phase of mesh generation in taking into account the preliminary thesis [1] for this wind turbine, since problems occurred with the tapering blade tip. Geometry data were passed to this thesis and, at a later date, when all simulation runs were already performed, the length deviation was recognised.

To show the deviations a run of simulations without any wind profile and the correct blade length has been conducted as reference in combination with the SST k/ω turbulence model and for different pitch angles.

These reference simulations are summarized at the end of this chapter.

Results

Diagram 2 - Diagram 4 display the mechanical power for boundary condition I against the pitch angle with reference to the fineness of the mesh, whereas Diagram 2 represents the coarse, Diagram 3 the middle and Diagram 4 the fine mesh.

Using the coarse mesh, the highest power is predicted by the k/ω model with a deviation of about 3% to the SST k/ω model. The BSL k/ω model predicted slightly lower with regard to the k/ω but also 2,2% higher than SST k/ω . Surveying the SST k/ω and the k/ε model, both tend to predict the same power. The Spalart-Allmaras turbulence model yielded the lowest power prediction for the coarse mesh, which indicates a high sensitivity to the resolution of the near wall mesh. It deviated -1% in comparison to the SST k/ω model.

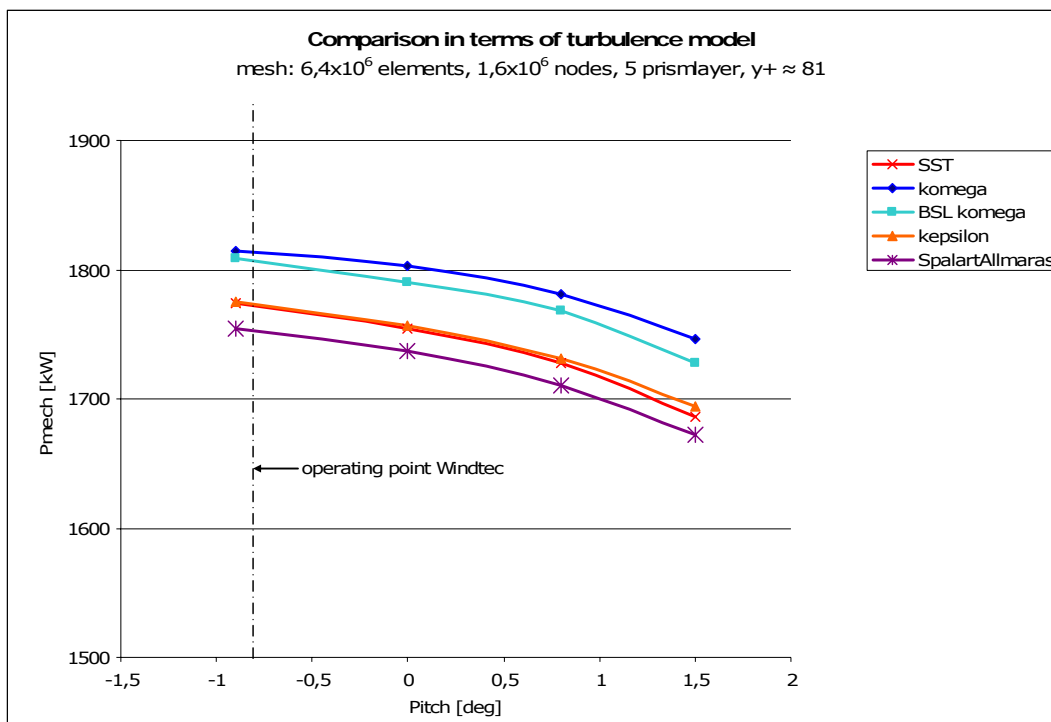


Diagram 2 Mechanical power against pitch angle, coarse mesh $y^+ = 81$ (boundary condition I)

The middle mesh showed a higher power output for all considered models than the coarse mesh, except the k/ω and the BSL k/ω model. However, the SST k/ω model yielded the lowest power. Again, the k/ω model predicted the highest power, 2,1% higher than SST k/ω model, whereas the Spalart-Allmaras model did a great jump compared to the others, 1,5% higher than SST k/ω . The k/ε and the BSL k/ω model with regard to the middle mesh predicted slightly less power than the Spalart-Allmaras model, about 1% compared to the SST k/ω .

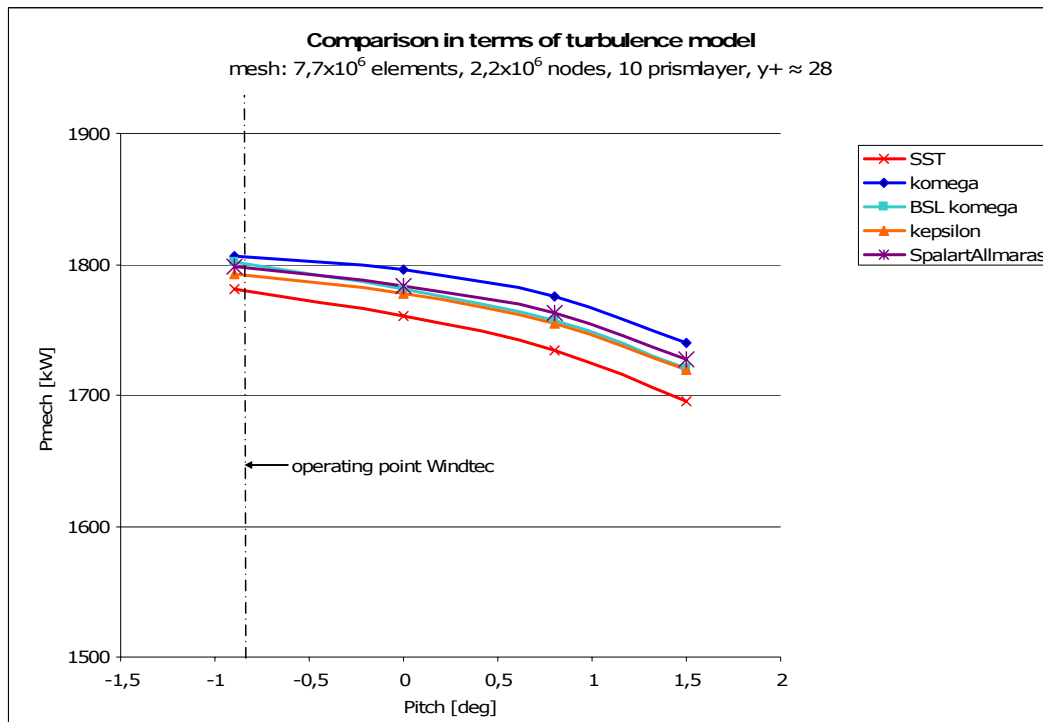


Diagram 3 Mechanical power against pitch angle, middle mesh $y+ = 28$ (boundary condition I)

The fine mesh resulted in the highest predicted power for the SST k/ω , k/ϵ and the Spalart-Allmaras model. The Spalart-Allmaras model again did a step up and combined with the fine mesh predicted 1,8% more power than the SST k/ω model. The power for the k/ω is 1,5% higher and the k/ϵ and the BSL k/ω model predicted nearly the same power in a range of 0,6% above the SST k/ω model. Also, a Reynolds Stress model was used to calculate the flow in conjunction with the fine mesh. This resulted in a mechanical power - 4,5% below the SST k/ω model. The fine mesh was considered also for a laminar simulation, because, theoretically, the flow around the wind turbine profile can mostly be considered as laminar. This yielded a higher power for higher pitch angles. However, at the lowest pitch angle the laminar simulation predicts the same power as for the k/ω model. A lower pitch angle leads to a higher angle of attack, whereas the reason for this could be that the laminar boundary layer is not able to override high pressure gradients compared to a turbulent boundary layer. Compare Diagram 4 for the above mentioned facts.

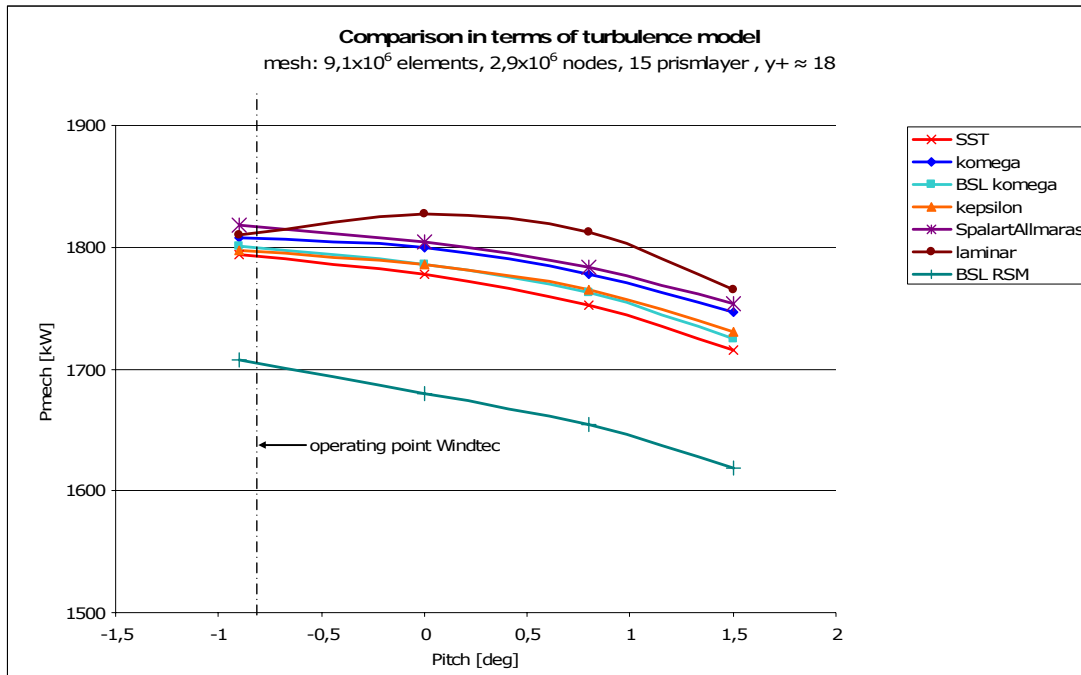


Diagram 4 Mechanical power against pitch angel, fine mesh $y^+ = 18$ (boundary condition I)

In Table 5 the deviations in comparison to the SST k/ω model are listed to give an adequate overview. It is clearly identified that the fine grid results in the lowest deviation among the turbulence models considered.

Table 5 Overview of the deviation of the models in comparison to the SST k/ω model (boundary condition I)

Turbulence model	coarse	middle	fine
k/ω	3%	2,1%	1,3%
BSL k/ω	2,2%	1,3%	0,5%
k/ϵ	0,2%	1%	0,6%
Spalart-Allmaras	-1%	1,5%	1,7%

Diagram 5 displays the variation of the predicted power in terms of the used mesh size, summarized for all turbulence models considered. Again the independency of the wall resolution of the k/ω and the BSL k/ω model is depicted. The Spalart-Allmaras model shows the greatest dependency while the SST k/ω and the k/ϵ model behave quite the same. At this point, it is important to say that the overall deviation of the models is very small if one considers that the diagrams zoom into a small power range.

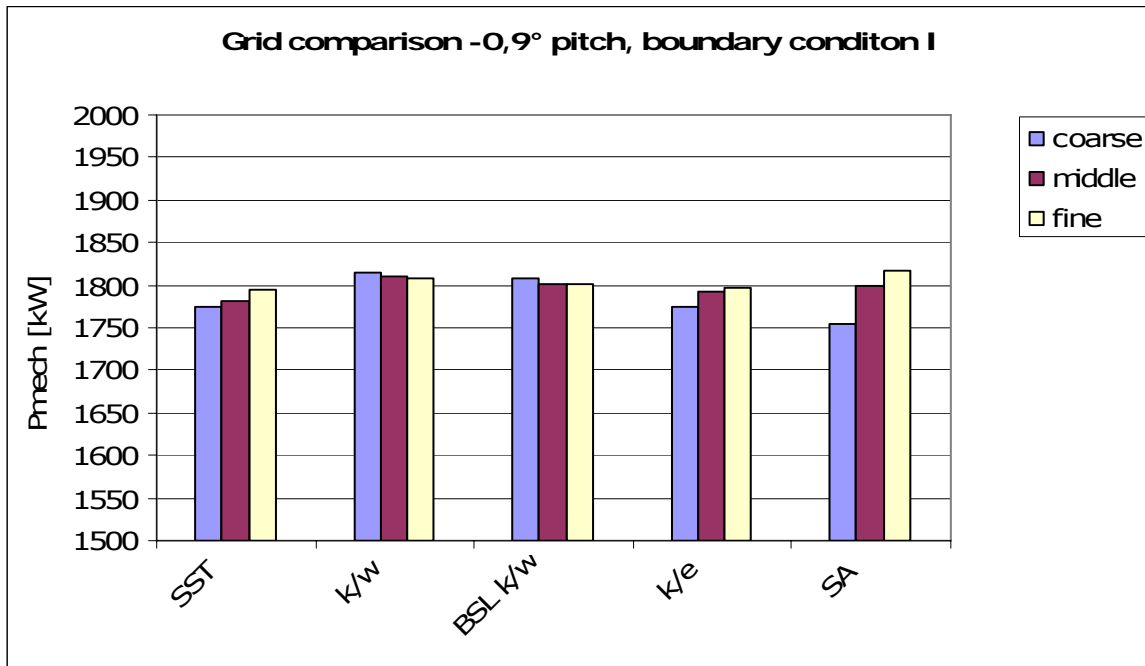


Diagram 5 Variation of the computed power for each turbulence model in terms of the used mesh (boundary condition I)

For the fine grid the second boundary condition was implemented in order to get an insight into the behaviour of the turbulence models with regard to lower wind speed. The operating point of the observed wind turbine for this condition is at 0,0° pitch angle. The results for the second boundary condition are displayed in Diagram 6. Again, the Spalart-Allmaras model predicted the highest power output as observed for boundary condition I applied to the fine mesh (cf. Diagram 4). The other models predict the mechanical power quite similar, within a range smaller than 1%.

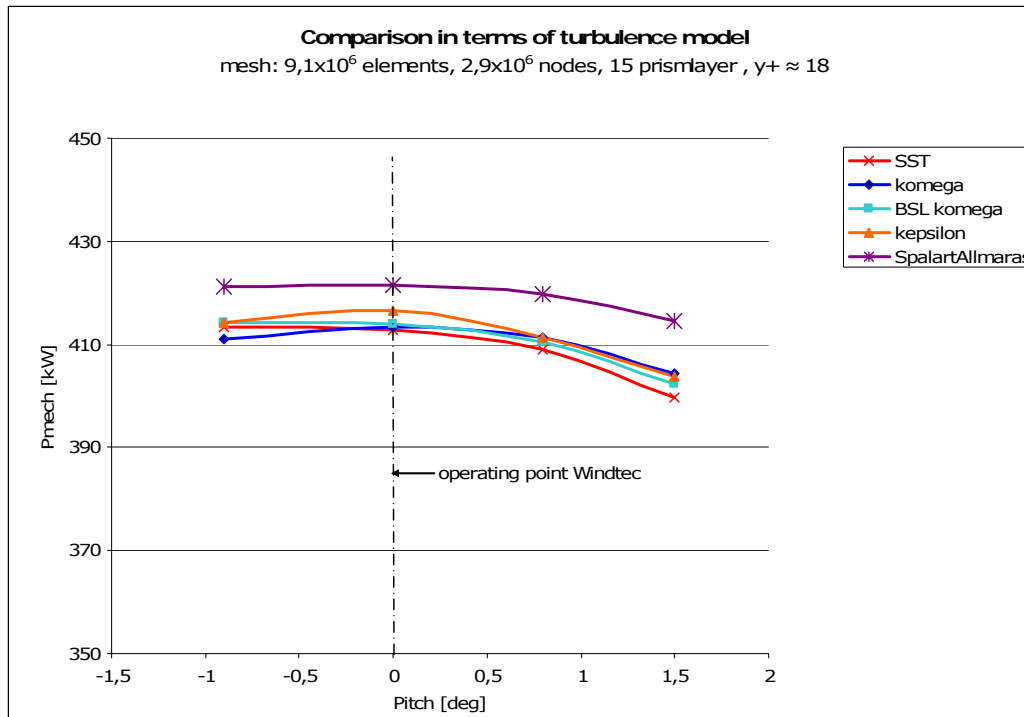


Diagram 6 Mechanical power against pitch angle, fine mesh $y^+ = 18$ (boundary condition II)

Again the deviations among the turbulence models are summarized in Table 6. It is clearly visible that the turbulence models do not deviate as strong as shown for boundary condition I at lower wind speeds, except the Spalart-Allmaras model.

Table 6 Overview of the deviation of the models in comparison to the SST k/ω model (Boundary condition II)

Turbulence model	Fine mesh
k/ω	0,3%
BSL k/ω	0,4%
k/ϵ	0,7%
Spalart-Allmaras	2,6%

5.2.2 Results for the mechanical power in terms of a structured mesh and turbulence model

Furthermore, a series of calculation runs has been performed in combination with a structured mesh, which resolves the geometry of the blade much finer than the finest unstructured mesh. The structured mesh was produced within a preliminary work [1].

However, the maximum aspect ratio was about ten times higher and the maximum mesh expansion factor was virtually twice as high as the already high values of the unstructured mesh. Therefore, it was not possible to run simulations with regard to the k/ϵ model and the Reynolds Stress model, as the simulation runs were terminated prematurely due to error messages. The feasible simulations have been performed for the $-0,9^\circ$ pitch angle in combination with boundary condition I, because this point is around the operating point of the wind turbine examined.

The deviation of the predicted mechanical power among the turbulence models is quite the same as observed for the unstructured mesh, but the power is about 9% higher (cf.: Diagram 7). This higher power output seems to be more realistic when comparing the results to a BEM calculation realized by AMSC Windtec GmbH. Table 7 shows the deviations with respect to the SST k/ω model.

Table 7 Overview of the deviation of the models in comparison to the SST k/ω model (structured mesh, boundary condition I)

Turbulence model	Structured mesh
k/ω	1,9%
BSL k/ω	2,1%
Spalart-Allmaras	1,9%

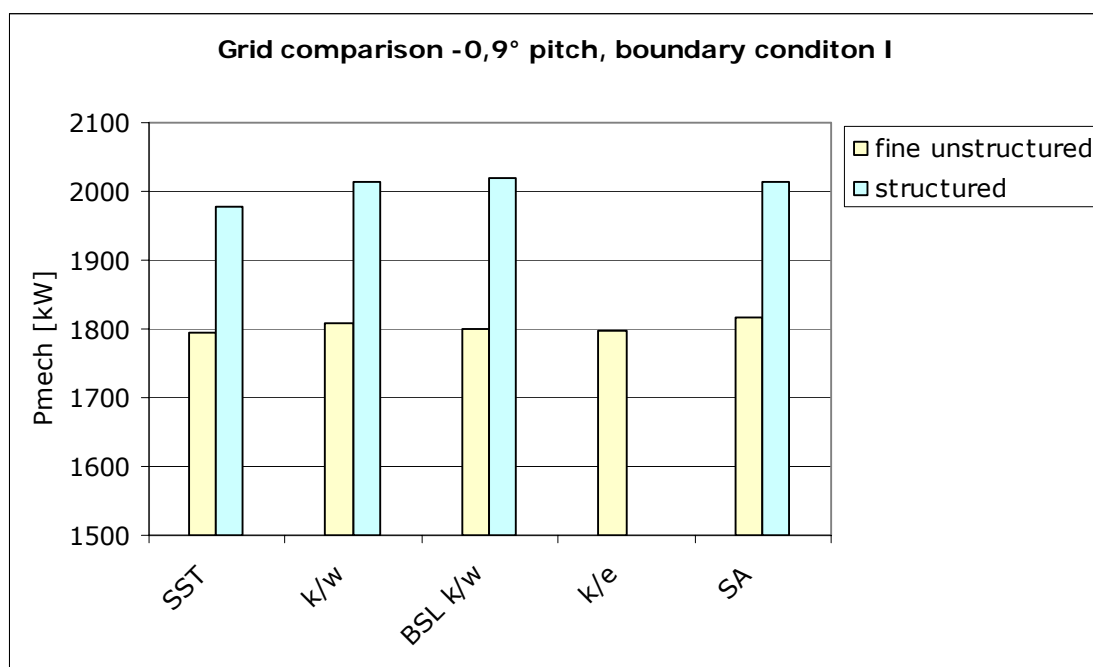


Diagram 7 Variation of the computed power for each turbulence model in comparison to the structured / unstructured mesh (boundary condition I)

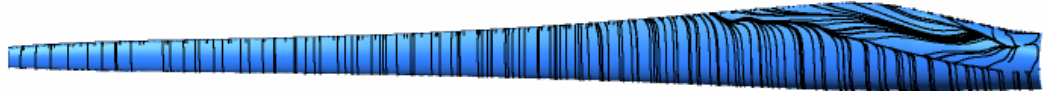

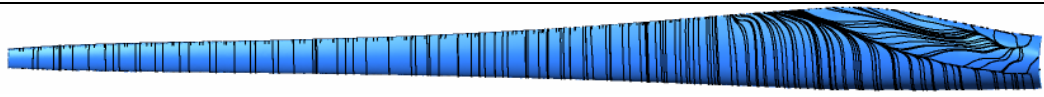
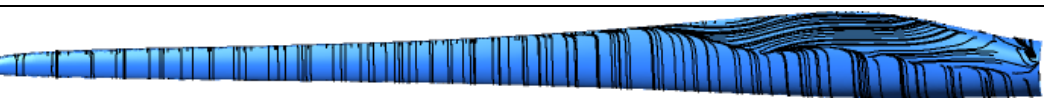
5.2.3 Streamline plots on the suction side of the blade

The focus here is set on surfaces streamlines in order to see how the different turbulence models predict the 3D effects which occur at the inboard sections of the blade.

The streamline plots displayed in Table 8 to Table 12 are related to boundary condition I at $-0,9^\circ$ pitch angle.

The SST k/ω model does not tend to different amounts of 3D flow due to the different grid resolutions. The fine and the middle mesh nearly predicted an equal amount of the 3D effect, whereas in combination with the coarse mesh a small increase is recognisable. The lower 3D effect of the fine mesh confirms the increase of the mechanical power which is observed from the coarse to the middle mesh as the 3D effect is a loss which negatively affects the flow around the blade. However, the SST k/ω model in combination with the structured mesh predicted the greatest amount of the 3D effect. Table 8 displays the above-mentioned observations.

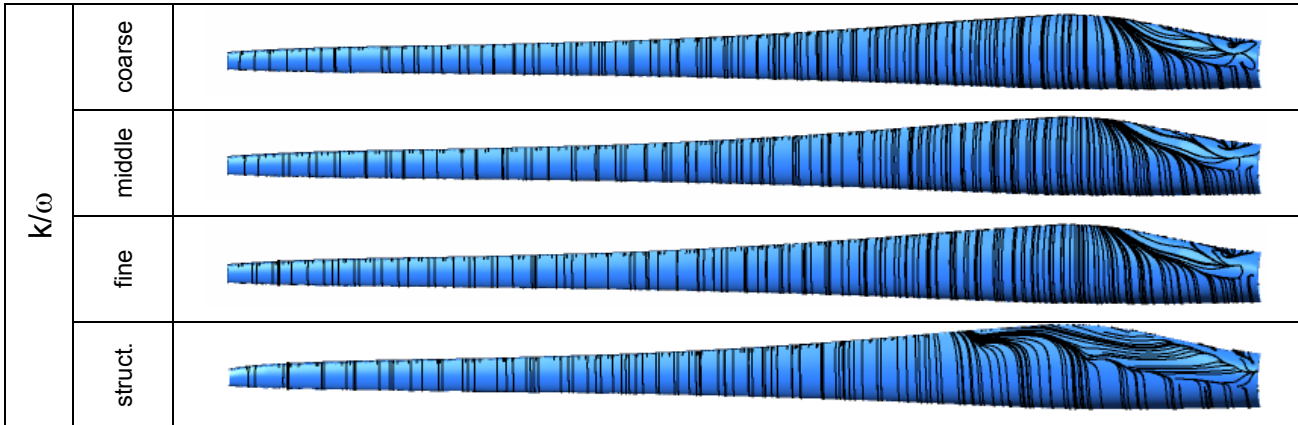
Table 8 Streamlines on suction side for the SST k/ω turbulence model in terms of the used mesh (boundary condition I, $-0,9^\circ$ pitch)

SST k/ω	coarse	
	middle	
	fine	
	struct.	

Results

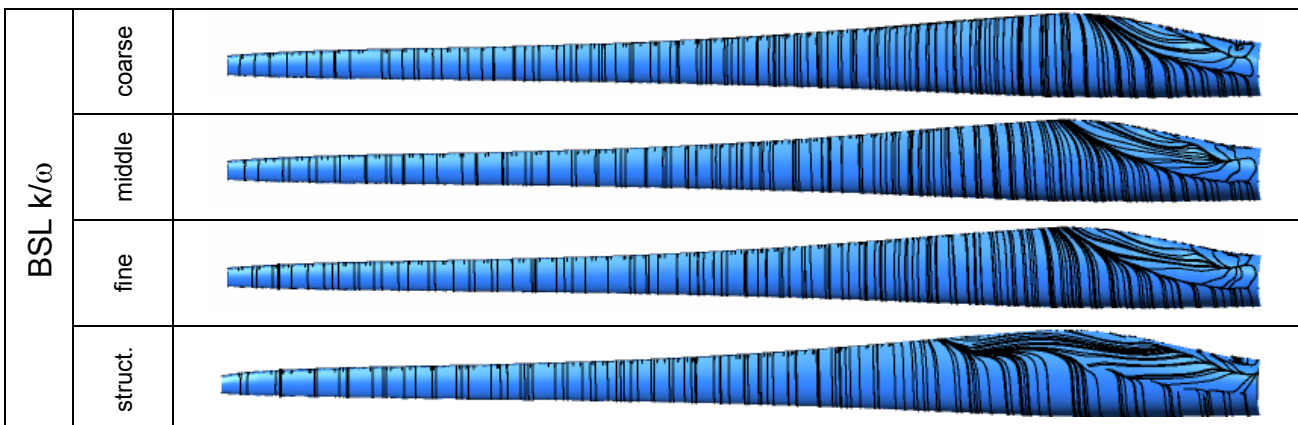
The k/ω model predicted the lowest amount 3D effects of all turbulence models considered. This goes along with the high mechanical power predicted for this model, as of the low loss due to the 3D effect. See Table 9 for comparison.

Table 9 Streamlines on suction side for the k/ω turbulence model in terms of the used mesh (boundary condition I, $-0,9^\circ$ pitch)



The BSL k/ω model shows a little more 3D flow at the inboard section of the blade than the k/ω model, but also a small amount of separation compared to the SST k/ω model. Again, the structured mesh yielded a greater expansion of the 3D effect, as shown in Table 10.

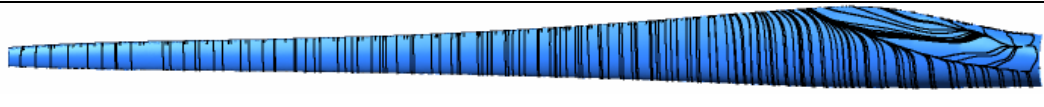
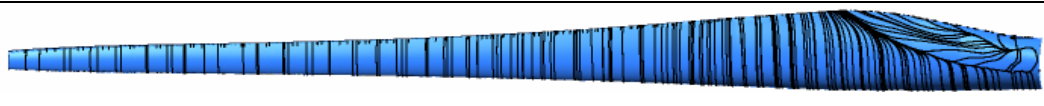
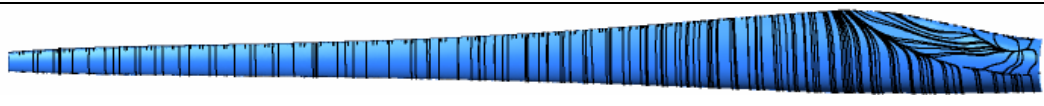
Table 10 Streamlines on suction side for the BSL k/ω turbulence model in terms of the used mesh (boundary condition I, $-0,9^\circ$ pitch)



Results

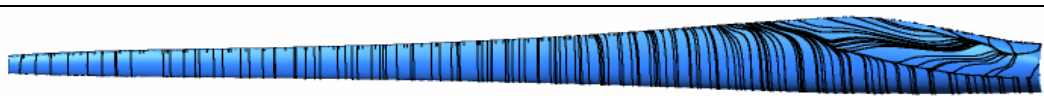
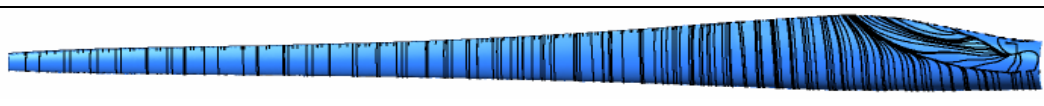

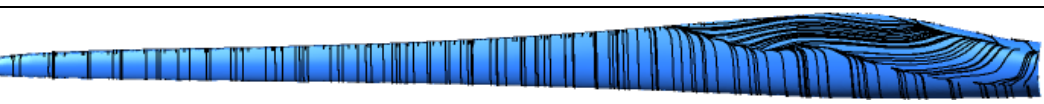
The value of the 3D cross flow predicted in combination with the k/ε model is very similar to the BSL k/ω model. Differences concerning grid resolution are just recognisable for the coarse mesh as shown in Table 11.

Table 11 Streamlines on suction side for the k/ε turbulence model in terms of the used mesh (boundary condition I, $-0,9^\circ$ pitch)

k/ε	coarse	
	middle	
	fine	
	struct.	-

The Spalart-Allmaras model predicts the strongest amount of 3D flow in arrangement with the coarse mesh, which yielded the lowest mechanical power in combination with this model. In connection with the middle and fine mesh, the calculated 3D flow remained in the same level. The structured mesh yields a 3D flow in a high gear, quite similar to the SST k/ω model in arrangement with the structured mesh.

Table 12 Streamlines on suction side for the Spalart-Allmaras turbulence model in terms of the used mesh (boundary condition I, $-0,9^\circ$ pitch)

Spalart-Allmaras	coarse	
	middle	
	fine	
	struct.	

5.2.4 Pressure coefficient at 4 m airfoil section

Looking at the pressure coefficient c_p with reference to the different mesh types used shows that there are some small deviations among the unstructured mesh types (coarse, middle, fine). For this overview the airfoil section at 4 m distance from the root has been chosen, as at higher radial distances the deviations among the mesh types are decreasing and nearly not recognisable.

With the SST k/ω model the strongest suction peak was predicted in combination with the coarse unstructured mesh, while the structured mesh featured a higher pressure coefficient (lower depression) on the first half of the suction side. In the area of the trailing edge ($Y_{\text{norm}} = 1$) of the blade section another, smaller suction peak is recognisable for the pressure side of the blade section, which is highest for the structured mesh, followed by the middle, fine and coarse unstructured meshes. In regions, where high pressure gradients occur, it seems to be important to resolve the near wall region fine in order to get accurate results. In general, it could be said that the difference between the middle and fine unstructured meshes is small compared to the coarse one. Diagram 8 depicts the above remarks.

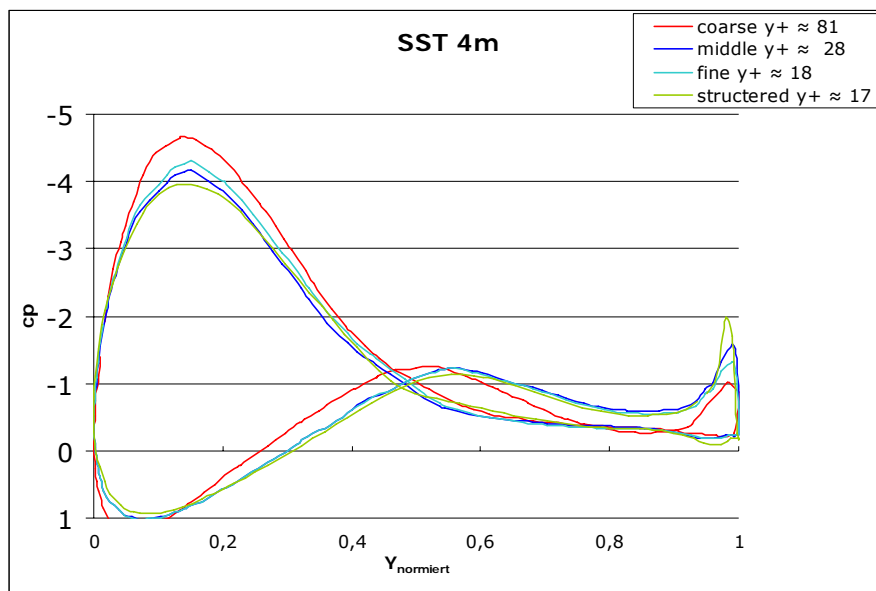


Diagram 8 Pressure coefficient c_p for different mesh types used in combination with the SST k/ω model

With the k/ω model, again, the highest suction peak was predicted for the coarse mesh, the structured mesh yielded a lower depression, until $Y_{norm} = 0,6$ at the suction side, and the strongest suction peak at the trailing edge (cf.: Diagram 9). The middle and fine unstructured meshes show the same tendency as detected for the SST k/ω model. However, the magnitude of the suction peak is higher for all unstructured mesh types compared to the SST k/ω model. The same statement can be made for the BSL k/ω model shown in Diagram 10, whereas the magnitude of the suction peak is slightly lower than that for the k/ω model.

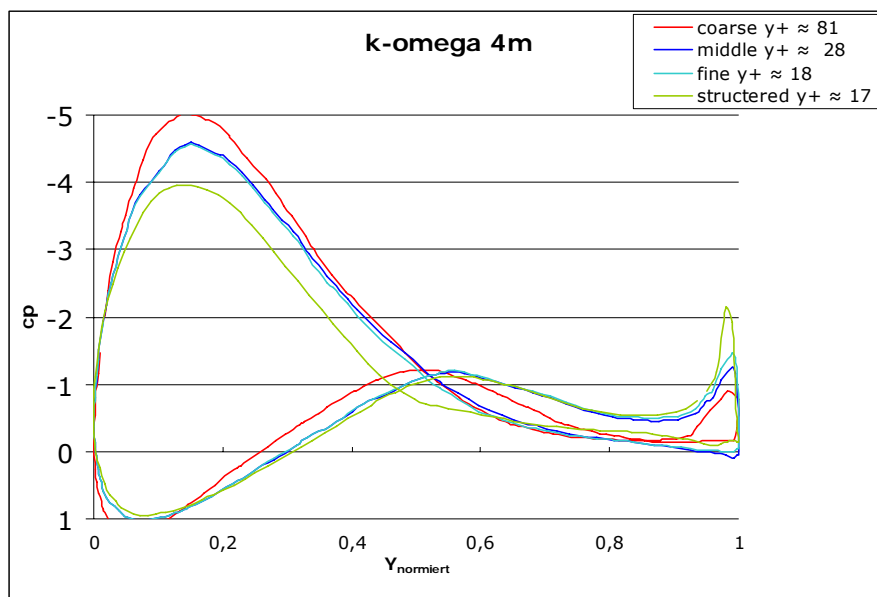


Diagram 9 Pressure coefficient c_p for different mesh types used in combination with the k/ω model

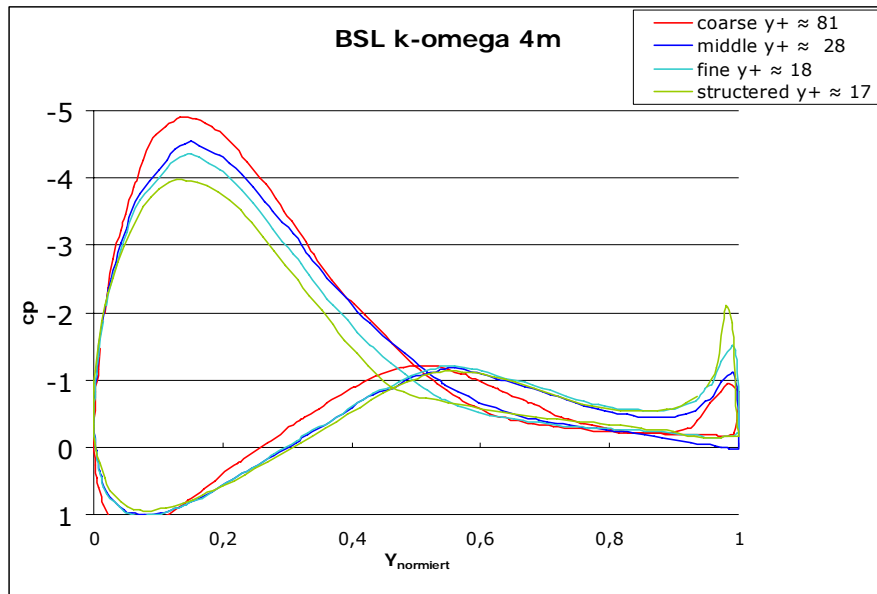


Diagram 10 Pressure coefficient c_p for different mesh types used in combination with the BSL k/ω model

The k/ϵ and the Spalart-Allmaras model predicted nearly the same pressure coefficients for the considered, unstructured mesh types, especially for the middle and fine mesh. Compared to the SST k/ω model, the trend is nearly the same for the longer part of the chord. However, the Spalart-Allmaras model showed the lowest suction peak in combination with the structured mesh. This fact could be explained with the large extension of the separation zone for this model. (cf.: Diagram 11 and Diagram 12)

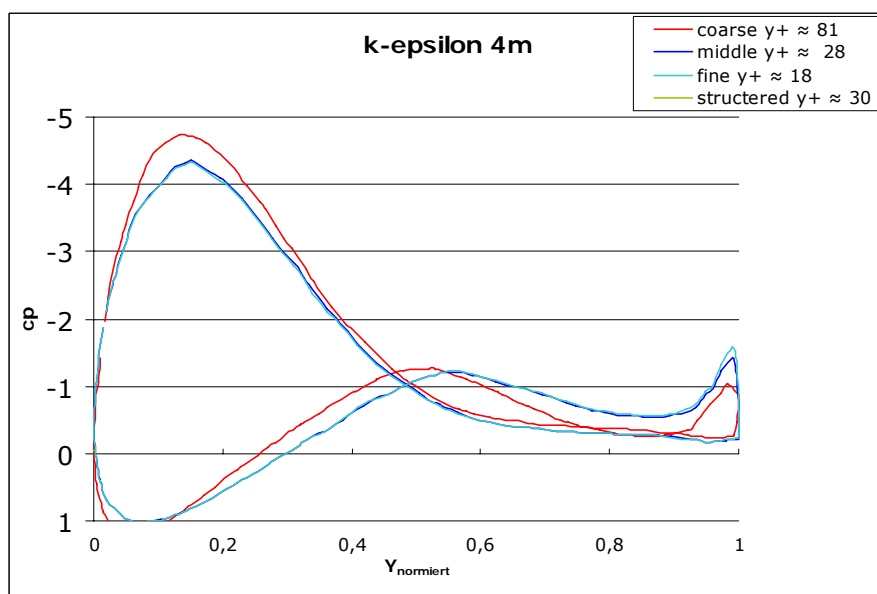


Diagram 11 Pressure coefficient c_p for different mesh types used in combination with the k/ϵ model

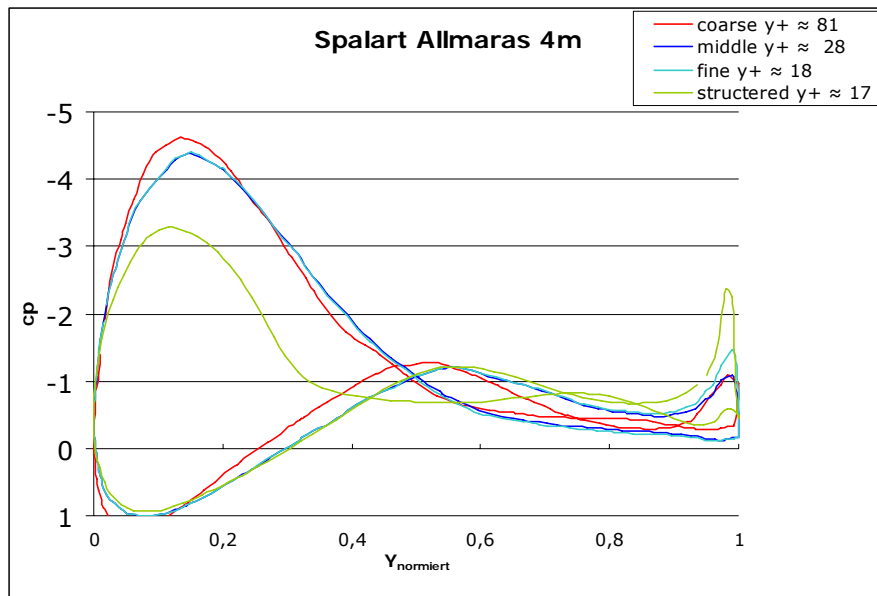


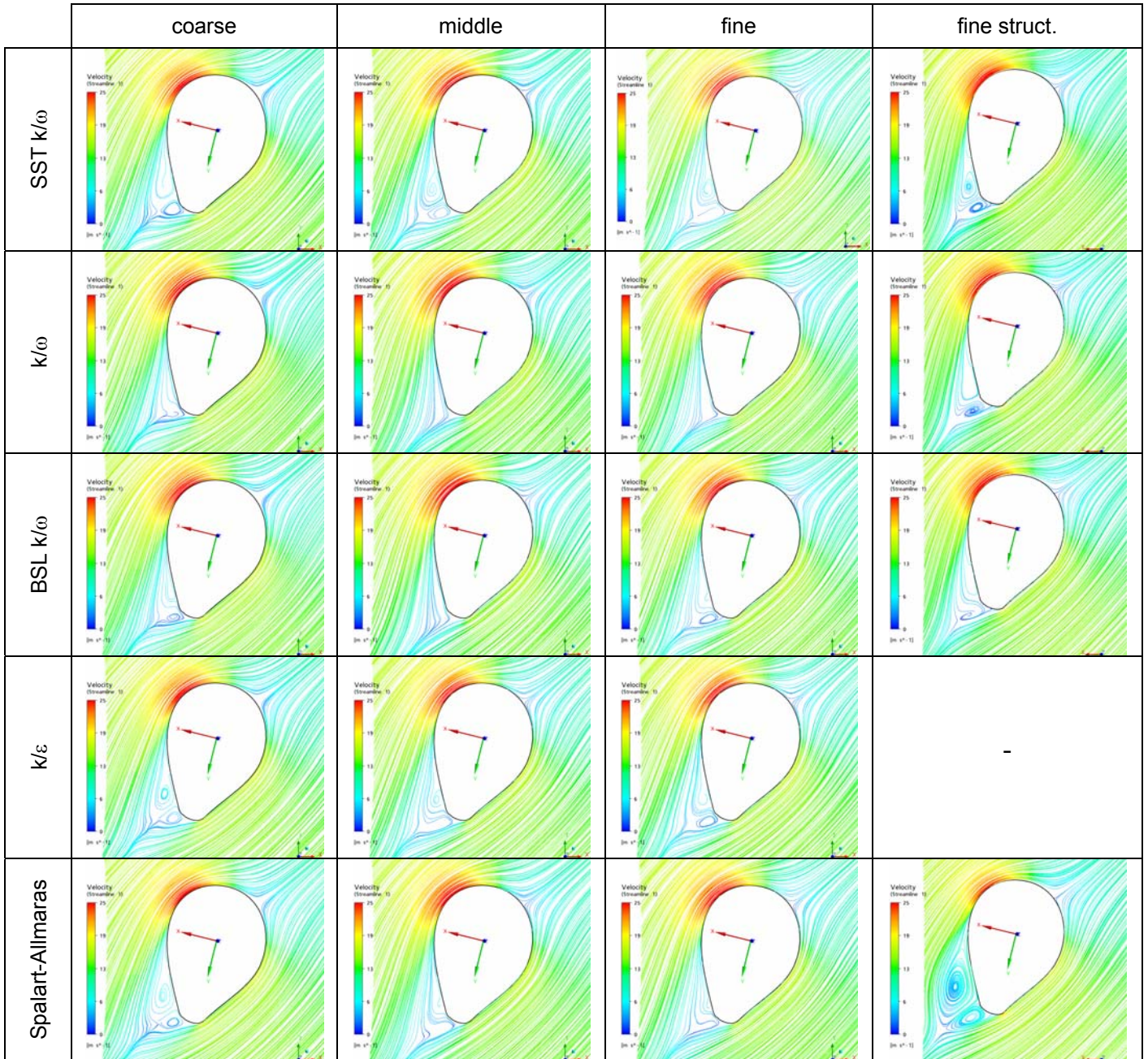
Diagram 12 Pressure coefficient c_p for different mesh types used in combination with the Spalart-Allmaras model

5.2.5 Streamline plots around the 4 m airfoil section

Observing the streamline plots coloured by the magnitude of the local velocity in Table 13 confirms the conclusion made on the basis of the surface streamline plots shown in chapter 5.2.3. Apparently the structured mesh resolves the separation best for all turbulence models considered. The magnitude of the velocity seems to be strongest for the k/ω model, which goes along with the continuous, highest predicted mechanical power. The 4 m distance from the root section has been chosen as at this point most of the differences are visible.

Results

Table 13 Streamline plots coloured by the magnitude of the local velocity for the 4 m distance from the root airfoil section











5.3 Detailed look on the results for the fine and the structured mesh

In this chapter, a more detailed insight into the results of the fine unstructured and the structured grids is given. These grids are considered as the most accurate types generated during the present work because they yielded the highest mechanical power. The calculated lift and drag coefficients as well as the pressure coefficient and wall shear stress graphs, streamlines around selected airfoil sections and tip vortex shading are discussed in this chapter. With the fine unstructured mesh also a simulation run in combination with a transition model has been carried out, however, this run yielded no advancement to the results. The reason is, that a y^+ of 18 is much too high and that the node spacing in chord wise direction is also too high to resolve the laminar/turbulent transition region.

The overviews in Table 14 and Table 15 show a direct comparison of the considered turbulence models in combination with the fine unstructured and the structured meshes.

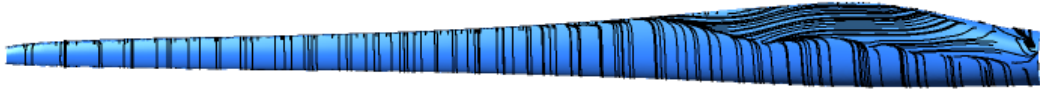



For the unstructured mesh it could be stated that the Reynolds Stress model predicted the highest amount of separation whereas the BSL k/ω , the k/ε and the Spalart-Allmaras model tended to predict similar the 3D effects. The k/ω model showed the fewest extensions of the separation zone which affect the lift coefficient at the inner section of the blade to be higher. When looking at the result of the Reynolds Stress model it can be seen that the separation zone extends at about two-thirds of the blade length. Another interesting conclusion is that the laminar simulation yielded no 3D effect but rather a separation all along the blade.

Table 14 Streamlines on the suction side in terms of the turbulence model used in combination with the fine unstructured mesh (boundary condition I, -0,9° pitch)

SST k/ω	
k/ω	
BSL k/ω	
k/ϵ	
Spalart-Allmaras	
SST k/ω transition	
Reynolds Stress	
laminar	

For the structured grid the SST k/ω model predicted the greatest amount of separation, whereas the k/ω and the BSL k/ω model predicted quite the same 3D effect, which does not correspond to the statement made for the unstructured mesh (cf.: Table 15). The Spalart-Allmaras models lies somewhere in between.

Table 15 Streamlines on the suction side in terms of the turbulence model used in combination with the structured mesh (boundary condition I, -0,9° pitch)

SST k/ω	
k/ω	
BSL k/ω	
Spallart Allmaras	

5.3.1 Lift and drag coefficients

The lift and drag coefficients have been calculated at four span wise airfoil sections using the method described in [26]. As mentioned above, the sections are at 4 m, 16 m, 30 m and 42 m distance from the root. Diagram 13 displays the lift coefficient c_L against the distance from the root of the blade in combination with the fine unstructured mesh. The deviation of the coefficients at the inner section of the blade is in a quite tall range. So, the k/ω model predicted the highest lift coefficient, 13,4% above the SST k/ω result at the 4 m section. This coincides with the observed surface streamline plot displayed in Table 14, where the k/ω model predicted the lowest 3D effect. Thus the flow is more attached and more lift is produced.

The great deviations at the inner airfoil section could generally be reduced to the different predictions of the 3D effect at the inboard section of the blade. At the middle sections (16 m and 30 m distance from the root) the lift coefficient deviates in a smaller range and at the 42 m section the deviations are within a range of 2%. The k/ω and the Spalart-Allmaras models are tending to predict higher coefficients, however, this is just a conclusion of the higher predicted mechanical power discussed above.

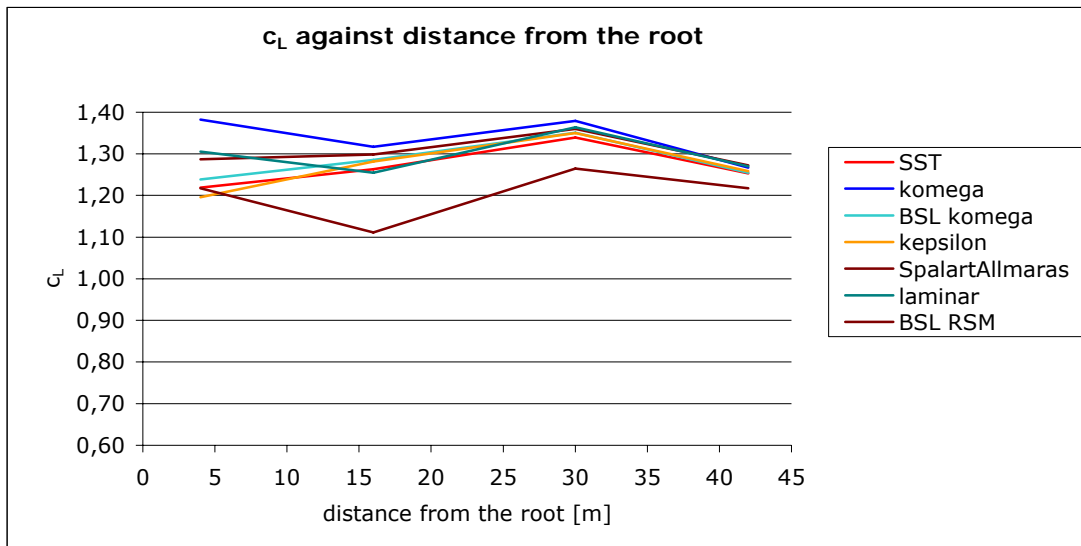


Diagram 13 Lift coefficient against the distance from the root in combination with the unstructured fine mesh (boundary condition I, -0,9° pitch)

Table 16 displays an overview of the deviations of the lift coefficients compared to the SST k/ω model.

Table 16 Deviations of the lift coefficient with regard to the unstructured fine mesh compared to the SST k/ω model (boundary condition I, -0,9° pitch)

	4 m	16 m	30 m	42 m
k/ω	13,4%	4,2%	3,0%	1,1%
BSL k/ω	1,6%	1,7%	0,8%	0,1%
k/ε	-1,9%	1,4%	0,8%	0,5%
Spalart-Allmaras	5,6%	2,8%	1,5%	1,5%
BSL RSM	-0,1%	-12,1%	-5,6%	-2,9 %
laminar	7,1%	-0,7%	1,8%	1,3%

Results

Combined with the structured mesh the gathered lift coefficients for the innermost sections (4 m and 16 m) are about 9% lower than calculated based on the unstructured mesh, except the Spalart-Allmaras model which shows a strong deviation at the 4 m section. This could be explained by the stronger separation which is yielded with the Spalart-Allmaras model at this part of the blade (cf.: Table 21). At the 30 m section the coefficient is about 3% lower and at the 42 m section the calculated coefficient is about 2% higher than with the unstructured mesh (cf.: Diagram 14).

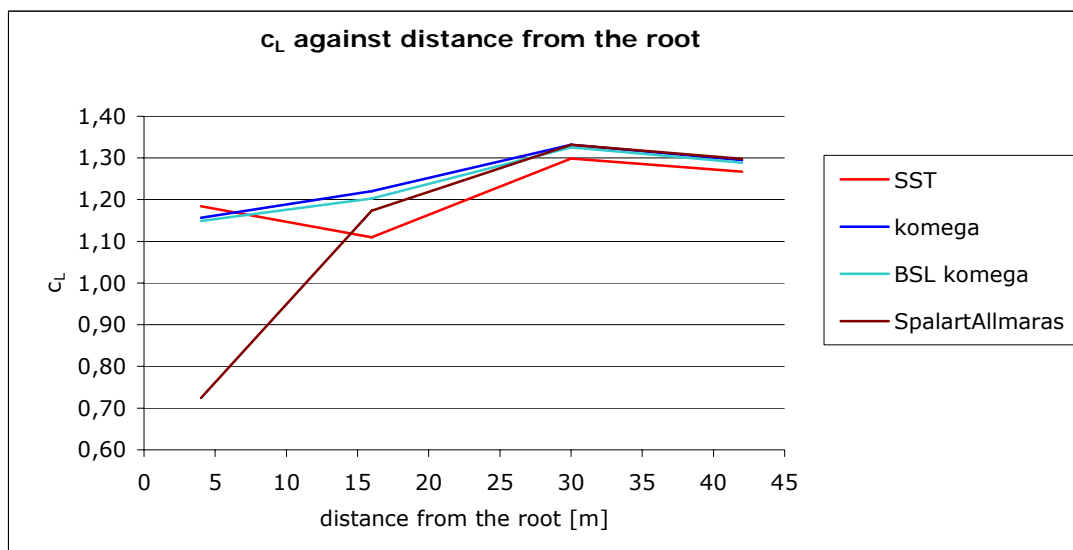


Diagram 14 Lift coefficient against the distance from the root in combination with the structured mesh (boundary condition I, $-0,9^\circ$ pitch)

The deviations among the models are different but in the same range as in combination with the unstructured mesh, see Table 17. However, the SST k/ω model predicted the highest lift at the 4 m section, while the SST k/ω model in combination with the unstructured mesh predicted the lowest lift.

Table 17 Deviations of the lift coefficient with regard to the structured mesh compared to the SST k/ω model (boundary condition I, $-0,9^\circ$ pitch)

	4 m	16 m	30 m	42 m
k/ω	-2,3%	9,9%	2,5%	2,2%
BSL k/ω	-3%	8,3%	2,1%	1,7%
Spalart-Allmaras	-38,8%	5,7%	2,6%	2,4%

Results

Comparison of the calculated drag coefficients depicted in Diagram 15 and Diagram 16 shows that with the structured mesh the predicted drag at the three outer sections is about 50% lower than with the unstructured mesh. Only the Spalart-Allmaras model showed a higher drag coefficient at the inner section, but this goes along with the strong separation predicted for the structured mesh.

The lower drag is a potential reason for the higher mechanical power output with the structured mesh. A proper influence factor for the higher drag coefficient in combination with the unstructured mesh could be the less smooth resolved surface of the blade with the prism elements. In order to the surface of the blade also being resolved more smoothly, the element size on the surface had to be considerably smaller. This, however, would result in a very high number of elements. Since the number of elements of the unstructured mesh is at a range of 9 million, the performance of the computer used for generating the mesh was already occupied to full capacity.

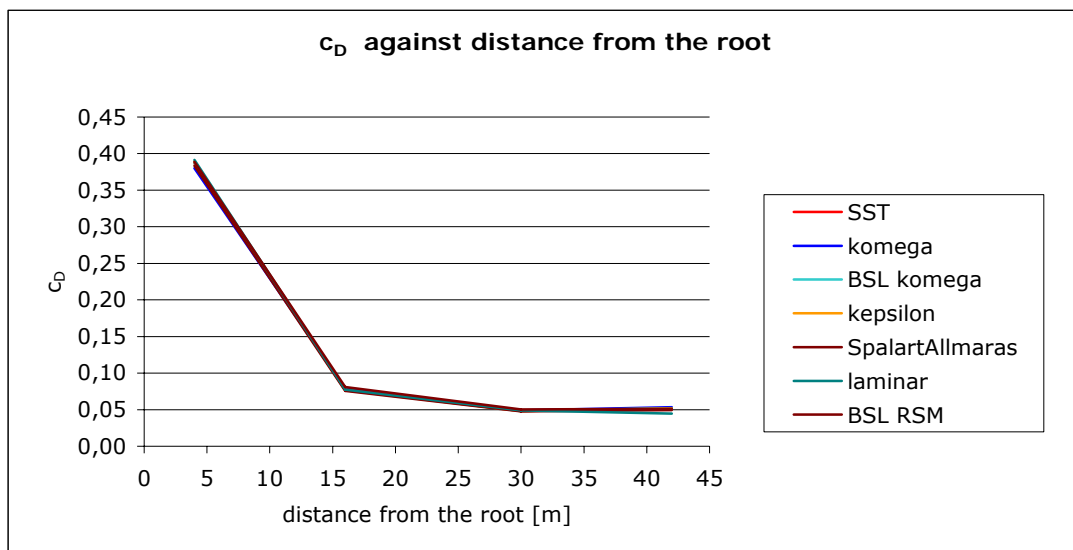


Diagram 15 Drag coefficient against the distance from the root in combination with the unstructured fine mesh (boundary condition I, $-0,9^\circ$ pitch)

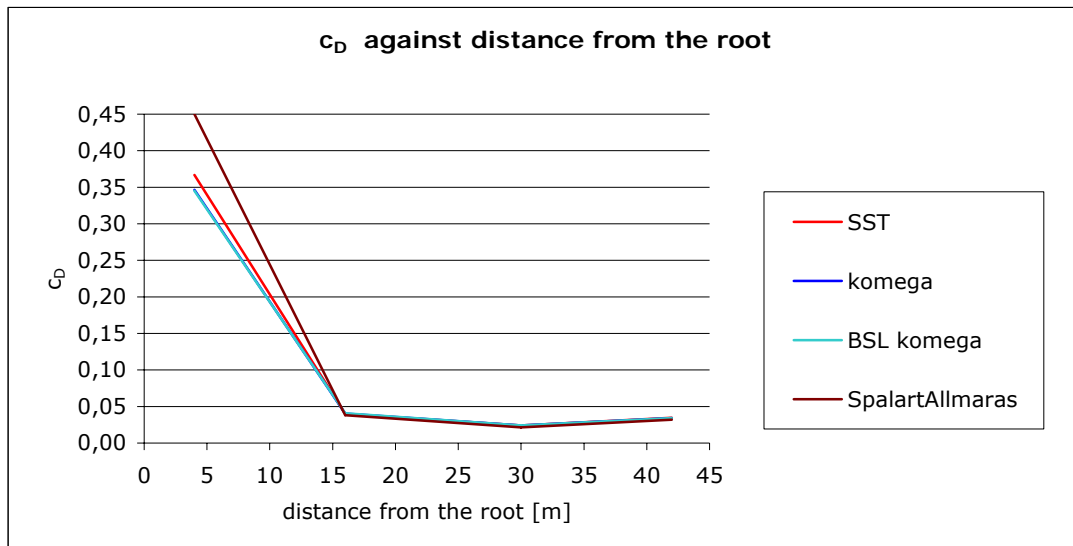
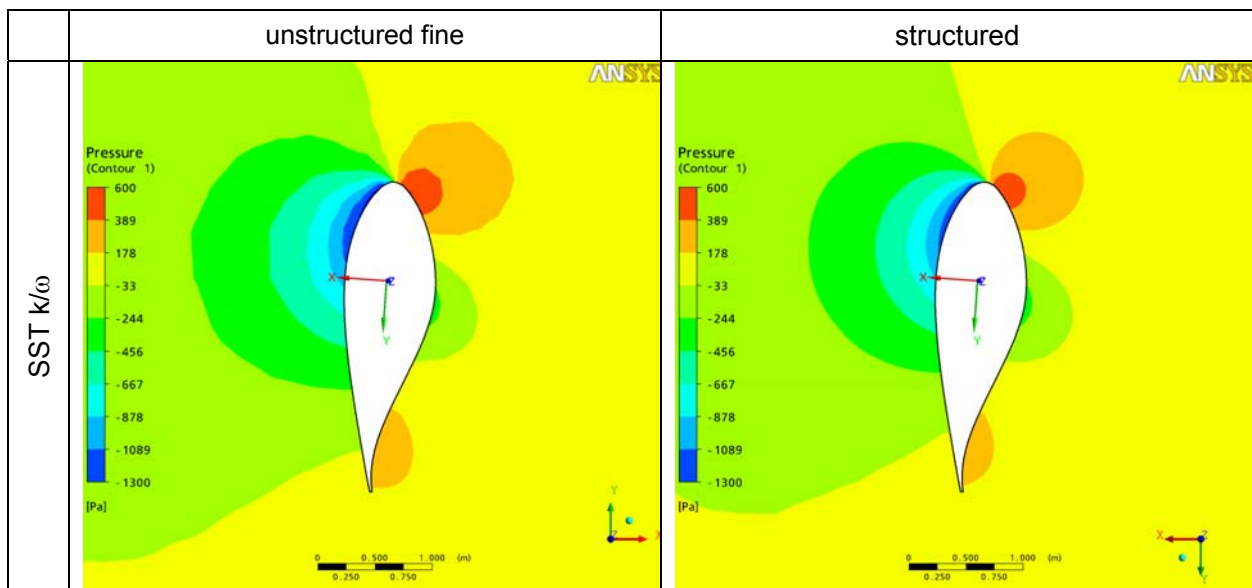


Diagram 16 Drag coefficient against distance from the root in combination with the structured mesh (boundary condition I, $-0,9^\circ$ pitch)

5.3.2 Pressure distribution around 16 m blade section

At this point, the 16 m distance from the root section is the airfoil section of choice to compare the unstructured and structured mesh regarding pressure distribution. Table 18 shows that the structured mesh yielded a smaller high pressure zone in the region of the stagnation point. Therefore, the lower drag of the structured mesh could be interpreted as the blade does not have to fight against a high pressure zone. When looking at the run of the pressure coefficient in Diagram 17, it is clear that the structured mesh yielded a higher and sharper suction peak than the unstructured mesh, while the remaining run of the structured mesh showed a lower c_p than the unstructured mesh.

Table 18 Comparison of the pressure distribution around the 16 m airfoil section for unstructured and structured mesh (SST k/ω model, boundary condition I, $-0,9^\circ$ pitch)



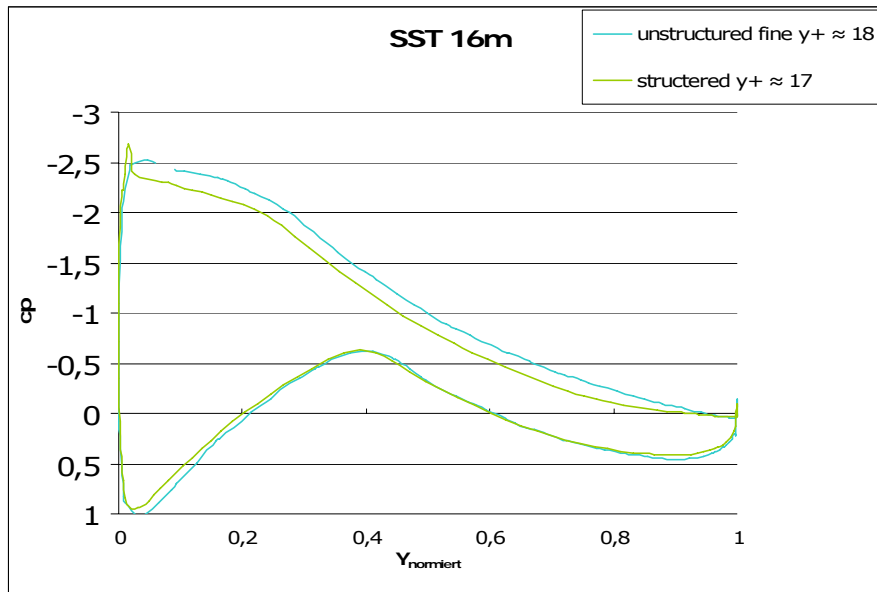
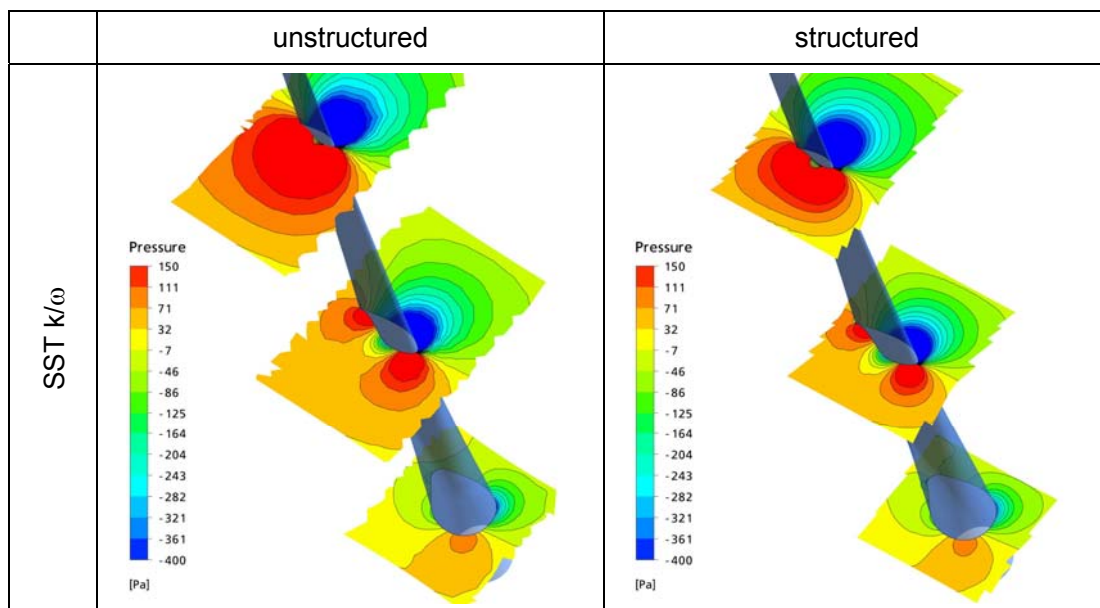


Diagram 17 Comparison of pressure coefficient at the 16 m airfoil section for unstructured and structured mesh (SST k/ω model, boundary condition I, $-0,9^\circ$ pitch)

Table 19 shows that the zone of the high pressure at the pressure side of the blade is more widely spread for the unstructured mesh than for the structured one. Also, as seen in Table 18, for the detailed view of the 16 m section.

Table 19 Comparison of the pressure distribution for unstructured and structured meshes at the three lower airfoil sections (SST k/ω model, boundary condition I, $-0,9^\circ$ pitch)



5.3.3 Wall shear stress at the 4 m airfoil section

Comparison of the wall shear stress for the two different mesh types in Diagram 18 and Diagram 19 shows that all considered turbulence models predicted the separation point more consistently in combination with a structured grid. The separation point can be recognised at about $Y_{norm} = 0,5$ of the normalized chord where the wall shear stress vanishes. Only the Spalart-Allmaras model showed an earlier separation point for the structured mesh. The unstructured mesh predicted the suction peak (the highest wall shear stress occurs at the suction peak since there the flow speed around the blade is highest) at a lower Y_{norm} position which can also be related to the higher drag coefficients as the zone with the highest velocity is located nearer to the tip (at lower Y_{norm} position). Diagram 18 also clearly shows that the SST k/ω model in combination with the transition model did not capture the laminar/transient transition. In case the transition would be captured, there would be a step change in the run of the wall shear stress along the suction side, as shown in [19].

On the suction side for both, the unstructured and the structured mesh, the k/ω model predicted the highest wall shear stress and the SST k/ω model the lowest within a small range. The Spalart-Allmaras model for the structured mesh showed the greatest amount of deviation compared to the other models, however, if you look at Table 21, this effect clearly bases on the well developed eddies within the separation zone.

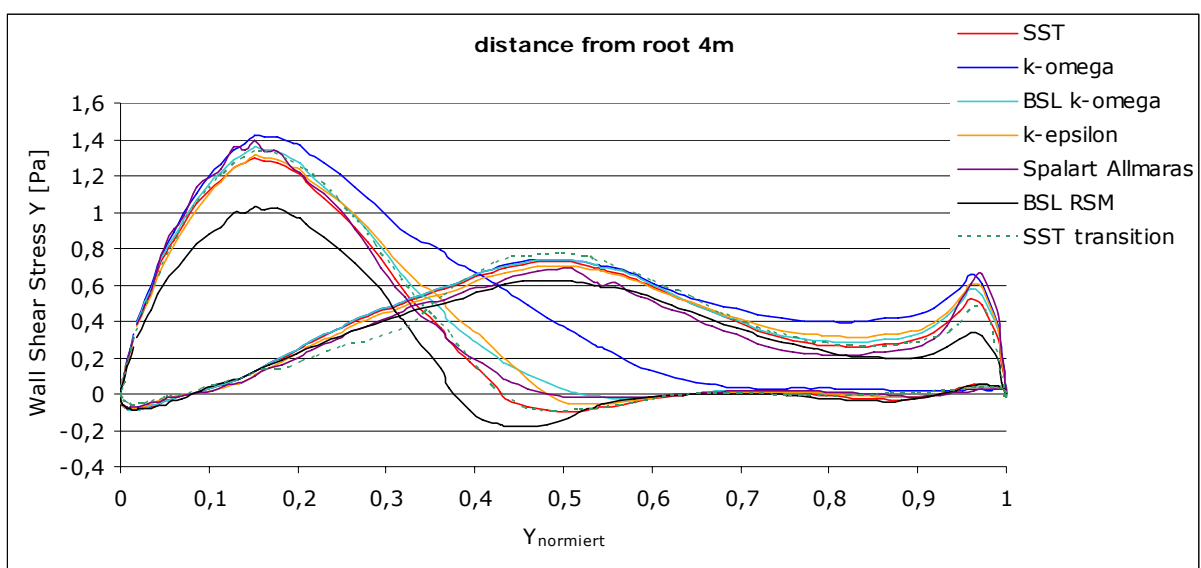


Diagram 18 Wall shear stress against the normalized chord in combination with the unstructured fine mesh (boundary condition I, $-0,9^\circ$ pitch)

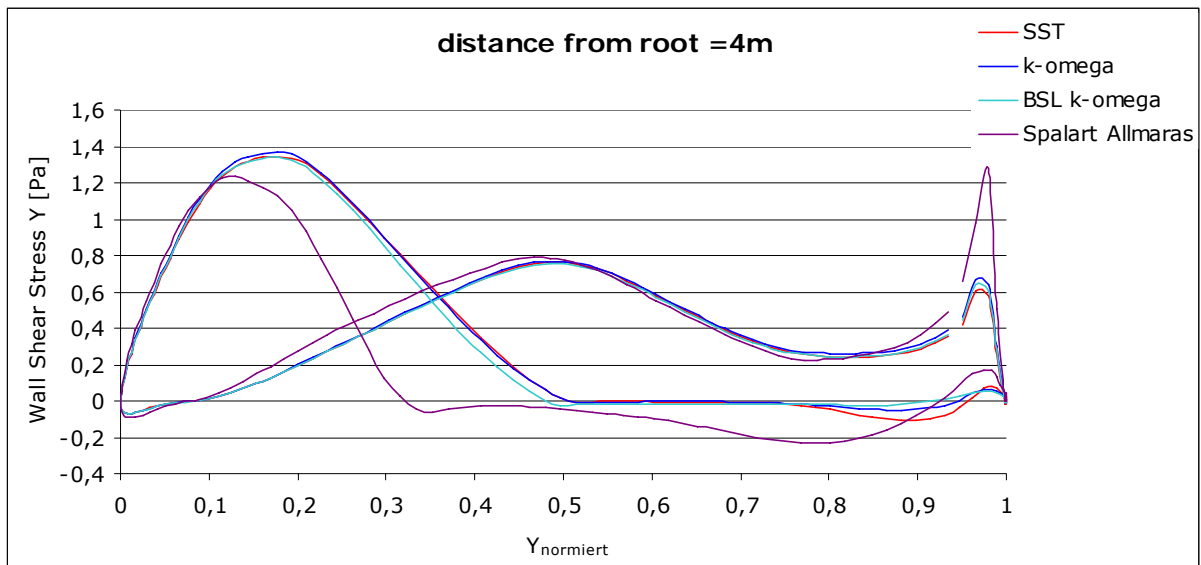


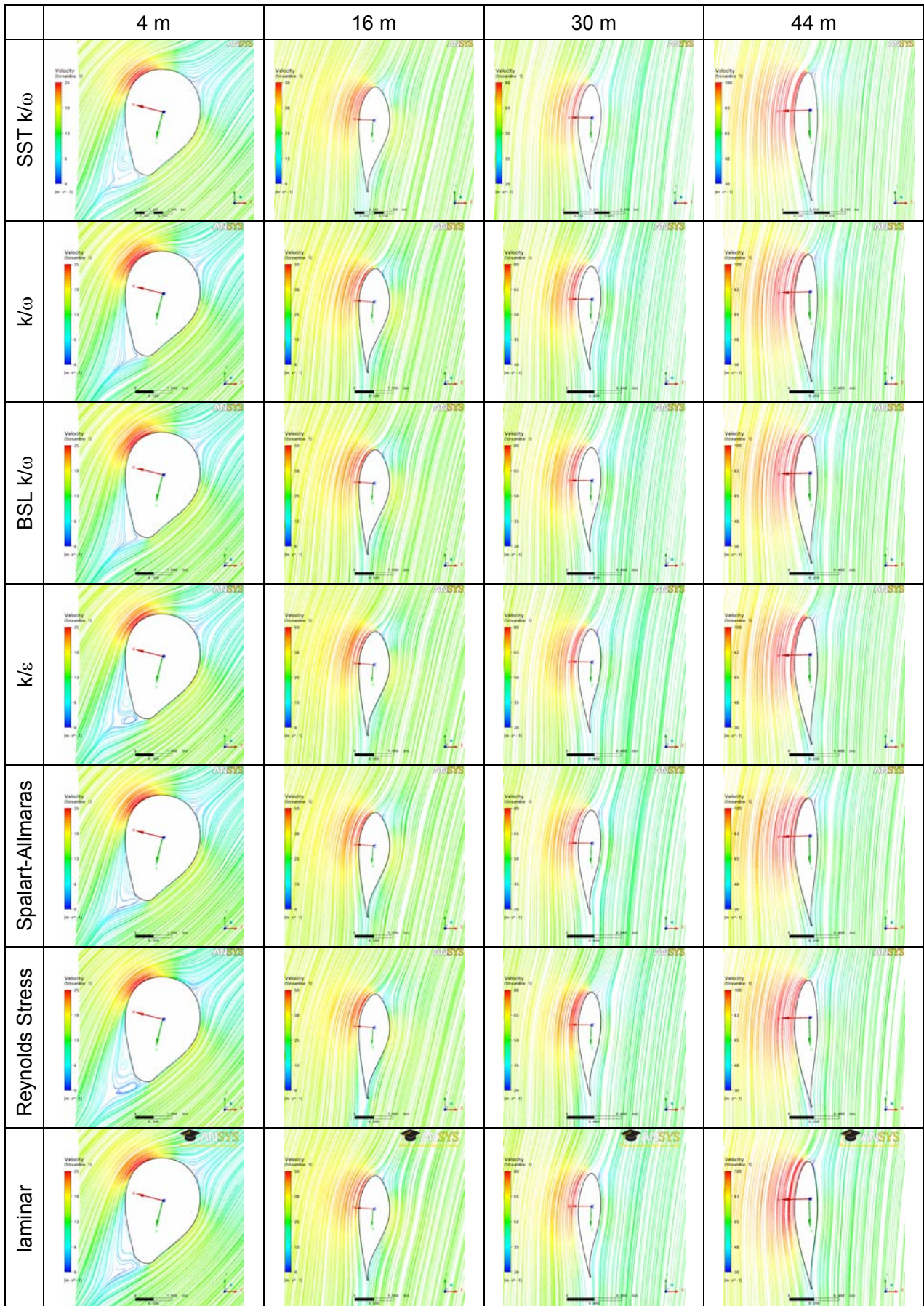
Diagram 19 Wall shear stress against the normalized chord in combination with the structured fine mesh (boundary condition I, $-0,9^\circ$ pitch)

5.3.4 Streamlines around all selected airfoil sections and tip vortex comparison

Examination of the streamlines around the four selected airfoil sections shows that there are no serious differences among the different turbulence models in general. The separation which appears at the 4 m section shows some differences which comes along with the formation of the 3D effect depicted in the surface streamline plots above. At the higher sections just some little deviations in the magnitude of the local velocity, which is represented by the streamlines colour, are recognisable. For the Reynolds Stress model a separation at the 16 m blade section is recognisable, while for the other models the flow is already attached at this blade length (c.f.: Table 20).

Results

Table 20 Streamline overview of all examined airfoil sections for the unstructured fine mesh, coloured by the magnitude of the local velocity (boundary condition I, $-0,9^\circ$ pitch)

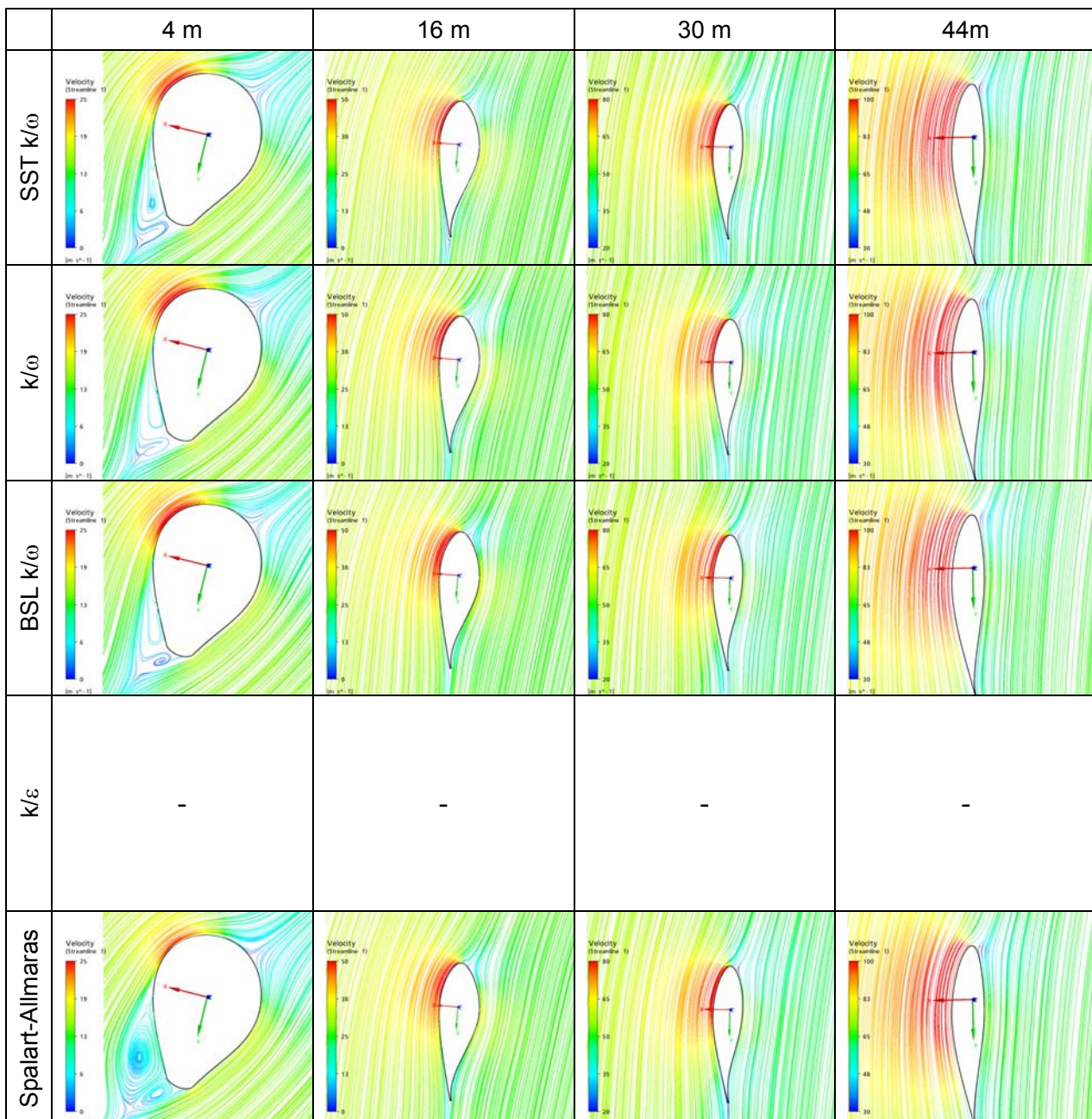


Results

The structured mesh showed a better resolution of the separation zone at the 4 m section, whereas the SST k/ω model and the BSL k/ω model predicted nearly the same and the Spalart-Allmaras model showed the strongest separation. For the unstructured mesh these statements could not be made. One reason is that with the unstructured mesh the elements grow very fast when moving away from the blade and, thus so the fine resolution could not be reached.

At the higher sections, there are also just little deviations in the magnitude of the velocity detectable (cf.: Table 21).

Table 21 Streamline overview of all examined airfoil sections for the structured mesh, coloured by the magnitude of the local velocity (boundary condition I, $-0,9^\circ$ pitch)

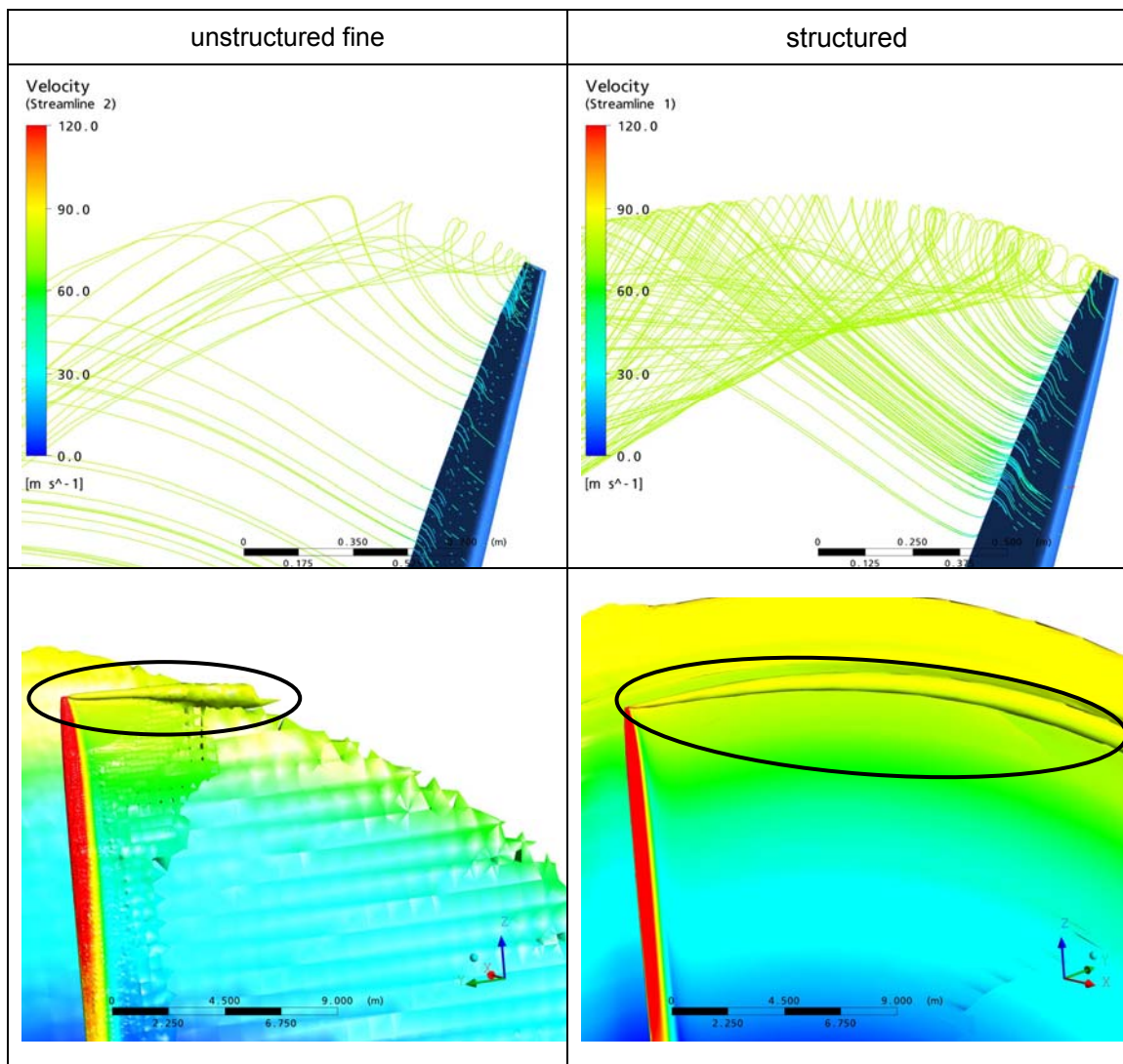


Results

The formation of the tip vortex is displayed in Table 22. There are no significant differences among the turbulence models recognisable, however, the structured mesh resolves the tip vortex much finer than the unstructured mesh. This could be explained by the finer resolution of the structured mesh away from the blade surface.

In Table 22, the first line displays streamlines of the tip vortex and the second line shows iso-surfaces of the total pressure coloured by the magnitude of the flow velocity. The iso-surface plot shows a longer vortex for the structured mesh.

Table 22 Comparison of the tip vortex formation for the unstructured fine mesh and the structured mesh (boundary condition I, $-0,9^\circ$ pitch)



5.4 Transient (time dependent) simulation

For more detailed investigations a time dependent calculation run has been performed for boundary condition I at 0,8° pitch. The resolution of the time steps was a two degrees azimuth angle and two revolutions have been calculated.

The major difference with regard to the steady state calculations was the higher mechanical power predicted. Diagram 20 shows the development of the mechanical power for the transient simulation. After a short overshoot within the first 100° azimuth angle the power began to engage to an average mechanical power of about 1950 kW (green line in diagram) which is 11% higher than the steady-state calculations. The simulation was conducted with the SST-SAS turbulence model.

Table 23 Settings for transient simulation

Total time	7,64 s
Time step (resolution)	0,02123 s
Internal iterations	25

It has to be said that transient simulation is very time consuming, so this run took 51 days to complete when set up for a serial run on a 8GB RAM, 3GHz Quad Core computer.

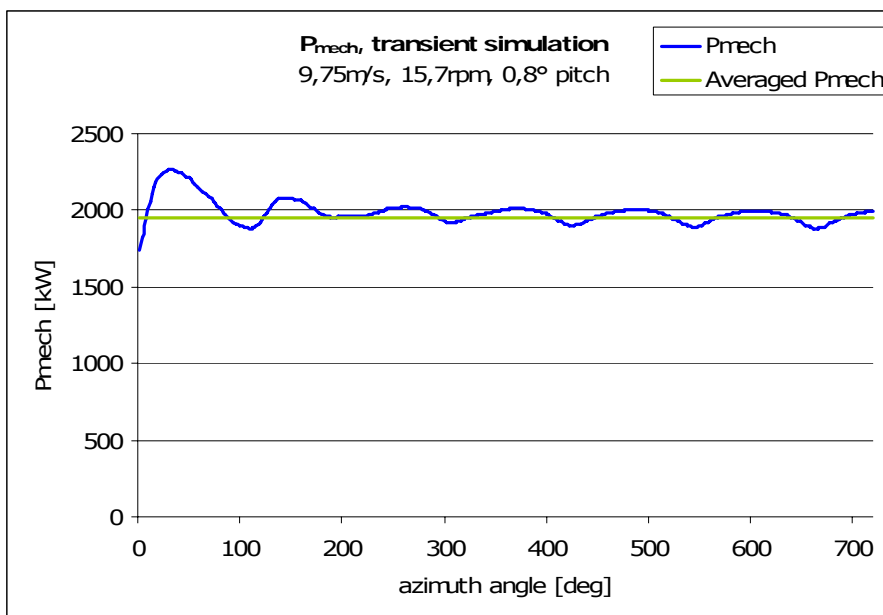


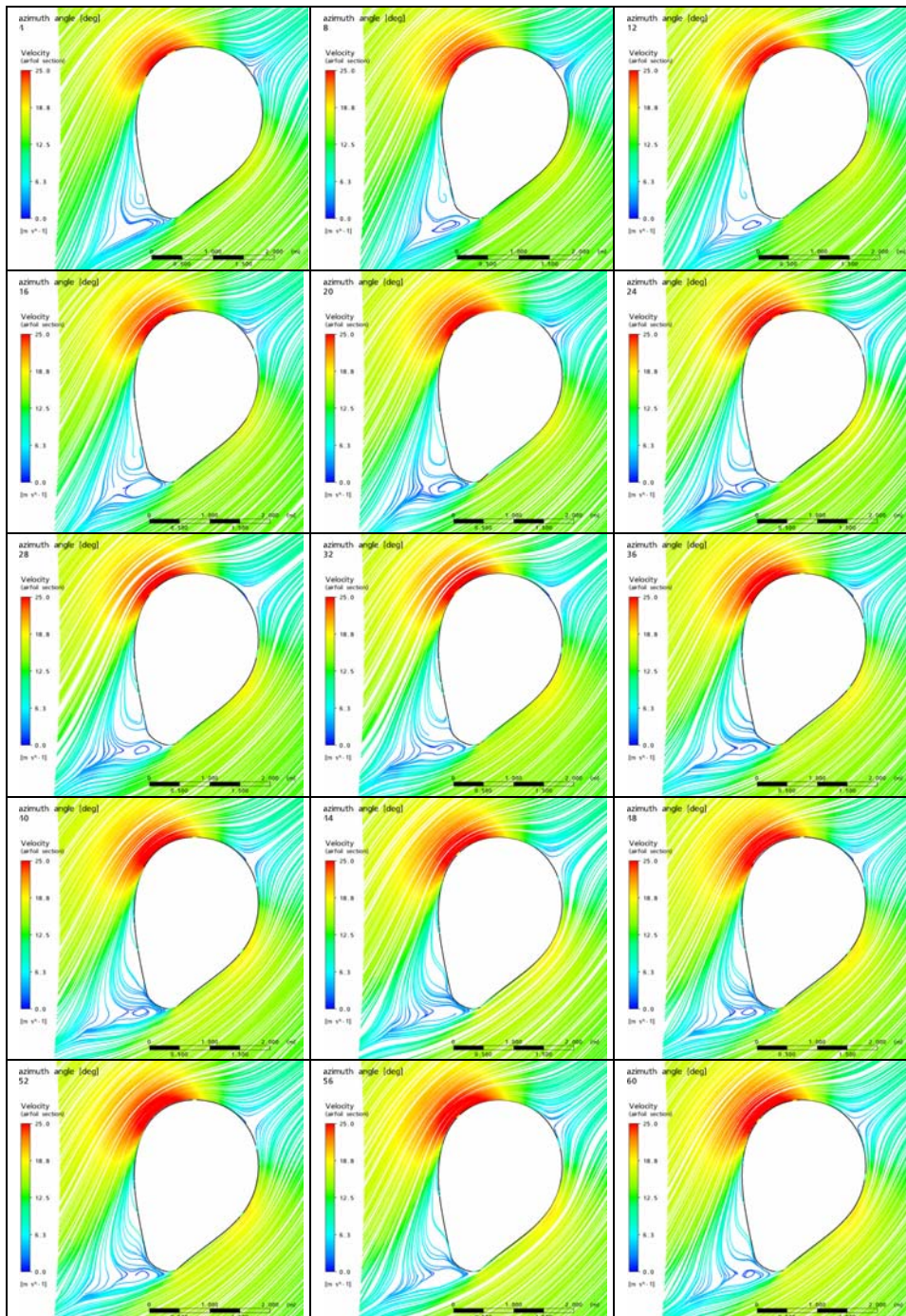
Diagram 20 Mechanical power against the azimuth angle for the transient simulation

Results

In Table 24 the development of an eddy at the inboard section of the blade is depicted. Such effects could only be resolved with a time dependent simulation.

This periodic eddy formation could also be one of the causes for the alternating mechanical power output. A video which gives you a better insight into the formation of the eddy within the separation zone at the inboard blade section is enclosed on a CD to be found at the end of this paper.

Table 24 **Development of an eddy at the 4 m distance from the root airfoil section, resolved in 4° azimuth angle steps**



5.5 Summary of the deviations for the computed mechanical output

This chapter displays the results of the reference runs without any wind profile and the correct blade length, in order to contrast them with the results of the BEM calculations realized by AMSC Windtec GmbH with the commercial BEM software GH Bladed.

These calculations showed that at all pitch angles observed the runs by means of the axial symmetric wind profile and the shorter blade yielded a 11% higher mechanical power output than with a constant wind condition and the correct blade length. So, the reference runs all were performed with a constant wind condition of 9,75 m/s and a rotational speed of 15,7 rpm (boundary condition I).

Diagram 21 gives an overview of the different steady-state simulation runs whereas the green line represents the BEM results, the red line the results from the unstructured mesh reference run and the blue dot the result from the structured mesh reference run. One essential fact is, that the calculations with Ansys CFX show the same tendency for the run of the power curve compared to the BEM calculation. A deviation just can be detected in the magnitude of the power. The most likely reason of the deviations, mainly for the unstructured grid, could be probably stated to be the grid resolution which was restricted by computational resources (3,4GB RAM at the workstation used for the grid generation). It can also clearly be seen that in combination with the structured mesh the deviation to the BEM calculation is reduced to a minimum. In the scope of the present work the trend that the power raises with the resolution of the grid was proved, as well as in [1], where the same tendency was recognised for the structured mesh.

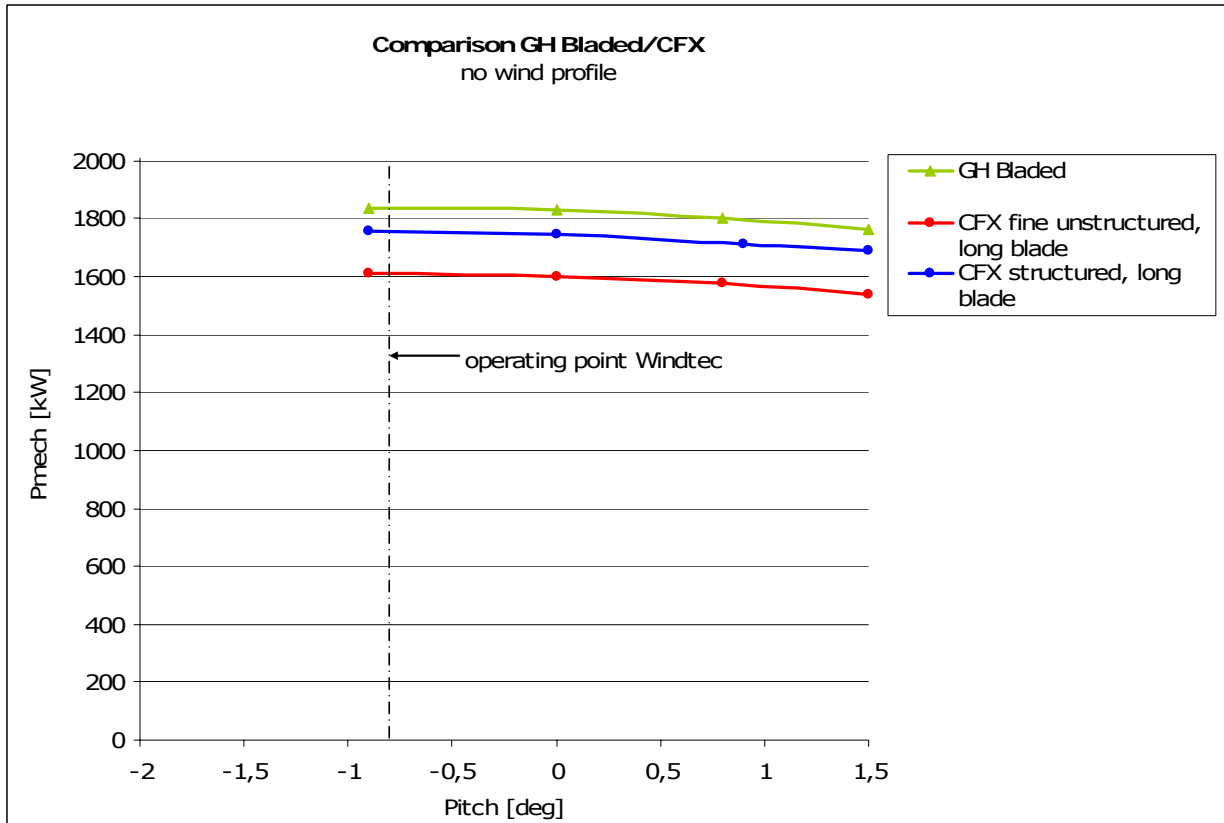


Diagram 21 Overview of the deviations with regard to the GH Bladed (BEM) calculation

Table 25 gives an overview of the deviations observed with regard to the BEM calculation.

Table 25 Deviations related to the GH Bladed (BEM) calculation without wind profile

Calculation type	Deviation
CFX unstructured fine	-14%
CFX structured	-4,5%

The transient calculation run has also been converted to the constant wind condition. This was done by the knowledge that the simulations with the short blade and the axial symmetric wind profile yielded a result 11% higher than the simulations with the correct blade length and no wind profile. The result is displayed in Diagram 22. The mechanical power engaged is reduced to 1.750 kW. Compared to the BEM simulation for this operating point it displays a deviation of -3%, which is much lower than for the steady-state simulation. This clearly shows that transient simulation is much more realistic than steady-state computation, even though the used grid is too coarse to predict the correct mechanical power with a steady-state simulation.

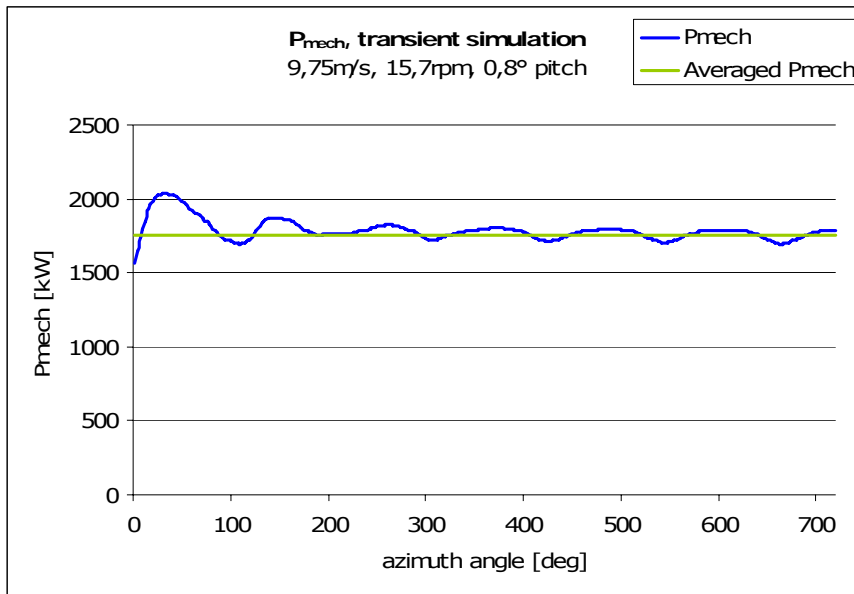


Diagram 22 Mechanical power against the azimuth angle for the converted transient simulation

5.5.1 Conversion to the exponential wind profile

Calculating the rotor power with the use of the exponential wind profile was accomplished by calculating a reduction factor for the mechanical power of one blade at each azimuth angle within the wind profile. The reduction factor calculated for the mechanical power output plotted against the azimuth angle for one revolution is displayed in Diagram 23.

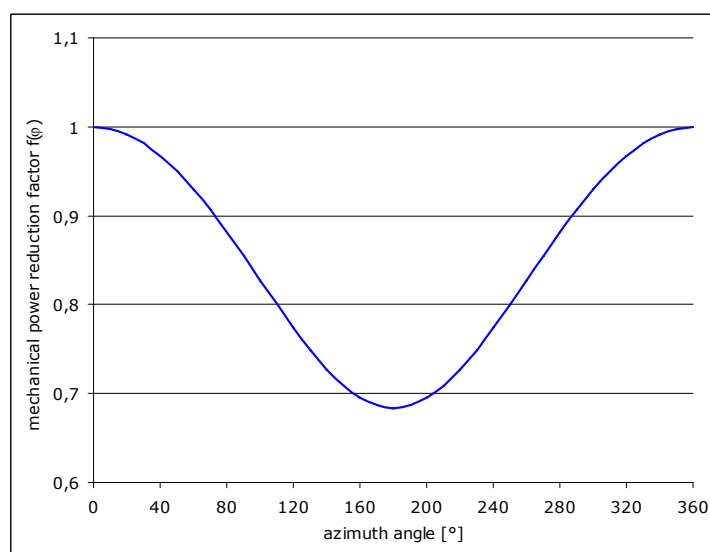


Diagram 23 Mechanical power reduction factor against azimuth angle

Results

The blade pointing in the positive z direction (zero degree position) was set as reference (factor 1) since all former runs were performed in this position. The following expression represents the calculation of the mechanical power. P_{zero} is the mechanical power at the zero degree position, f_{red} the reduction factor and n the number of blades.

$$P_{mech} = \frac{\sum_{\varphi=0^{\circ}} P_{zero} f_{red}(\varphi)}{360^{\circ}} n \quad (18)$$

The wind profile was given by the following exponential function, which is plotted in Diagram 24 where the position of the rotor plane is marked by the black line. z is the z coordinate, z_{hub} is the height of the hub, v_{rated} is the rated wind speed at the hub position and a is the wind shear exponent. The chosen variables are related to boundary condition I. Table 26 gives an overview of the variables for the wind profile function.

$$V(z) = V_{rated} \left(\frac{z - z_{hub}}{z_{hub}} \right)^a \quad (19)$$

Table 26 Overview of the variables for the wind profile

Z_{hub}	80m
V_{rated}	9,75m/s
a	0,2

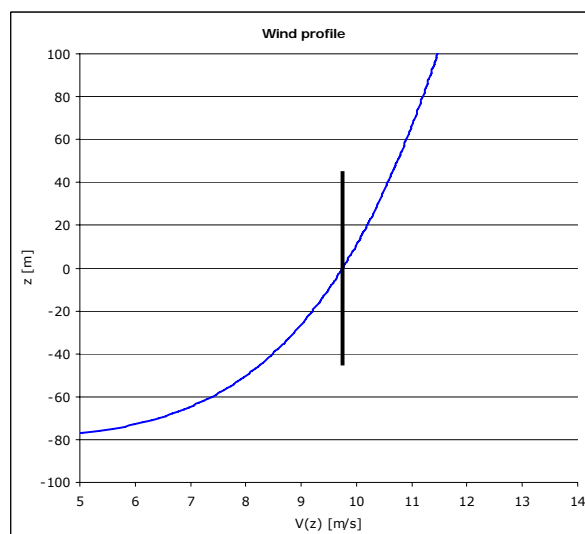


Diagram 24 Wind speed against z direction

Results

The mechanical power could be calculated with the knowledge of the reduction factor for the whole rotor within the wind profile. This was done by multiplying the zero degree mechanical power by the reduction factor of each azimuth angle for one revolution and afterwards averaging the power for one revolution. The method applied to the runs performed in combination with the fine unstructured and the structured mesh is displayed in Diagram 25. The runs with GH Bladed are also included. The diagram shows that the application of the wind profile yields a lower mechanical power, since the wind speed reduction below the axis of rotation is greater than the wind speed rise above the axis of rotation within the wind profile (cf.: Diagram 24). The deviation for the structured mesh, whether a wind profile is applied or not, is smaller than shown for the unstructured mesh and the BEM result. The overall deviation among the GH Bladed results and the results from the unstructured mesh as well as the structured mesh are the same as displayed in Table 25.

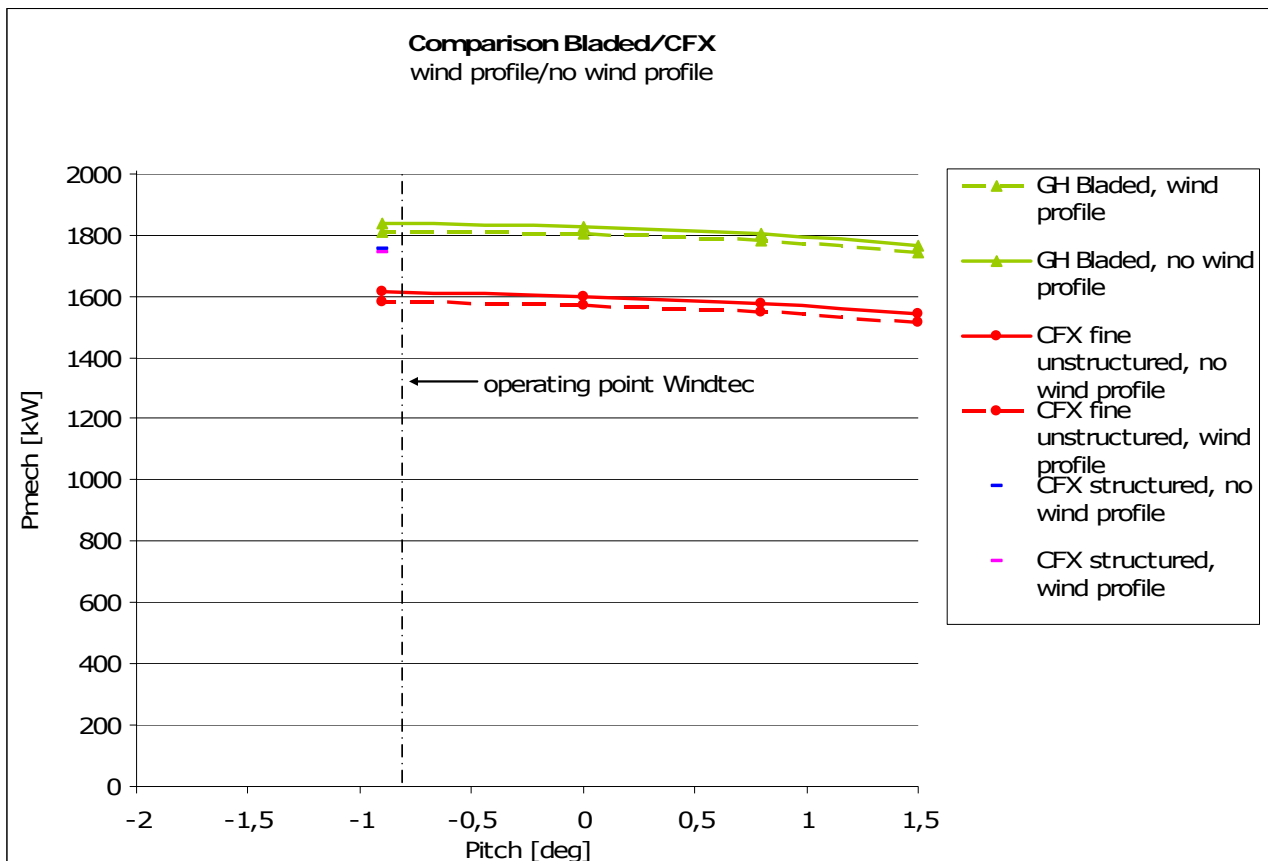


Diagram 25 Comparison of the results with and without wind profile

Results

At the end of this chapter an overview of the calculated power coefficient of the simulations with the correct wind profile and the correct blade length as well as the GH Bladed result is given. Note that the maximum reachable power coefficient investigated by Betz is 59,3% (cf.: chapter 2.1). In [6] it is shown that current up-to-date wind turbines of the same range as the turbine investigated in the present work reach a maximum power coefficient of around 50%. If looking at the results of the present work in Diagram 26, it is visible that the results of the CFD analysis as well as of the BEM calculation are within a realistic range of 39% to 44%.

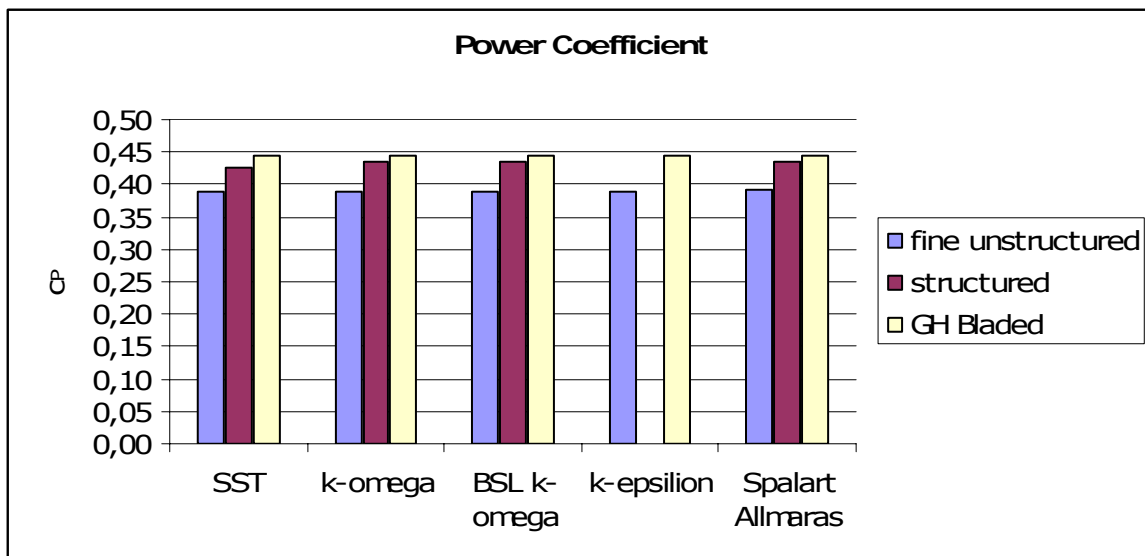


Diagram 26 Comparison of the power coefficient (boundary condition I, $-0,9^\circ$ pitch)

6 Conclusion and prospect

In general, it was shown that all evaluated turbulence models predicted nearly the same mechanical power output for all considered pitch angles when used for a certain grid. The comparison of the results to the BEM calculations realized by AMSC Windtec GmbH provides the same qualitative tendency as the results yielded in the scope of this work. It has been proved that the unstructured grid still contains a too small number of elements whereas, in combination with a structured grid good quantitative agreement with the BEM results is obtained.

With the finest unstructured grid the highest mechanical power output was yielded and the maximum deviation among the turbulence models was at max. 1,7%, except the Reynolds Stress model which yielded a deviation of -5,4%. This quite large deviation could be related to the wider spread separation zone predicted by the Reynolds Stress model. The result gained with the laminar simulation can be regarded as noncompetitive.

The strongest dependency of the grid resolution relating to the unstructured mesh was displayed for the Spalart-Allmaras model (cf.: Diagram 5). This fact signifies a high dependency of the near wall resolution for the Spalart-Allmaras model. The SST k/ω and the k/ε model showed the same tendency less clearly. Therefore, further simulations with finer grids have to be conducted in the future.

Even though the SST k/ω model predicted nearly the lowest mechanical power, the result should not be labelled to be unrealistic since the 3D effect predicted by the SST k/ω model was within a practical range compared to [19] where a similar wind turbine was simulated. The structured mesh as well calculated the amount of the 3D effect in a comparable range, however, for all turbulence models combined with it. This reflects the strength of the SST k/ω model as already stated in many references [18, 19, 29, 30]. All other turbulence models considered predicted a smaller 3D effect.

Carrying out simulations in combination with the structured mesh yielded a mechanical power approximately 9% higher than in combination with the finest unstructured mesh. This strong rise of the power output can be related to the significantly finer resolved surface of the blade in chord wise direction. The unstructured mesh resolved the blade surface more edged and rough, as it was not possible to achieve a smaller element size on the surface of the blade. The blade surface did not seem to be smooth. [44] also

suggests that a too rough resolved blade surface yields higher drag and thus a lower power output.

This also coincides with the calculated drag coefficients, since the unstructured mesh yielded a drag coefficient of approximately 45% higher than the structured mesh. Further calculations done by [1] with a structured mesh also proved that refining in chord wise direction yields lower drag and thus a higher power output.

The above-mentioned further simulations with a finer unstructured grid should be accomplished with highly refined grid elements on the blade surface in order to avoid the high drag produced by a rough surface.

In Diagram 27 the mechanical power for the simulations with the fine unstructured mesh, the structured mesh and the BEM results are finally contrasted to display the above mentioned facts.

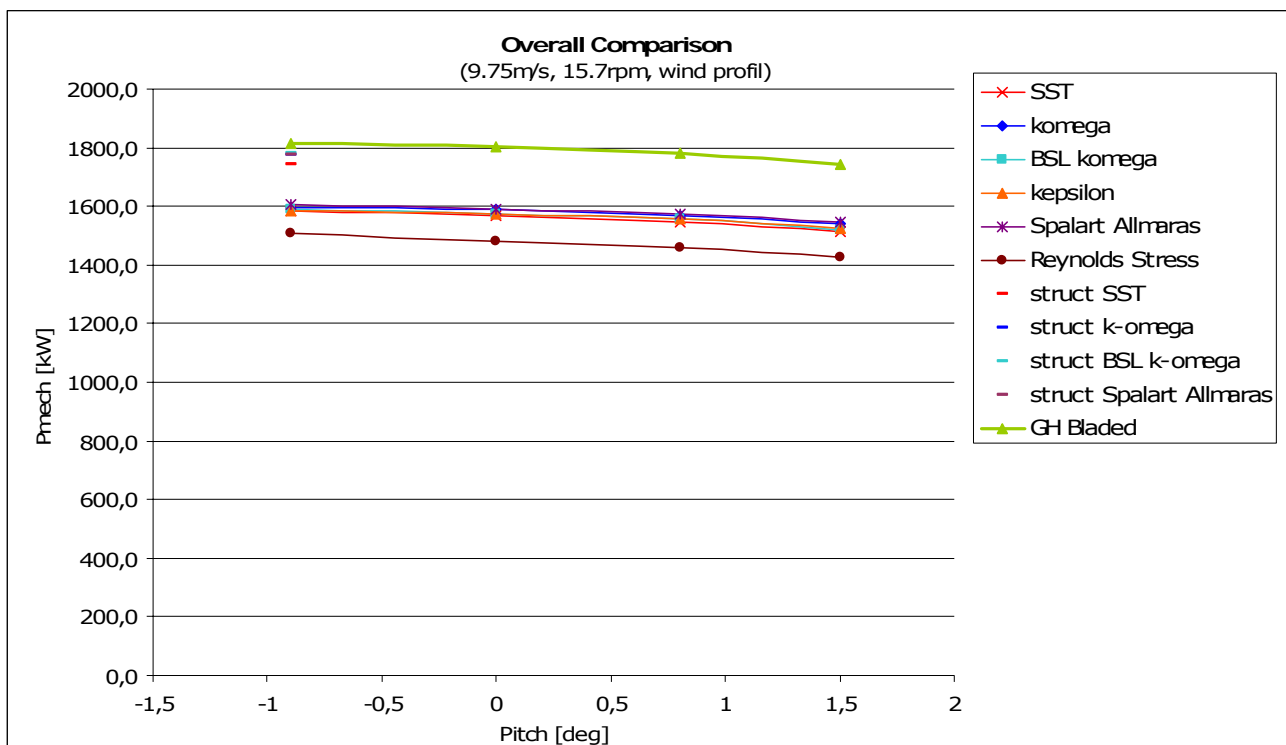


Diagram 27 Final comparisons of the conducted simulations against the BEM results (boundary condition I, with wind profile)

The transient simulation in combination with the unstructured mesh showed an increase of the mechanical power of 11%. This could be related to the fact that transient simulation accounts for effects which occur during the rotation of the rotor whereas steady-state simulation just calculates the power for the rotor in a fixed circumferential position which could be interpreted as a snapshot of the flow during the rotation of the rotor. Therefore,

the result of the transient simulation represents the reality much more than a steady-state simulation. In the scope of this work a periodic formation and destruction of eddies inside the separation zone of the blade was observed (cf.: Table 24). In fact, transient simulation yields more accurate results, however, it is much more time consuming than steady-state simulation since the rotation of the rotor has to be resolved in fine angular steps and for each step a single result has to be calculated. In order to get even more accurate results transient simulation in combination with a structured grid should be performed.

The deviations between the CFD simulations and the calculation with the BEM software GH Bladed could be related to different causes. At first, it should be said that the grid resolution for the unstructured mesh should be further refined since there a rise of the mechanical power could be recognised and the drag coefficients also were much higher than for the structured mesh. Further simulations in [1] showed better agreement with the BEM calculations when refining the grid in chord wise direction.

Moreover, BEM software just calculates the power by using blade coefficients and not with a three-dimensional geometry as used in a CFD simulation. Also, the BEM software does not calculate the losses at the near hub region (3D effect) and at the tip (tip vortex). These are just included by means of empirical functions, which could be another reason for the deviations, since the CFD calculation accounts for the whole flow field developing around the wind turbine blade including viscous losses.

For further investigations concerning turbulence models, grid resolution and grid type and measured values of the mechanical power, the wind speed and the rotational speed should be comprised implicitly. If it were possible, also the pressure distribution at some selected airfoil sections would also be of special interest in order to compare it with the results of the simulations.

7 List of references

- 1 GRUBER, R.: CFD modelling and simulation of the airflow around a wind turbine. Diploma Thesis, Graz University of Technology, 2010.
- 2 <http://www.ifb.uni-stuttgart.de/~doerner/windenergie1.html> (04.09.2010)
- 3 <http://www.ifb.uni-stuttgart.de/~doerner/win9.gif> (04.09.2010)
- 4 HAMMEL, L.: Die Ausnutzung der Windkräfte. Berlin: Verlagsbuchhandlung Paul Parep, Verlag für Landwirtschaft, Gartenbau und Forstwesen, 1924.
- 5 SCHIEBER, W.: Energiequelle Windkraft. Berlin: Fackelträger-Verlag K.G. . G.B. von Bodenhausen-Bennhausen, 1941.
- 6 HAU, E.: Windkraftanlagen, Grundlagen, Technik, Einsatz, Wirtschaftlichkeit. 4. Auflage, Berlin-Heidelberg: Springer Verlag, 2008.
- 7 HONNEF, H.: Windkraftwerke. Braunschweig: Friedrich Vieweg & Sohn Akt.-Ges., 1932.
- 8 <http://www.cnngo.com/sites/default/files/imagecache/400x267/2010/07/26/inline.jpg> (02.11.2010)
- 9 <http://www.3sat.de/mediathek/?mode=play&obj=16222> (02.11.2010)
- 10 http://www.metaefficient.com/wp-content/uploads/e-126-wind_turbine.jpg (02.11.2010)
- 11 BOSSANYI, E.A.: GH Bladed Theory Manual. Garrad Hassan and Partners Limited, 2003.
- 12 KRONSCHNABL, F.J.: Numerische Strömungssimulation von Horizontalachsen-Windturbinen. Dissertation, Technische Universität München, 2008.
- 13 TANGLER, J.L.: The Nebulous Art of Using Wind-Tunnel Airfoil Data for Predicting Rotor Performance. In: *NREL/CP-500-31243*, 2002.
- 14 INGRAM, G.: Windturbine Blade Analysis using the Blade Element Momentum Method Version 1.0. School of Engineering, Durham University, 2005.
- 15 http://www.baesystems.com/ProductsServices/ss_tes_atc_flite3d.html (08.11.2010)
- 16 <http://www.grc.nasa.gov/WWW/winddocs/index.html> (08.11.2010)
- 17 SUMNER, J., WATTERS, C.S., MASSON, C.: CFD in Wind Energ: The Virtual, Multi Scale Wind Tunnel. In: *Energies* 2010, 3, p.989-1013, 2010.
- 18 TACHOS, N.S., FILIOS, A.E., MARGARIS, D.P.: A comparative study of four turbulence models for predicting of horizontal axis wind turbine flow. In: *Proceedings of the institution of mechanical engineers, Part C: Journal of Mechanical Engineering Science*, 2009.
- 19 LAURSEN, J.; ENEVOLDSEN, P.; HJORT, S.: 3D CFD Quantification of the Performance of a Multi-Megawatt Wind Turbine. In: *Journal of Physics: Conference Series* 75 012007, 2007.
- 20 KRAMER, R.; ARCHER, R.: Modelling Approaches for Flow over a Wind Turbine Blade. In: *Wind Engineering Volume 28 No.3*, 2004.
- 21 MENTER, F.R.: Two-Equation Eddy-Viscosity Turbulence Models for Engineering Applications. In: *AIAA Journal Volume 32, No. 8*, 1994.
- 22 ANSYS Europe, Ltd.: Ansys CFX Solver Theory Guide. Ansys CFX release 11.0, 2006.
- 23 <http://www.nrel.gov> (02.11.2010)

List of references

- 24 TACHOS, N.S., FILIOS, A.E., MARGARIS, D.P., KALDELLIS, J.K.: A Computational Aerodynamics Simulation of the NREL Phase II Rotor. In: *The Open Mechanical Engineering Journal*, 2009-3, p.9-16, 2009.
- 25 GÓMEZ-IRADI, S., BARAKOS, G.N.: Computational fluid dynamics investigation of some wind turbine rotor design parameters. In: Proc. IMechE Volume 222 Part A: J. Power and Energy, p.455-470, 2008.
- 26 JOHANSEN, J., SØRENSEN, N.N.: Aerofoil Characteristics from 3D CFD Rotor Computations. In: *Wind Energy*, 2004-7, p.283-294, 2004.
- 27 GUERRI, O., BOUHADEF, K., HARHAD, A.: Turbulent Flow Simulation of the NREL S809 Airfoil. In: *Wind Engineering Volume 30, No. 4*, p.287-297, 2006.
- 28 WOLFE, W.P., OCHS, S.S.: CFD Calculations of S809 Aerodynamic Characteristics. In: *AIAA-97-0973*, 1997.
- 29 CAMPOBASSO, M.S., ZANON, A., MINISCI, E., BONFIGLIOLI, A.: Wake-tracking and turbulence modeling in computational aerodynamics of wind turbine aerofoils. In: Proc. IMechE Volume 223 Part A: J. Power and Energy, p.939-951, 2009.
- 30 BERTAGNOLIO, F., SØRENSEN, N.N., RASMUSEN, F.: New Insight Into the Flow Around a Wind Turbine Airfoil Section. In: *Transactions of the ASME Volume 127*, p.214-221, May 2005.
- 31 XU, G., SANKAR, L.N.: Computational Study of Horizontal Axis Wind Turbines. In: *AIAA-99-0042*, 1999.
- 32 MADSEN, H.A., SØRENSEN, N.N., SCHRECK, S.: Yaw aerodynamics analyzed with three codes in comparison with experiment. In: *AIAA-2003-0519*, p.94-103, 2003.
- 33 TONGCHITPAKDEE, C., BENJANIRAT, S., SANKAR, L.N.: Numerical Simulation of the Aerodynamics of Horizontal Axis Wind Turbines under Yawed Wind Flow Conditions. In: *Transactions of the ASME Volume 127*, p.464-474, 2005.
- 34 TIMMER, W.A., VAN ROOIJ, R.P.O.M.: Summary of the Delft University wind turbine dedicated airfoils. In: *AIAA-2003-0352*, 2003.
- 35 BRUINING, A., TIMMER, W.A.: Airfoil characteristics of rotating wind turbine blades. In: *Journal of Wind Engineering and Industrial Aerodynamics*, 39 (1992), p.35-39, 1992.
- 36 AKAY, B., FERREIA, C.S., VAN BUSSEL, G.J.W.: Experimental Investigation of the Wind Turbine Blade Root Flow. In: *AIAA 2010-641*, 2010.
- 37 WILCOX, D.C.: Turbulence Modelling for CFD. La Canada: DWC Industries, Inc., 1994.
- 38 FERZIGER, J.H., PERIĆ, M.: Numerische Strömungsmechanik, Berlin-Heidelberg: Springer Verlag, 2008.
- 39 SCHLICHTLING, H., GERSTEN, K.: Grenzschichttheorie 10. Auflage, Berlin-Heidelberg: Springer Verlag, 2006.
- 40 STEINER, H., BASARA, B: Numerische Methoden in der Strömungslehre und Wärmeübertragung, Skriptum 2006.
- 41 HANJALIĆ, K.: Closure Models for Incompressible Turbulent Flows. Department of Applied Physics, Delft University of Technology, 2004.
- 42 ANSYS Europe, Ltd.: Ansys CFX Solver Modeling Guide. Ansys CFX release 11.0, 2006.
- 43 FREY, P.J., GEORGE, P.L.: Mesh Generation Application to Finite Elements. United States and Great Britain: ISTE Ltd and John Wiley & Sons, Inc, p.95, 2008.
- 44 GASCH, R., TWELE, J.: Windkraftanlagen : Grundlagen, Entwurf, Planung und Betrieb. 6. Auflage Wiesbaden: Vieweg + Teubner, 2010.

8 List of tables

Table 1	Overview of global mesh size and part mesh size	35
Table 2	Overview of the calculated values for 5 prism layers within the boundary layer	40
Table 3	Overview of generated mesh types	42
Table 4	Overview of the boundary conditions considered.....	49
Table 5	Overview of the deviation of the models in comparison to the SST k/ω model (boundary condition I)	52
Table 6	Overview of the deviation of the models in comparison to the SST k/ω model (Boundary condition II)	54
Table 7	Overview of the deviation of the models in comparison to the SST k/ω model (structured mesh, boundary condition I)	55
Table 8	Streamlines on suction side for the SST k/ω turbulence model in terms of the used mesh (boundary condition I, $-0,9^\circ$ pitch)	56
Table 9	Streamlines on suction side for the k/ω turbulence model in terms of the used mesh (boundary condition I, $-0,9^\circ$ pitch)	57
Table 10	Streamlines on suction side for the BSL k/ω turbulence model in terms of the used mesh (boundary condition I, $-0,9^\circ$ pitch)	57
Table 11	Streamlines on suction side for the k/ε turbulence model in terms of the used mesh (boundary condition I, $-0,9^\circ$ pitch)	58
Table 12	Streamlines on suction side for the Spalart-Allmaras turbulence model in terms of the used mesh (boundary condition I, $-0,9^\circ$ pitch).....	58
Table 13	Streamline plots coloured by the magnitude of the local velocity for the 4 m distance from the root airfoil section	63
Table 14	Streamlines on the suction side in terms of the turbulence model used in combination with the fine unstructured mesh (boundary condition I, $-0,9^\circ$ pitch).....	65
Table 15	Streamlines on the suction side in terms of the turbulence model used in combination with the structured mesh (boundary condition I, $-0,9^\circ$ pitch)	66
Table 16	Deviations of the lift coefficient with regard to the unstructured fine mesh compared to the SST k/ω model (boundary condition I, $-0,9^\circ$ pitch)	67
Table 17	Deviations of the lift coefficient with regard to the structured mesh compared to the SST k/ω model (boundary condition I, $-0,9^\circ$ pitch).....	68
Table 18	Comparison of the pressure distribution around the 16 m airfoil section for unstructured and structured mesh (SST k/ω model, boundary condition I, $-0,9^\circ$ pitch)	71
Table 19	Comparison of the pressure distribution for unstructured and structured meshes at the three lower airfoil sections (SST k/ω model, boundary condition I, $-0,9^\circ$ pitch).....	72
Table 20	Streamline overview of all examined airfoil sections for the unstructured fine mesh, coloured by the magnitude of the local velocity (boundary conditon I, $-0,9^\circ$ pitch).....	75

List of tables

Table 21	Streamline overview of all examined airfoil sections for the structured mesh, coloured by the magnitude of the local velocity (boundary condition I, $-0,9^\circ$ pitch).....	76
Table 22	Comparison of the tip vortex formation for the unstructured fine mesh and the structured mesh (boundary condition I, $-0,9^\circ$ pitch).....	77
Table 23	Settings for transient simulation	78
Table 24	Development of an eddy at the 4 m distance from the root airfoil section, resolved in 4° azimuth angle steps.....	79
Table 25	Deviations related to the GH Bladed (BEM) calculation without wind profile.....	81
Table 26	Overview of the variables for the wind profile.....	83

9 List of diagrams

Diagram 1	Axial velocity distribution against the X direction (rotational axis of the turbine).....	45
Diagram 2	Mechanical power against pitch angle, coarse mesh $y^+ = 81$ (boundary condition I).....	50
Diagram 3	Mechanical power against pitch angle, middle mesh $y^+ = 28$ (boundary condition I).....	51
Diagram 4	Mechanical power against pitch angle, fine mesh $y^+ = 18$ (boundary condition I).....	52
Diagram 5	Variation of the computed power for each turbulence model in terms of the.....	53
Diagram 6	Mechanical power against pitch angle, fine mesh $y^+ = 18$ (boundary condition II).....	54
Diagram 7	Variation of the computed power for each turbulence model in comparison to the structured / unstructured mesh (boundary condition I).....	55
Diagram 8	Pressure coefficient c_p for different mesh types used in combination with the SST k/ω model.....	59
Diagram 9	Pressure coefficient c_p for different mesh types used	60
Diagram 10	Pressure coefficient c_p for different mesh types used in combination with the BSL k/ω model.....	61
Diagram 11	Pressure coefficient c_p for different mesh types used	61
Diagram 12	Pressure coefficient c_p for different mesh types used	62
Diagram 13	Lift coefficient against the distance from the root in combination with	67
Diagram 14	Lift coefficient against the distance from the root in combination with	68
Diagram 15	Drag coefficient against the distance from the root in combination with	69
Diagram 16	Drag coefficient against distance from the root in combination with	70
Diagram 17	Comparison of pressure coefficient at the 16 m airfoil section for unstructured and	72
Diagram 18	Wall shear stress against the normalized chord in combination with the unstructured.....	73
Diagram 19	Wall shear stress against the normalized chord in combination with the structured fine mesh (boundary condition I, $-0,9^\circ$ pitch)	74
Diagram 20	Mechanical power against the azimuth angle for the transient simulation.....	78
Diagram 21	Overview of the deviations with regard to the GH Bladed (BEM) calculation	81
Diagram 22	Mechanical power against the azimuth angle for the	82
Diagram 23	Mechanical power reduction factor against azimuth angle	82
Diagram 24	Wind speed against z direction.....	83
Diagram 25	Comparison of the results with and without wind profile	84
Diagram 26	Comparison of the power coefficient (boundary condition I, $-0,9^\circ$ pitch).....	85
Diagram 27	Final comparisons of the conducted simulations against the BEM results (boundary	87

10 List of figures

Fig. 1	Eclipse Wind Turbine [].....	2
Fig. 2	4 MW Darrieus-Rotor [6].....	3
Fig. 3	Scheme of the large-scale power plant (left) and swimming.....	4
Fig. 4	New floating wind turbine []	5
Fig. 5	Currently, worlds largest wind turbine Enercon E-126 []	6
Fig. 6	Flow conditions across the actuator disk [].....	7
Fig. 7	Annular Element for Blade Element theory [12]	8
Fig. 8	Streamline plot around a 5,1 m radius blade section(about 10% blade height) at 9,75 m/s wind speed, 15,7 rpm and -0,9° pitch of the WT2000 HAWT	9
Fig. 9	Frontview (left) and sideview (right) of the whole domain used for the computations in the present thesis	10
Fig. 10	Split flow field for hybrid Navier-Stokes solver [31]	16
Fig. 11	Dye filament in Reynolds' experiment 1883,.....	18
Fig. 12	Averaging of the velocity component U for a statistical steady (left).....	20
Fig. 13	Schematic diagram of the overall alignment of the domains (sideview)	27
Fig. 14	Front view of the whole domain with boundaries for "rotational periodicity" tagged by arrows	28
Fig. 15	Connecting different non-matching mesh types	29
Fig. 16	Different types of boundary conditions used for the simulation.....	30
Fig. 17	Section points of the lower part of the blade and section points of the hub.....	32
Fig. 18	Section points connected via spline curve	32
Fig. 19	Trailing edge linear closed (left), unrealistic closure by drawing spline (right).....	32
Fig. 20	Completed surface generation of the blade and hub	33
Fig. 21	Blade inside wireframe of surrounding surface	33
Fig. 22	Lower part of the blade and hub (element size 200 mm).....	34
Fig. 23	Upper part of the blade (element size from left to right 50 mm-200 mm)	34
Fig. 24	Refined leading edge marked by the red line.....	36
Fig. 25	Refined trailing edge marked in yellow.....	36
Fig. 26	Unstructured mesh around blade section.....	39
Fig. 27	Detailed view of the prism layers surrounding the surface of the blade.....	39
Fig. 28	Description of aspect ratio [42].....	41
Fig. 29	Reference coordinate system at 16m distance from the root.....	44
Fig. 30	Intersection planes at the selected airfoil sections.....	44
Fig. 31	Annular plane for determining the reduced axial velocity in front of the blade.....	46
Fig. 32	Profile section with associated forces and angles.....	47